UNIVERSITÀ
degli STUDI
di CATANIA

PHD IN MATERIALS SCIENCE AND NANOTECHNOLOGY

Antonio Brancato

ENGINEERED NANOMATERIALS FOR ENHANCED SPECTROSCOPY AND SENSING

Tutor:
Prof.ssa Luisa D'Urso

Supervisor:
Dr. Marcello Condorelli

Anno Accademico 2024-2025

Index

Abstract

This PhD thesis focuses on the controlled design of plasmonic and metal-free nanomaterials, where both morphology and composition are tailored to optimize their performance as substrates for Surface-Enhanced Raman Spectroscopy (SERS). By engineering nanoscale features and material characterizations (Raman, UV-visible and FT-IR spectroscopy, XPS, SEM, TEM, and AFM), it was possible to investigate how structural parameters directly influence both spectroscopic enhancement and plasmon-mediated reactivity.

A single-particle SERS study on Silver Nanoflowers (AgNFs) demonstrated their exceptionally broad plasmonic response and high density of electromagnetic hot-spots, enabling determination of enhancement factors across multiple excitation wavelengths.

A comparative study of plasmon-driven catalysis on Silver Nanospheres (AgNSs), Nanoplates (AgNPTs), and AgNFs revealed that both morphology and excitation wavelength govern reaction kinetics and product development. Specifically, 532 nm excitation promoted the dimerization of 4-nitrothiophenol (4-NTP) into 4,4′-dimercaptoazobenzene (DMAB), while 785 nm irradiation favored alternative reduction pathways leading to 4-aminothiophenol (4-ATP).

To address the intrinsic instability of silver nanostructures, a bimetallic strategy was pursued by coating AgNPTs with thin platinum shells. These hybrid systems combined the strong plasmonic fields of the silver core with the chemical stability of platinum, resulting in more reliable SERS substrates.

Finally, a metal-free substrate was explored through laser irradiation in liquid of MoS_2, producing defect-engineered 2D semiconductors that provide SERS activity via charge-transfer mechanisms. These approaches highlight the versatility of tailored nanostructures for sensing applications.

Introduction

Surface-Enhanced Raman Spectroscopy (SERS) is one of the most powerful and sensitive techniques used to study the chemical and structural properties of molecules, even at very low concentrations, down to the level of a single molecule [1]. It also allows for non-destructive analysis, including measurements in biological fluids [2]. This method enables the study of the vibrational spectrum of molecules bonded to plasmonic substrates, which have special optical properties that strongly amplify the Raman signal.

The primary mechanism responsible for the SERS effect is electromagnetic enhancement, which arises from the interaction of light with high-refractive-index systems [3] or, more commonly, with noble metal nanostructures. In these materials, the collective oscillation of free electrons is induced by incident light, leading to the phenomenon known as Localized Surface Plasmon Resonance (LSPR). LSPR corresponds to the coherent oscillation of conduction electrons at the surface of metal nanoparticles (typically silver or gold) resulting in a strong amplification of the local electromagnetic field [2]. When the wavelength of the Raman spectroscopy light source (laser) matches the LSPR of the substrate, very strong and localized electric fields called hot-spots are created, especially at sharp tips, edges, or junctions between particles [4]. These hot-spots can increase the electric field intensity by several orders of magnitude, making the Raman signal of the nearby molecule much stronger.

The degree of amplification is calculated quantitatively using the Enhancement Factor (EF), defined as the ratio between the Raman signal intensity obtained in the presence of the SERS-active substrate and the corresponding signal measured under standard Raman conditions [5].

The strength of the plasmon resonance, and therefore the intensity of the SERS effect, depends greatly on the material, shape, and size of the nanoparticles [4]. Specifically, the geometry of the

particles affects the distribution of the electric field and hotspots which directly influences the EF. Chapter 1 of this thesis will give a general introduction to the physical principles of LSPR and SERS, with a detailed explanation of how optical properties are connected to the shape and structure of the substrates.

Given the crucial role of particle morphology, the design control of nanoparticles is a key step to create effective SERS substrates. Chemical nanoparticles synthesis will be the focus of chapter 2 showing methods that allow precise control over nanoparticle size and shape, which is especially important for making substrates that are reproducible and suitable for large-scale production.

The use of multi-branched Silver Nanoparticles such as Silver Nanoflowers will be the focus of chapter 3. The high roughness of these structures helps to create many hot-spots, making them excellent for amplifying Raman signals. Their enhancement factor (EF) has been tested at different laser wavelengths, showing good performance from the visible to the near-infrared range. This is due to the broad plasmonic band of nanoflowers, which allows them to match the resonance of many commonly used Raman lasers. In general, the strongest SERS signals occur when the laser wavelength excites the plasmon resonance of the substrate, and nanoflowers are particularly versatile.

In Chapter 4 the concept of plasmon-driven reactions will be introduced exploring how SERS can be used to monitor in real time such chemical reactions using plasmonic substrates. These are chemical reactions influenced by the transfer of hot-electrons, which are high-energy electrons generated during plasmon excitation. Reactions involving molecules linked to different nanoparticle shapes (Nanospheres, Nanoplates, and Nanoflowers) will be compared in terms of reaction kinetics, conversion, and selectivity, showing how nanoparticle shape affects the efficiency of the reaction.

Chapter 5 deals with one of the main problems of silver-based SERS substrates: their low stability and limited reproducibility in SERS measurements. To improve this, bimetallic substrates were

synthesized by coating Silver Nanoplates with platinum. Different synthesis conditions were tested to control the coating amount, to keep a high Raman signal while improving the durability and reliability of the measurements. Platinum works as a protective layer, helping to make the SERS substrate more stable over time.

In Chapter 6, the thesis will explore an emerging aspect in SERS research: the use of semiconductors materials. Specifically, molybdenum disulfide (MoS_2) was modified using laser irradiation in liquid (LIL), a method that creates many structural defects. These defects were shown to boost the Raman signal, even without using traditional plasmonic metals. The SERS enhancement is not due to the typical electromagnetic mechanism but is attributed to the chemical enhancement mechanism. Controlling these defects may offer a new way to improve the SERS effect using metal-free materials.

Thus, this thesis shows how important it is to control the synthesis and design of materials used for SERS, depending on the specific goal. From creating powerful plasmonic structures for SERS signal enhancement, to controlling chemical reactions or improving the stability and sustainability of the substrates, each chapter contributes to a deeper understanding of the connection between material nanostructuration and SERS applications.

Chapter 1

1.1 Localized Surface Plasmon Resonance (LSPR)

The use of metal nanoparticles as SERS substrates is due to their special optical properties. When the frequency of the electromagnetic field of the incident light matches the oscillation frequency of the free electrons in the nanoparticle, there is a strong absorption and scattering of light. This is the phenomenon known as Localized Surface Plasmon Resonance (LSPR). Resonance conditions only happen for certain wavelengths and depend on the geometry, the dimension and the nature of the metal of the nanoparticles [2], [4].

LSPR allows the amplification of the electric field by several orders of magnitude, making Raman spectroscopy much more sensitive compared to other configuration when no substrate is used [5].It is possible to calculate the resonance conditions analytically only for some simple shapes. The easiest case is a spherical nanoparticle with a diameter much smaller than the wavelength of the incoming light. In this situation, the quasi-static approximation is used, which simplifies the problem by considering just a sphere placed in a uniform electric field [6].

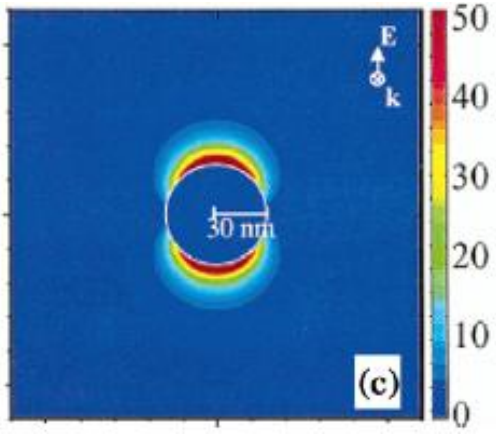

Figure 1.1. Electric field distribution of a spherical silver nanoparticle during the excitation of the LSPR dipolar mode. The red region is called hot-spot [7].

Under these conditions, the interaction between light and the material creates an electric field outside the nanoparticle (E_{out}) (fig. 1.1), which is the sum of two parts:

$$E_{out} = E_0 + E(p) \tag{1}$$

Where E_0 is the electric field of the incoming light, and E(p) is the additional field dependent by the dipole moment p induced by the electrons displacement in the particle:

$$p = \varepsilon_m \alpha E_0 \tag{2}$$

Where ε_m is the dielectric function of the surrounding medium, and α is the polarizability of the system, expressed as:

$$\alpha = 4\pi \frac{\varepsilon - \varepsilon_m}{\varepsilon + 2\varepsilon_m} r^3 \tag{3}$$

Where r is the radius of the nanosphere and ε is the dielectric function of the nanoparticle. It is possible to observe that, if the medium around the sphere is non-absorbing, the polarizability becomes maximum when:

$$\varepsilon = -2\varepsilon_m \tag{4}$$

Since ε_m is positive, ε must be negative. Normally, the dielectric function $\varepsilon(\omega)$ (as a function of frequency) is positive, but metals like silver and gold can have $\varepsilon(\omega) < 0$ from the ultraviolet to near-infrared range.

The dielectric function $\varepsilon(\omega)$ can be described using the Lorentz model [8]. For metal nanoparticles, it is common to use the Drude model [9], which gives the following equations:

$$Re[\varepsilon(\omega)] = 1 - \frac{\omega_p^2}{\omega^2} \tag{5}$$

$$Im[\varepsilon(\omega)] = \frac{\gamma\omega_p^2}{\omega^3} \tag{6}$$

Where $Re[\varepsilon(\omega)]$ and $Im[\varepsilon(\omega)]$ are the real and imaginary parts of the dielectric function, ω_p is the plasma frequency of the material, γ is the damping factor (related to electron collisions), and ω is the frequency of the incident light.

In Figure 1.2a, it is possible to see that $Re[\varepsilon(\omega)]$ becomes zero at $\omega = \omega_p$, and becomes negative for $\omega < \omega_p$. This is very important for achieving plasmon resonance. Also, the imaginary part $Im[\varepsilon(\omega)]$ should be as small as possible, which is easier at high frequencies because it decreases with ω^3.

The real part of the dielectric function of metals, like gold and silver, can become negative and satisfy the condition for maximum polarizability. When α is at its maximum, LSPR happens, and the dipolar mode is excited in a spherical nanoparticle [7].

As shown in Figure 1.1, the electric field near the surface of the sphere becomes stronger at the poles (hot-spot regions), along the direction of the applied field, when α is maximum [7].

For the extinction spectrum of the nanospheres, a peak is expected when $Re[\varepsilon(\omega)] = -2\varepsilon_m$ (fig. 1.2b), as can be expressed from the scattering and absorption cross-sections (based on the Poynting vector) [7], [8]:

$$C_{sca} = \frac{k^4}{6\pi}|\alpha|^2 \tag{7}$$

$$C_{abs} = k\, Im[\alpha] \tag{8}$$

Where k is the wave vector of the incident light.

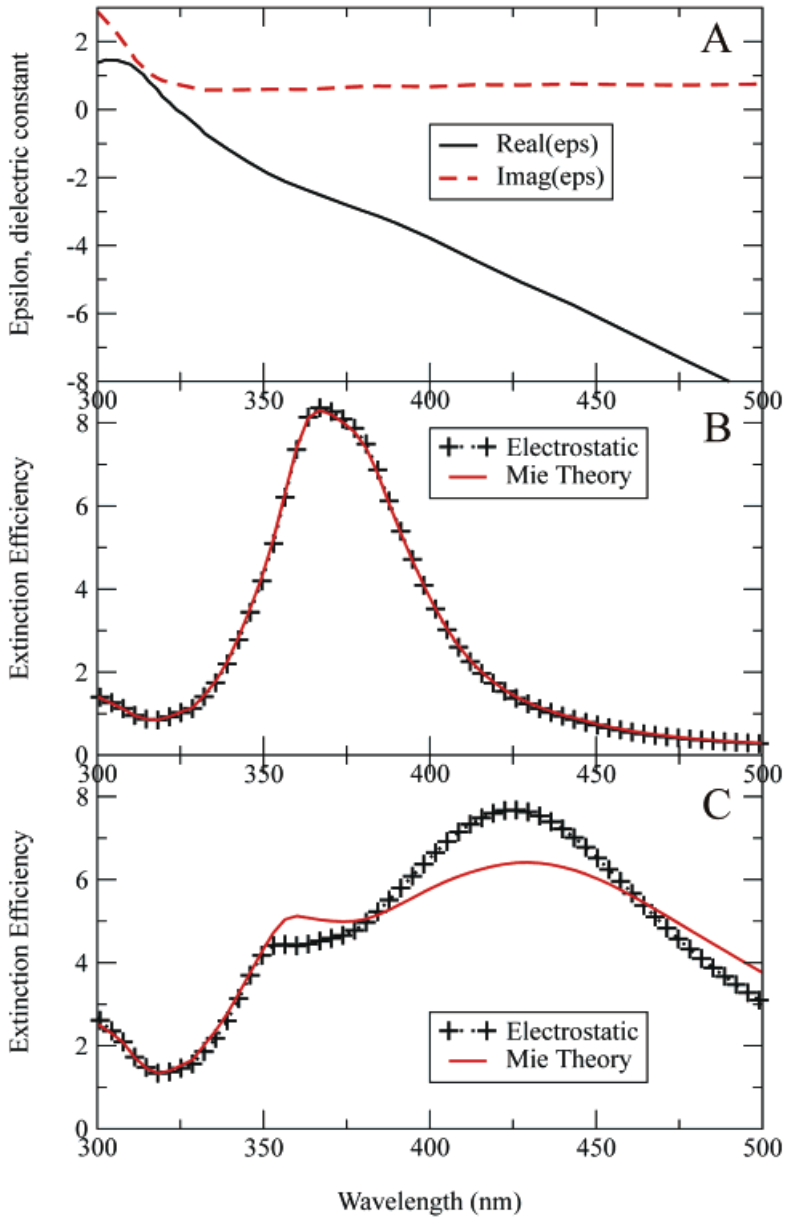

Figure 1.2. (a) Real and imaginary parts of silver dielectric function. (b) Extinction of a nanosphere obtained from quasi-static approximation. (c) The corresponding efficiency for a 60 nm particle [10].

These cross-sections depend not only on the material properties but also on the shape of the particle and the surrounding medium. This means that absorption (which occurs in all materials) must be distinguished from LSPR. For example, in spherical nanoparticles, increasing the particle size leads to the increase of the scattering effect because $C_{sca} \propto r^6$, instead $C_{abs} \propto r^3$. This means that small particles mainly contribute through absorption, while larger ones show stronger scattering.

When the particle size is small, as shown in Figure 1.1, the electric field is mainly confined at two poles, and the excited LSPR corresponds to the dipolar mode (l = 1). However, as the particle size increases, while bigger than the wavelength of the incident light, higher-order multipolar modes begin to appear, like quadrupole (l = 2). Moreover, in small spherical nanoparticles, the extinction spectrum shows only one peak from the dipolar mode, while the others are negligible (fig. 1.2b). But for larger particles, higher-order modes can also appear. For example, a 60 nm silver sphere already shows a quadrupolar signal at 357 nm (fig. 1.2c) [10].

By considering all resonance conditions for different modes, the polarizability becomes [11]:

$$\alpha_l = 4\pi \frac{\varepsilon - \varepsilon_m}{\varepsilon + \left(\frac{l+1}{l}\right)\varepsilon_m} a^3 \tag{9}$$

For quadrupolar mode (l = 2), resonance happens when $Re[\varepsilon(\omega)] = -\frac{3}{2}\varepsilon_m$ This condition is reached at a higher frequency of the light than for the dipolar mode (l = 1).

To better understand plasmonic modes, it is possible to represent the surface charge distribution *σ(x, y)* of an elongated nanoparticle like a nanorod [11]. Each plasmon mode has a number of nodes equal to two times its order (fig. 1.3). So, the dipole (l = 1) has two nodes. The zero-order mode is not visible unless the particle has a net charge.

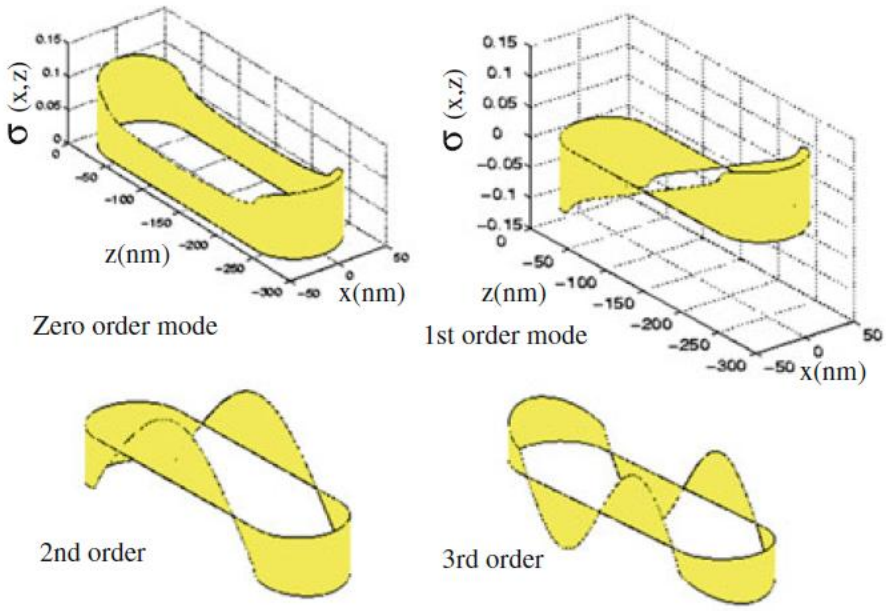

Figure 1.3. Surface charge density distribution related to the plasmonic modes of a nanorod [11].

Changing the shape of the nanoparticle, from a sphere to another shape, removes spatial symmetry in different directions of the electric field. This changes the polarizability and the resonance conditions [9].

The simplest example is transforming a sphere into an ellipsoid. In this shape, the free electrons move differently along the three main axes of the nanoparticle when exposed to the electric field. As a result, there are three different resonance conditions, based on the depolarization factor (L_i). For an ellipsoid:

$$L_x \neq L_y \neq L_z \tag{10}$$

The new equation for polarizability becomes [9]:

$$\alpha_i = 4\pi \frac{\varepsilon - \varepsilon_m}{3\varepsilon_m + 3L_i(\varepsilon - \varepsilon_m)} abc \tag{11}$$

Where a, b, c are the three semi-axes of the ellipsoid. In the special case of a sphere $L_x = L_y = L_z = 1/3$.

1.2 The Raman Effect

SERS is an evolution of classical Raman spectroscopy. The amplification obtained with SERS allows to overcome many of its limitations, such as the low signal intensity [12]. However, to understand the potential of the SERS technique, it is necessary to have a basic knowledge of the fundamental principles on which Raman spectroscopy is based.

Raman is a type of vibrational spectroscopy that can be applied to solid, liquid, or gas samples. It provides structural information about a molecule by analyzing its vibrations. When a monochromatic laser beam interacts with a sample, most of the light is scattered elastically, without any change in frequency (Rayleigh scattering). However, a small part of the light is scattered inelastically, with a change in frequency caused by its interaction with the vibrational modes of the molecule. This frequency change corresponds to one vibrational quantum of the molecule [12]. This phenomenon, known as the Raman effect, produces a characteristic spectrum that can be considered the "fingerprint" of the molecule [13]. As a result, Raman spectroscopy is used in many fields, including materials chemistry, biology, and forensic analysis [12], [14].

Another advantage of Raman spectroscopy is its capability to analyze samples that contain water, since water does not absorb visible light used in Raman lasers (from UV to near-infrared), unlike infrared spectroscopy, which cannot be used with aqueous samples.

However, the Raman signal is very weak due to the very low probability that a photon is scattered inelastically. As showed in Figure 1.4, typical Raman cross-sections are on the order of 10^{-30} cm^2. In contrast, IR spectroscopy, which is based on the absorption of incoming light, has a cross-

section around 10^{-20} cm^2 [15]. For this reason, many efforts have been made to create experimental conditions that increase the Raman signal and make the technique more sensitive [13] and in the case of SERS is possible to reach a cross-section around 10^{-16} cm^2.

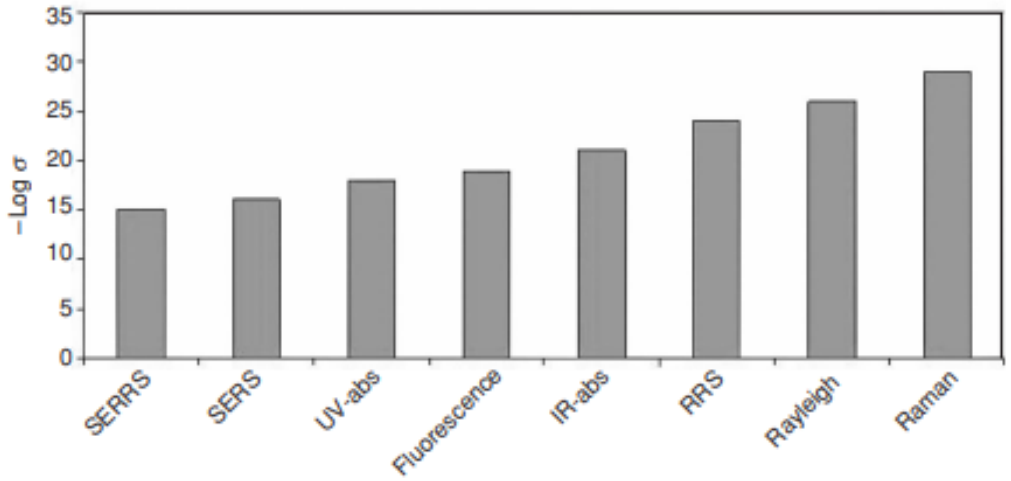

Figure 1.4. Cross-sections for different spectroscopic techniques [15].

To explain the Raman effect in a simple way, it is possible to follow a classical approach; however, a quantum view of the phenomenon is necessary for a more accurate understanding. In the classical model, the Raman effect is described as the result of the interaction between the electric field of the incident laser radiation and the electron cloud of the molecule. The electric field (E) induces a dipole moment (P) in the molecule, whose intensity is proportional to the polarizability (β) of the molecule [16]:

$$P = \beta E \tag{12}$$

The induced dipole oscillates and scatters light at three different frequencies: the same as the incident radiation (Rayleigh scattering), a lower one (Stokes scattering), and a higher one (anti-Stokes scattering). The last two represent the Raman effect. To obtain these three types of light

scattering analytically, it is necessary to rewrite the terms of the polarizability (β) and electric field (E). The electric field of the incident radiation can be written as a periodic wave over time (t), with a maximum amplitude E_0 and frequency ω_0:

$$E = \frac{1}{2}E_0\left(e^{i\omega_0 t} + e^{-i\omega_0 t}\right) \tag{13}$$

The polarizability of the molecule can change over time due to vibrational motions; therefore, it can be expressed using a Taylor series expansion for the molecules normal coordinates (Q_k):

$$\beta = \beta_0 + \left(\frac{\partial \beta}{\partial Q_k}\right)_0 Q_k \tag{14}$$

Here, k represents the k-th vibrational mode of the molecule.

The Taylor series is stopped at the first order by using the electric harmonic approximation, which assumes that the change in polarizability is proportional to the first power of Q_k [16]. The normal coordinates Q_k depend on time in a similar way to the electric field (E) in equation (13), by including the vibrational frequency of the molecule (ω_k):

$$Q_k = \frac{1}{2}Q_{k_0}\left(e^{i\omega_k t} + e^{-i\omega_k t}\right) \tag{15}$$

Thus, inserting equations (13), (14) and (15) in the equation (12) the induced dipole moment becomes:

$$P = \left[\beta_0 + \left(\frac{\partial \beta}{\partial Q_k}\right)_0 \frac{1}{2}Q_{k_0}\left(e^{i\omega_k t} + e^{-i\omega_k t}\right)\right]\frac{1}{2}E_0\left(e^{i\omega_0 t} + e^{-i\omega_0 t}\right) \tag{16}$$

And rearranging:

$$P = \frac{1}{2}\beta_0 E_0\left(e^{i\omega_0 t} + e^{-i\omega_0 t}\right) + \frac{1}{4}\left(\frac{\partial\beta}{\partial Q_k}\right)_0 E_0 Q_{k_0}\left[\left(e^{i(\omega_0+\omega_k)t} + e^{-i(\omega_0+\omega_k)t}\right) + \left(e^{i(\omega_0-\omega_k)t} + e^{-i(\omega_0-\omega_k)t}\right)\right] \quad (17)$$

At the end, using the Euler's formula is possible to rewrite equation (17) as:

$$P = \beta_0 E_0 \cos\omega_0 t + \frac{1}{2}\left(\frac{\partial\beta}{\partial Q_k}\right)_0 E_0 Q_{k_0}[\cos(\omega_0 + \omega_k)t + \cos(\omega_0 - \omega_k)t] \quad (18)$$

The induced dipole can scatter light at three different frequencies. The radiation at ω_0 is called Rayleigh scattering, while the radiations shifted by the vibrational frequency ω_k are known as Raman Stokes scattering $(\omega_0 - \omega_k)$ and anti-Stokes scattering $(\omega_0 + \omega_k)$ [16]. Furthermore, it can be concluded that the Raman effect occurs if $\left(\frac{\partial\beta}{\partial Q_k}\right)_0 \neq 0$. This condition is known as a selection rule, meaning that the molecule must change its polarizability during the vibration.

In Figure 1.5 is shown a Raman spectrum with the Raman shift in wavenumbers on the x-axis. It is the typical representation of the vibrational energy shift from the wavelength of the incident laser. The highest peak centred at 0 cm^{-1} is the elastic Rayleigh scattering, and the other signals are due to the inelastic scattered light. In this example is reported the entire spectrum with Stokes and anti-Stokes regions but often just the Stokes signals are showed.

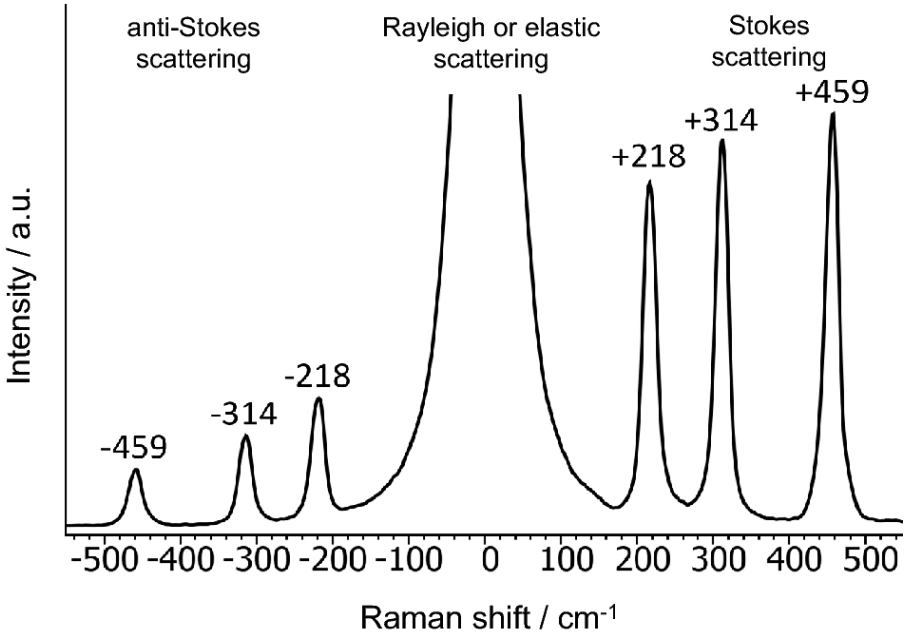

Figure 1.5. Raman Spectrum. The incident radiation is scattered by the molecule either elastically (Rayleigh scattering) or inelastically (Stokes and anti-Stokes scattering) [17].

According to a semi-quantistic approach, the incident photon interacts with the molecule, promoting it to a virtual state between the ground electronic state and the next one. It can be imagined that the molecule undergoes a transition to this virtual state, which has an extremely short lifetime, and then immediately returns to the ground electronic state. However, it may arrive in a different vibrational state than the one it started from (fig. 1.6) [16], [18]. If the virtual state does not correspond to a real electronic state, the process is called normal Raman scattering. But when the frequency of the incident photon matches the energy required for a real electronic transition, the process is called resonant Raman scattering (fig. 1.6), which produces signals of much higher intensity [16].

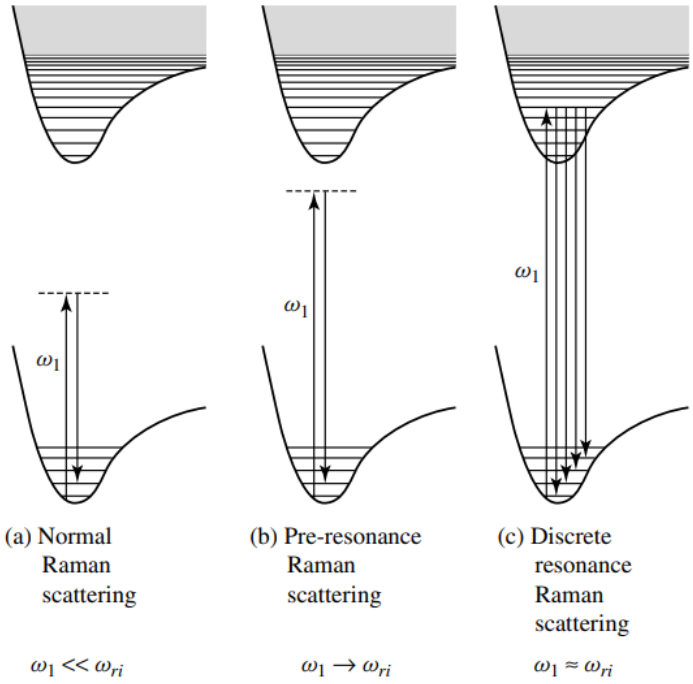

Figure 1.6. Representation of normal and resonant Raman processes. In the figure, ω_0 is the frequency of the incident light, while ω_{ri} represents the energy difference between the electronic states i and r [16].

1.3 Surface-Enhanced Raman Scattering (SERS)

The goal of the SERS technique is to amplify the cross-section of one or more Raman-active vibrational modes in order to detect concentrations lower than the detection limit of normal Raman spectroscopy. To quantify the effectiveness of the SERS technique, the Enhancement Factor (EF) is used. It compares the intensity of the signal obtained using SERS (I_{SERS}) with the signal from normal Raman spectroscopy (I_{Raman}), normalized to the number of molecules involved (N_{SERS} and N_{Raman}) [5].

$$EF = \frac{I_{SERS}/N_{SERS}}{I_{Raman}/N_{Raman}} \tag{19}$$

In some special cases, the technique allows achieving EF values up to 10^{14}, making it possible to detect even single molecules [1].

The amplification of the SERS signal (enhancement) is mainly due to two mechanisms: electromagnetic enhancement (EM) and chemical enhancement (CE) [5].

The electromagnetic mechanism is often dominant and occurs when the incident laser light excites surface plasmons localized on the metallic nanostructure. This excitation generates a strongly amplified electric field (hot-spot), located near the metallic surface, especially in the small gaps between adjacent particles. The analyte located in these areas experiences a double amplification [19].

In fact, the EM can be described with two amplification steps, and the first one takes place when the analyte interacts with the incident field, which is amplified by the plasmons (fig. 1.7). An amplification factor for the incident radiation ($M_{loc}(\omega_0)$) can be calculated as the ratio between the squared magnitudes of the local electric field ($E_{loc}(\omega_0)$) on the active SERS substrate and the electric field of the laser radiation ($E_0(\omega_0)$) [5], [19].

$$M_{loc}(\omega_0) = \frac{|E_{loc}(\omega_0)|^2}{|E_0(\omega_0)|^2} \tag{20}$$

The second amplification occurs when the scattered Raman signal is re-emitted amplified, if it maintains the plasmon resonance conditions (fig. 1.7).

Also in this case, an electromagnetic field amplification factor ($M_{Rad}(\omega_S)$) can be defined as the ratio between the squared magnitudes of the electric fields of the scattered Raman radiation in presence ($E_{loc}(\omega_S)$) and absence ($E_0(\omega_S)$) of the active SERS substrate [19], [20].

$$M_{Rad}(\omega_S) = \frac{|E_{loc}(\omega_S)|^2}{|E_0(\omega_S)|^2} \tag{21}$$

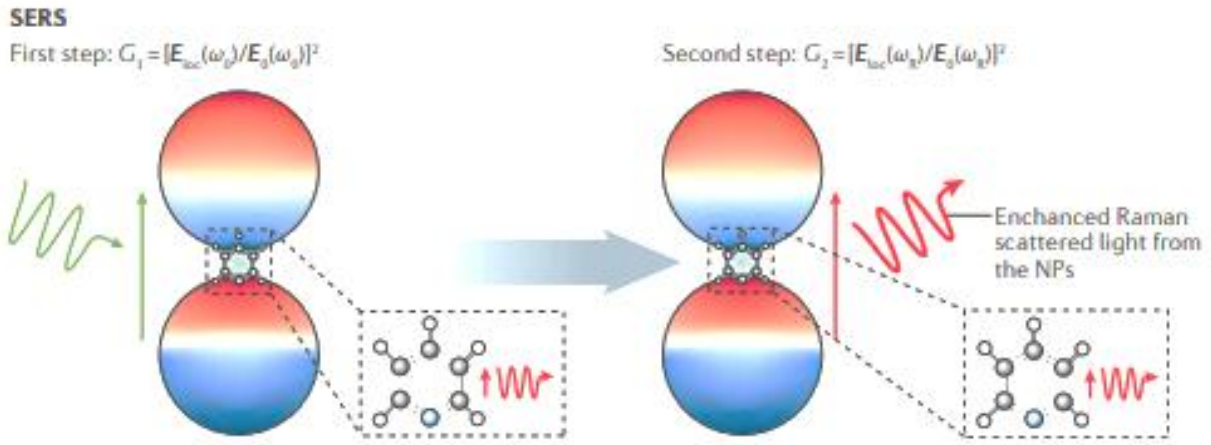

Figure 1.7. Diagram of the two-step electromagnetic field amplification mechanism by the metallic nanostructure. The laser radiation reaches the metallic nanostructure at a wavelength that excites the plasmon, allowing localization and amplification of the field, and then it is scattered by the analyte maintains the resonance conditions with an amplified emission by the nanostructure [20].

The chemical enhancement mechanism, although it contributes less then EM, is based on the chemical-physical interaction between the analyte and the metallic substrate. This interaction can change the polarizability of the molecule or modify the electronic distribution through charge transfer [5].

It is expressed as the ratio between the polarizability magnitude of the molecules with the SERS substrate (β_{SERS}) and without (β_0):

$$Chemical\ Enhancement\ (CE) = \frac{|\beta_{SERS})|^2}{|\beta_0)|^2} \tag{22}$$

Chemical amplification does not require the substrate to be plasmonic, which is very useful for designing metal-free substrates.

It can be possible to consider all the amplification contributions, with the total Enhancement Factor expressed as [5]:

$$EF = M_{loc}(\omega_0) \times M_{Rad}(\omega_S) \times CE \tag{23}$$

And by substituting each contribution:

$$EF = \frac{|E_{loc}(\omega_0)|^2}{|E_0(\omega_0)|^2} \times \frac{|E_{loc}(\omega_S)|^2}{|E_0(\omega_S)|^2} \times \frac{|\beta_{SERS})|^2}{|\beta_0)|^2} \tag{24}$$

Trying to modify or increase each single contribution is very important to better understand the SERS amplification mechanisms, making scientific research easier for real-world applications.

References

[1] K. Kneipp and H. Kneipp, 'Single molecule Raman scattering', *Appl Spectrosc*, vol. 60, no. 12, 2006, doi: 10.1366/000370206779321418.

[2] R. Pilot, R. Signorini, C. Durante, L. Orian, M. Bhamidipati, and L. Fabris, 'A review on surface-enhanced Raman scattering', *Biosensors (Basel)*, vol. 9, no. 2, Jun. 2019, doi: 10.3390/BIOS9020057.

[3] Martín Caldarola *et al.*, 'Non-plasmonic nanoantennas for surface enhanced spectroscopies with ultra-low heat conversion', *Nat Commun.* 2015 Aug 4:6:7915. doi: 10.1038/ncomms8915.

[4] E. C. Le Ru and P. G. Etchegoin, 'Principles of Surface-Enhanced Raman Spectroscopy', *Principles of Surface-Enhanced Raman Spectroscopy*, 2009, doi: 10.1016/B978-0-444-52779-0.X0001-3.

[5] E. C. Le Ru and P. G. Etchegoin, 'Quantifying SERS enhancements', *MRS Bull*, vol. 38, no. 8, pp. 631–640, Aug. 2013, doi: 10.1557/MRS.2013.158.

[6] Y.-T. Long and C. Jing, 'Localized Surface Plasmon Resonance Based Nanobiosensors', 2014, doi: 10.1007/978-3-642-54795-9.

[7] X. Zhang, Y. L. Chen, R. S. Liu, and D. P. Tsai, 'Plasmonic photocatalysis', *Reports on Progress in Physics*, vol. 76, no. 4, Apr. 2013, doi: 10.1088/0034-4885/76/4/046401,.

[8] C. F. Bohren and D. R. Huffman, 'Absorption and Scattering of Light by Small Particles', *Absorption and Scattering of Light by Small Particles*, Apr. 1998, doi: 10.1002/9783527618156.

[9] S. A. Maier, ‘Plasmonics: Fundamentals and applications’, *Plasmonics: Fundamentals and Applications*, pp. 1–223, 2007, doi: 10.1007/0-387-37825-1.

[10] K. L. Kelly, E. Coronado, L. L. Zhao, and G. C. Schatz, ‘The optical properties of metal nanoparticles: The influence of size, shape, and dielectric environment’, *Journal of Physical Chemistry B*, vol. 107, no. 3, pp. 668–677, Jan. 2003, doi: 10.1021/JP026731Y.

[11] S. Enoch and N. Bonod, Eds., ‘Plasmonics’, vol. 167, 2012, doi: 10.1007/978-3-642-28079-5.

[12] R. R. Jones, D. C. Hooper, L. Zhang, D. Wolverson, and V. K. Valev, ‘Raman Techniques: Fundamentals and Frontiers’, *Nanoscale Research Letters 2019 14:1*, vol. 14, no. 1, pp. 1–34, Jul. 2019, doi: 10.1186/S11671-019-3039-2.

[13] R. S. Das and Y. K. Agrawal, ‘Raman spectroscopy: Recent advancements, techniques and applications’, *Vib Spectrosc*, vol. 57, no. 2, pp. 163–176, Nov. 2011, doi: 10.1016/J.VIBSPEC.2011.08.003.

[14] E. R. Mojica and Z. Dai, ‘New Raman spectroscopic methods’ application in forensic science’, *Talanta Open*, vol. 6, p. 100124, Dec. 2022, doi: 10.1016/J.TALO.2022.100124.

[15] R. Aroca, ‘Surface-Enhanced Vibrational Spectroscopy’, *Surface-Enhanced Vibrational Spectroscopy*, pp. 1–233, Sep. 2007, doi: 10.1002/9780470035641.

[16] D. A. Long, ‘The Raman Effect’, Apr. 2002, doi: 10.1002/0470845767.

[17] J. R. Ferraro, K. Nakamoto, and C. W. Brown, ‘Basic Theory’, *Introductory Raman Spectroscopy*, pp. 1–94, Jan. 2003, doi: 10.1016/B978-012254105-6/50004-4.

[18] P. G. Etchegoin and E. C. Le Ru, ‘Basic Electromagnetic Theory of SERS’.

[19] S. Y. Ding, E. M. You, Z. Q. Tian, and M. Moskovits, ‘Electromagnetic theories of surface-enhanced Raman spectroscopy’, *Chem Soc Rev*, vol. 46, no. 13, pp. 4042–4076, Jul. 2017, doi: 10.1039/C7CS00238F.

[20] S.-Y. Ding *et al.*, ‘Nanostructure-based plasmon-enhanced Raman spectroscopy for surface analysis of materials’, *NatRM*, vol. 1, no. 6, p. 16021, Apr. 2016, doi: 10.1038/NATREVMATS.2016.21.

Chapter 2

2.1 Synthesis of Silver Nanoflowers

Several methods can be used to fabricate plasmonic SERS substrates, depending on the goal to be achieved. Many physical and chemical methods have been developed to synthesize metal nanoparticles with a wide variety of shapes and sizes. For example, to produce small spherical nanoparticles, pulsed laser ablation in liquid (PLAL) can be used [1] with a relatively simple experimental setup. Specifically, a Pulsed laser beam is focused onto an ultrapure metal target (gold, silver, copper, etc.) submerged in a solvent that may be organic or aqueous. By controlling experimental parameters such as power of the laser pulse, wavelengths, and pulse durations (for example, nanoseconds or femtoseconds), it is possible to achieve a wide range of results in terms of yield, size, and composition of the nanoparticles. Although this method is fast and simple, it often lacks high control over the shape, polydispersity, and stability of the produced nanoparticles. Techniques such as electron beam lithography (EBL) can be used to have greater control over shape and size [2]. In this method, a thin layer of polymer resist is spread on a substrate such as silicon oxide, and the desired pattern is then “written” onto the resist using a focused electron beam. The resist exposed to the electron beam becomes soluble when immersed in a specific solvent, leaving uncovered the areas where the electron beam wrote. A metallic layer is then deposited by evaporation, followed by a lift-off process that eliminates the remaining resist, leaving behind metal islands with well-defined shapes and sizes on the substrate. While this technique provides high precision and control, it is time-consuming and costly. A good compromise between cost-effectiveness, scalability, and control over the entire production process can be obtained with chemical synthesis [3]. The general principle of this method involves the

nucleation and controlled growth of particles from chemical precursors (typically metal salts) in the presence of reducing agents and shape-controlling agents (capping agents).

Typically, a metal precursor (e.g., silver nitrate or gold chloride) is dissolved in a solvent, and a capping agent (such as CTAB or PVP) is added to control particle growth and prevent aggregation. A reducing agent is then introduced to convert the metal ions into their elemental form. Once the concentration of metal atoms reaches a critical level, nuclei form, which grow as additional atoms deposit on them. By adjusting reaction conditions such as temperature, pH, concentration, and the type of stabilizer nanoparticles with different sizes and shapes, including spheres, cubes, and triangles, can be obtained in colloidal dispersion. This synthesis method is fast, does not require specialized equipment, and offers better control over particle morphology compared to EBL and PLAL. However, it is less reproducible than EBL, and the resulting nanostructures are coated with residual chemicals, unlike those produced by PLAL. In this chapter, chemical synthesis in aqueous environments will be used to synthesize plasmonic particles.

Usually, chemical syntheses involve two steps. In the first step, nanoparticle seeds are synthesized, and in the second step, the seeds grow along specific crystallographic directions. This method is called “seed-mediated growth” and will be described in the next section for the synthesis of silver nanoplates [4]. In this section, a method called “particle-mediated growth” will be described to synthesize Silver Nanoflowers (AgNFs).

AgNFs are micrometer-sized particles and can be described as a spherical core decorated with nanometric protrusions that resemble flower petals (fig. 2.1). The term “nano” refers to the nanostructured surface, and this terminology is widely used in the literature to describe this type of metallic particle, although they are also referred to as “mesoparticles” or “microflowers” [5], [6], [7], [8], [9], [10].

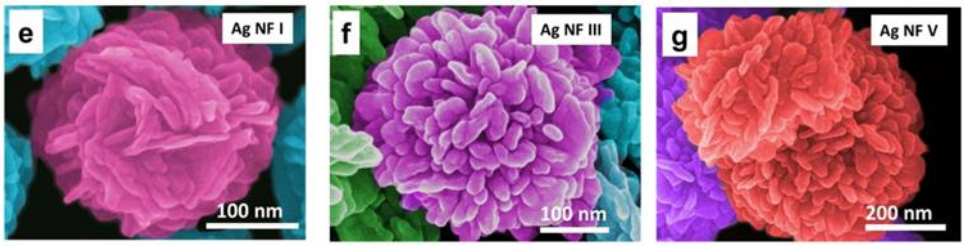

Figure 2.1. SEM images of Silver Nanoflowers [7].

The synthesis of AgNFs [11] was carried out by adding 1 ml of 0.5 M $AgNO_3$ to 10 ml of ultrapure water (Milli-Q grade) and keeping the solution in an ice bath. After 10 minutes, 0.1 ml of a 0.25 M sodium citrate solution was added. Finally, after 15 minutes and under strong stirring, 1 ml of 0.5 M L-ascorbic acid was added to the reaction mixture. The addition of the latter changed the color of the solution to dark grey, indicating the reduction of silver nitrate. Five minutes after the final addition, the nanoparticles were purified from excess reagents by wash-centrifuge cycles and dried for storage.

The morphological analysis was carried out using a SEM instrument (SUPRA-55 VP, Zeiss) by setting the electron probe energy at 15kV. The SEM images confirmed that the AgNF microparticles were obtained (fig. 2.2a) with a nanostructured surface (fig. 2.2b) with an average diameter of the particles around 1.72 ± 0.54 μm, and an average petal thickness of 96 ± 19 nm.

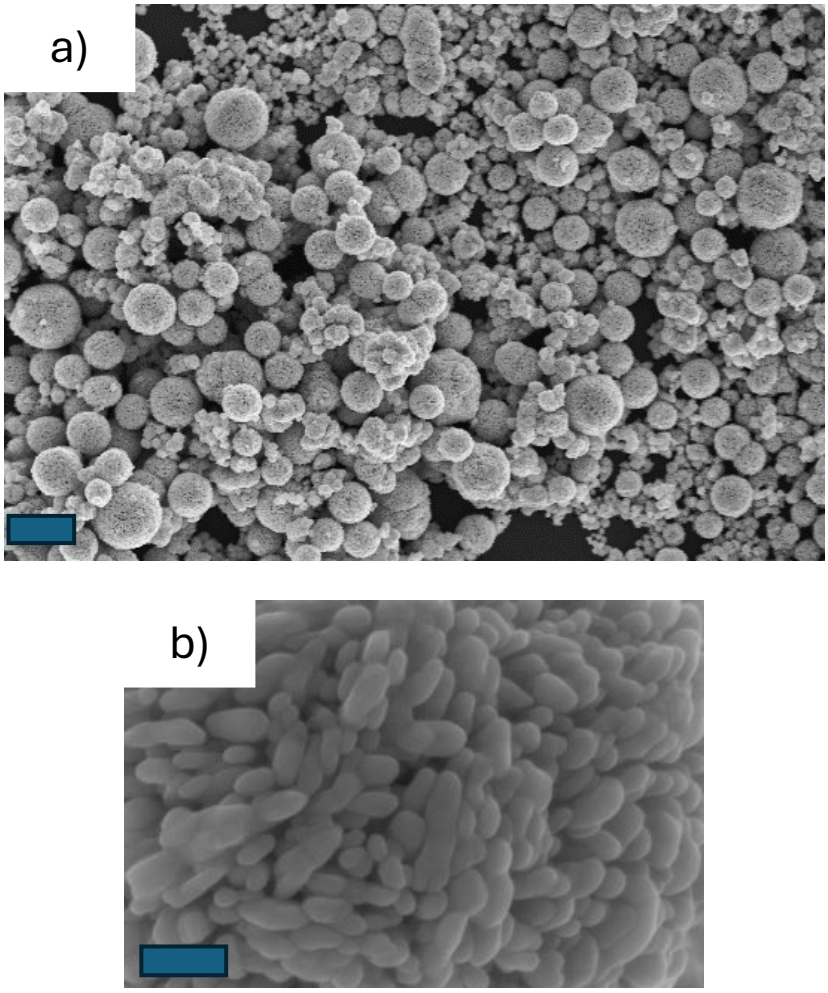

Figure 2.2. SEM images of a) obtained AgNFs (scale bar: 2 µm) and b) the petals of a single nanoflower (scale bar: 200 nm).

To understand how the formation of nanoflowers takes place, it is necessary to refer to a type of growth known as "particle-mediated growth" [12]. Typically, the synthesis follows the pattern described by the LaMer curve (Fig. 2.3), in which, after the reducing agent is added, there is an initial stage where the concentration of Ag^0 atoms in the solution rises until it reaches the critical level needed to initiate particle nucleation.

This marks the beginning of the second phase, where seed formation takes place, which stops when the concentration of Ag^0 atoms in solution drops below the minimum nucleation threshold, and at this point start the third phase. The seeds begin to aggregate, and through interfacial diffusion

processes, they merge into a single particle. Finally, in the fourth phase, the remaining metallic silver atoms further enrich the particles.

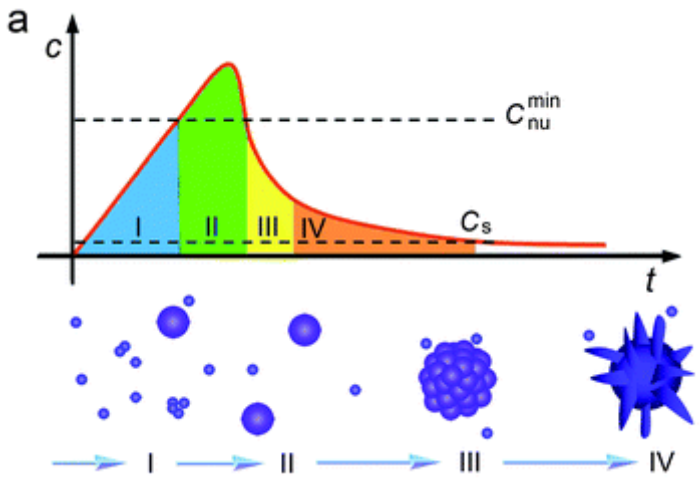

Figure 2.3. LaMer curve for nucleation and growth processes in "particle-mediated growth" [13].

So, it is clear that the aggregation of seeds must be so that the growth process follows a "particle-mediated growth" pathway. The conditions for it depend on the collision frequency between the seeds, which is closely related to the number of seeds per unit volume.

Besides the collision frequency, these collisions must occur in a useful way, meaning they allow the seeds to merge together. This condition can be satisfied by reagents such as ascorbic acid in the synthesis of silver microparticles because it can be adsorbed onto the surface of silver seeds, acting like a typical capping agent. Specifically, the hydroxyl groups of ascorbic acid enable the seeds to aggregate through hydrogen bonding.

To demonstrate that seed aggregation is necessary for the formation of microparticles, other syntheses were conducted using polyvinylpyrrolidone (PVP) as blocking agent for the particles growth reducing the size of the nanoflowers. In detail, AgNFs were prepared in the absence (0 mM) and in the presence of PVP at concentrations of 100 mM and 250 mM, which will be labeled as #1, #2, and #3, respectively.

The SEM images (fig. 2.4) highlight the changes in the AgNFs morphology induced by different PVP concentrations employed during the synthesis. Microstructures with average diameters of 1.7 µm, 1 µm, and 0.5 µm were obtained, respectively, for samples #1, #2, and #3, and a difference in the surface roughness of the three microstructures is observable. Specifically, the number of nano-petals that decorate the surface of the AgNF structure decreases with increasing PVP concentration and it is possible to deduce that the seed aggregation process was hindered by the capping action of the polymer, resulting in particles with significantly smaller sizes compared to those obtained without it.

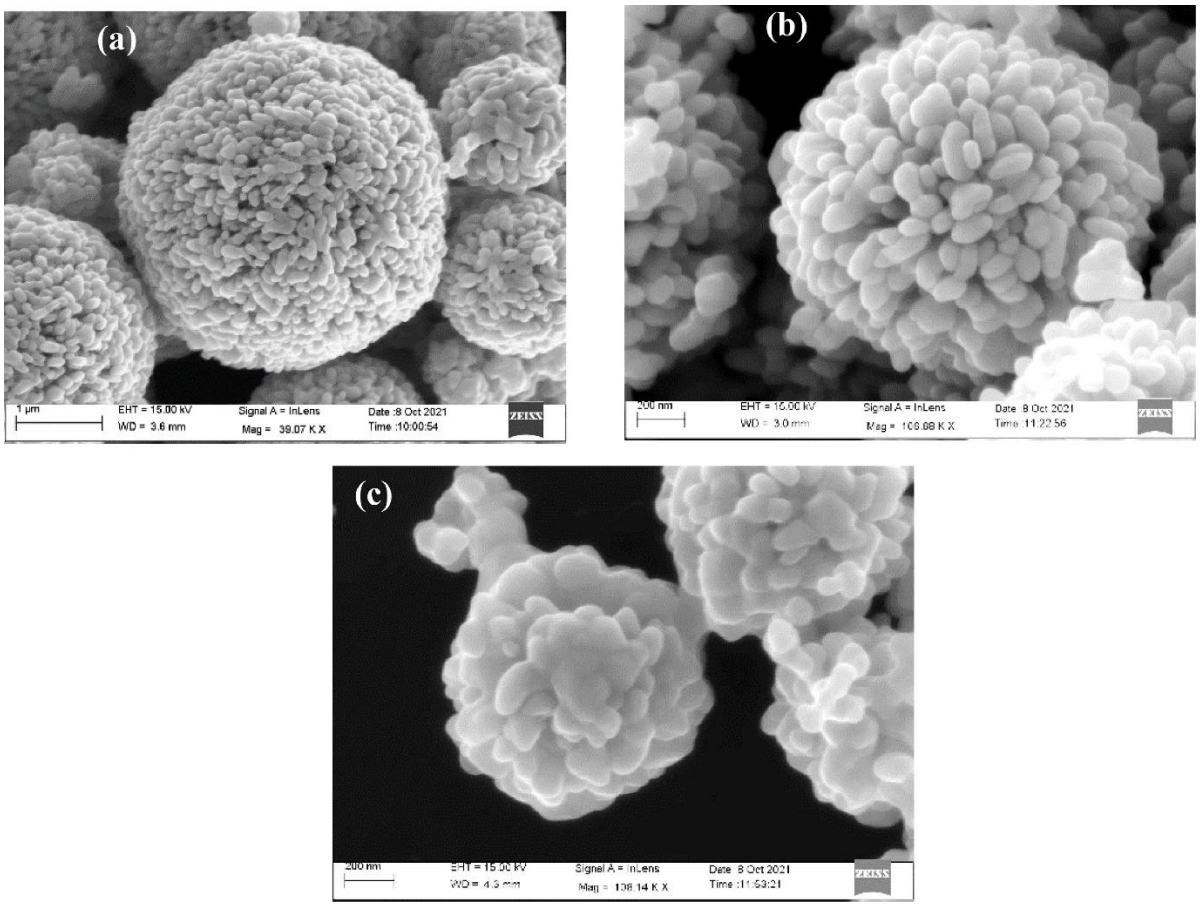

Figure 2.4. SEM images of AgNF obtained a) in the absence and the presence of PVP at a concentration of b) 100 mM and c) 250 mM. The difference in the magnification of the three images is due to the great difference in the dimensions of the three different microstructures [11].

Figure 2.5 shows the extinction spectra of aqueous dispersions of AgNFs synthesized with and without PVP. The obtained spectra display continuous extinction across the visible range and a more or less pronounced plasmon band in the 350–1100 nm region. It is interesting to note that, as the concentration of PVP increases, a broad band appears at 450 nm, and the minimum at 300 nm gradually becomes more pronounced. This optical behavior is due to the large size of the particles, which allows the excitation of multipolar plasmon modes such as quadrupole and octupole, in addition to the dipole. As predicted by plasmonic theory, the decrease in the diameter of the AgNFs from 1.7 µm to 500 nm (Fig. 1) changes the contribution of the higher-order resonances.

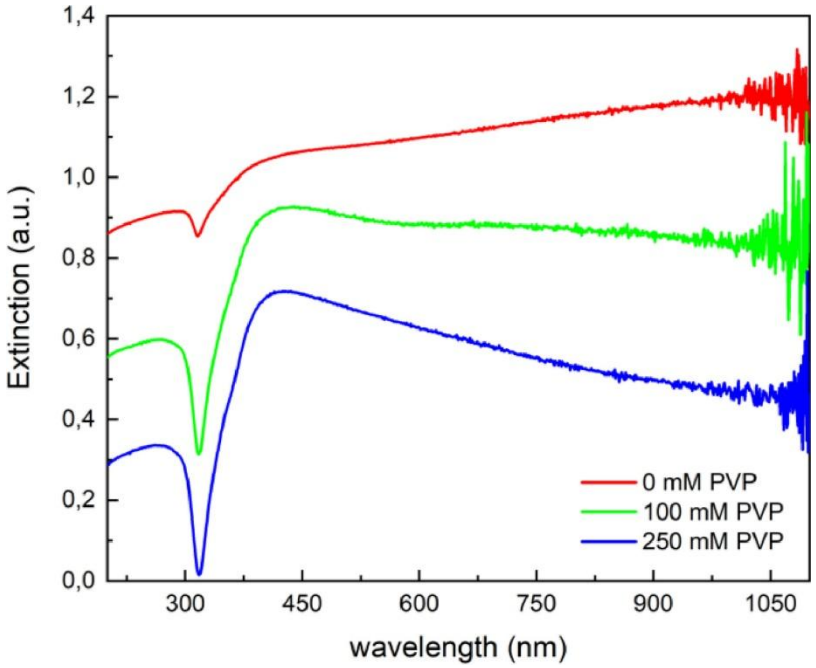

Figure 2.5. Extinction spectra of Ag NFs obtained in the absence (red line) and presence of PVP at concentrations of 100 mM (green line) and 250 mM (blue line) [11].

XPS analysis of the samples was also performed to ensure that the surface of the microstructure did not oxidize during the washing and stocking procedure, since the presence of silver oxide on the surface of the particle can worsen the plasmonic and electromagnetic field enhancement capabilities [14]. Fig. 2.6 shows the XPS analysis of AgNFs #1, #2, and sample #3.

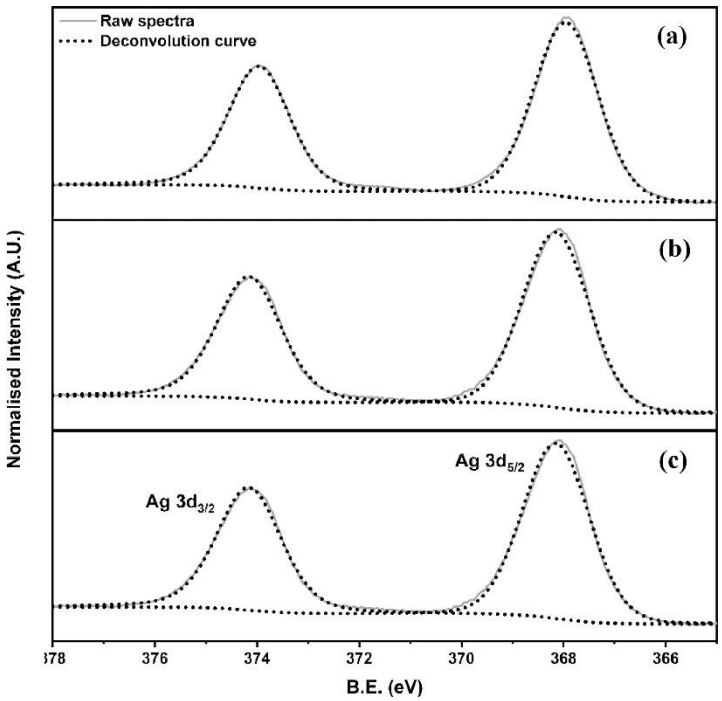

Figure 2.6. XPS spectra of AgNFs #1 (a), #2 (c), and #3 (b) [11].

AgNFs were employed as SERS substrates in Chapter 3 to calculate the enhancement factor (EF) on a single particle. In Chapter 4, they were further used to investigate their catalytic performance in a plasmon-driven reaction, monitored through SERS.

2.2 Synthesis of Silver Nanospheres an Nanoplates

To obtain nanoparticles with specific morphologies, such as Silver Nanoplates (AgNPTs), the synthesis control is necessary. The seed-mediated growth approach is one of more suitable chemical method because it is able to separate nucleation and nanoparticle growth stages controlling not only the shape but also the size of produced nanostructures, thus allowing the modulation of the characteristic resonance plasmon peak of the particles in almost the entire visible and near-infrared range as it will be explained below.

First, it is necessary to obtain the seeds of silver that are Silver Nanospheres (AgNSs). The synthesis was carried out by adding, in a beaker, 0.5 mL of a 59 mM silver nitrate ($AgNO_3$) solution and 1 mL of a 35 mM trisodium citrate (TSC) solution to 10 mL of ultrapure water (Milli-Q grade) and then stirring vigorously for 5 minutes. Then, 0.5 mL of a 20 mM sodium borohydride ($NaBH_4$) solution was added, and the reaction proceeded for 30 minutes [15]. Figure 2.7a shows the TEM of the small silver nanoparticles. Their small size is due to the synthesis method where the reduction of Ag^+ ions interact with a strong reducing agent, such as $NaBH_4$, increasing the nucleation of Ag^0 clusters. Moreover, TSC adsorbs on the surface of the nanoparticles and prevents them from agglomerating [16]. The scheme of synthesis is described in Figure 2.7b.

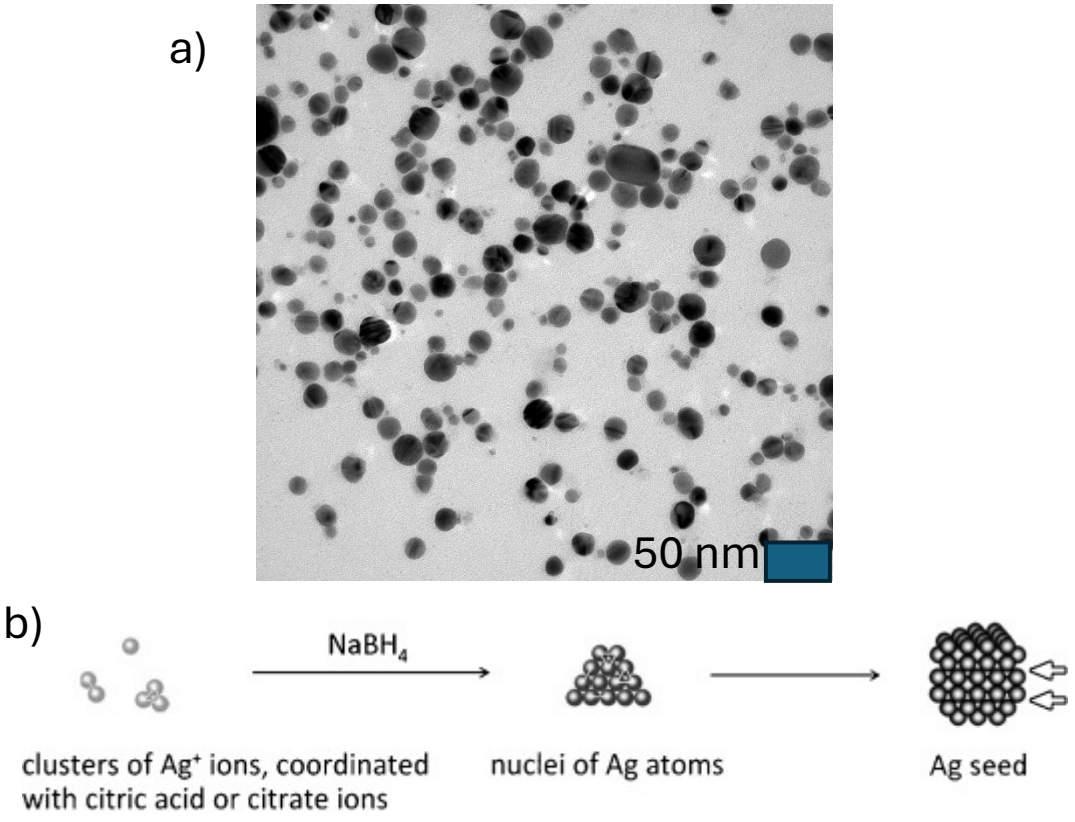

Figure 2.7. a) TEM image and b) synthesis sheme [16] of AgNSs.

Silver Nanoplates were prepared by using the seed-mediated growth approach [17]. In details, 60 μL of 400 mM TSC solution were added to 20 mL of ultrapure water. Then, 200 μL of the AgNS seeds dispersion were added while keeping the system under vigorous stirring. After 10 minutes, 50 μL of a 400 mM hydrazine (N_2H_4) solution were added. Fifteen minutes later, a nutrient solution of 0.59 mM $AgNO_3$ was slowly added over 5 minutes.

As shown in Figure 2.8, AgNPTs synthesized are very thin particles with triangular, or hexagonal shapes. To obtain these particular shapes is necessary a strong control of the reaction using specific reducing and capping agents.

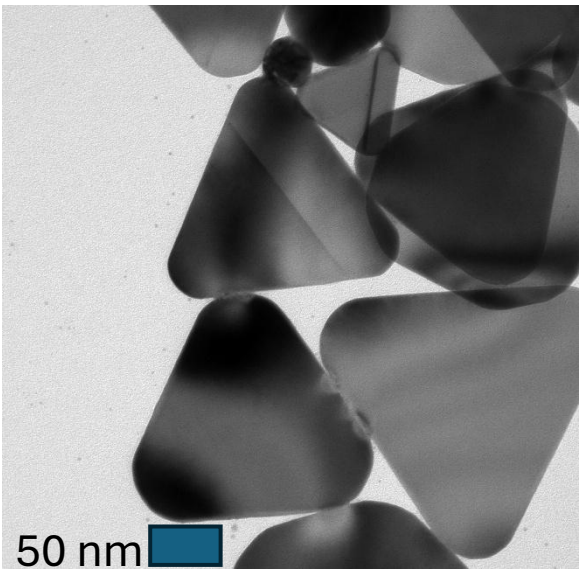

Figure 2.8. TEM images of the synthesized AgNPTs.

The reducing agent must be strong enough to reduce Ag^+ ions but, at the same time, it should prevent the formation of new nuclei. For example, if $NaBH_4$ was used, the process would not be easy controlled because this reducing agent is too strong, inducing new nuclei formation. In contrast, hydrazine (used for this work synthesis) ensures Ag^+ reduction only on pre-existing seeds and for this reason it is particularly suitable for an accurate control of the nanostructure dimensions [17].

The capping agent plays a key role in determining particle shape. The different nature of the capping agents can completely change the final nanoparticle shape. For example, in the case of TSC, typically used for AgNPTs synthesis, it binds preferentially to the 111 crystal plane of silver, leaving the orthogonal directions free to change. Thus, the growth along the 111 direction is blocked, and it only occurs along the perpendicular directions. The result is a flat particle with a hexagonal or triangular shape, depending on the degree of development [17].

Using other capping agents, it is possible to obtain different shapes. For example, Tao et al. used PVP to build silver cubes and octahedrons since silver deposits selectively onto the 100 facets [18]. Instead, Hu et al. reported the synthesis of silver nanowires using sodium dodecylsulfonate with silver growth long the 110 facets [19].

In Figure 2.9 is represented a general growth scheme of AgNPTs where the choice of TSC is necessary to block the 111 facets [20].

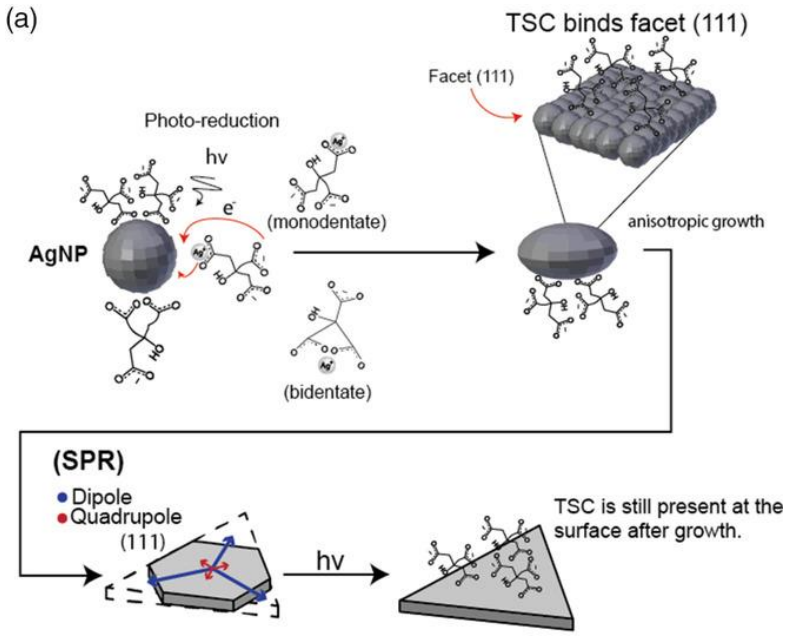

Figure 2.9. Synthesis scheme of AgNPTs [20].

The optical behaviours of AgNSs and AgNPTs are monitored with UV-Vis spectroscopy. The typical spherical shape of the AgNSs is confirmed by the UV-Vis spectrum, where the characteristic extinction peak at 410 nm is attributable to the dipolar plasmon resonance [21] (fig. 2.10, line in yellow). The extinction spectrum of AgNPTs (fig. 2.10, blue line) is due to the formation of plasmon multipoles caused by the anisotropy of the nanoparticle. Specifically, the main intense peak, at 792 nm, is attributable to the in-plane dipolar plasmon mode; at shorter wavelengths, the signals are associated with the in-plane quadrupole at 442 nm, the out-of-plane dipole at 395 nm and the out-of-plane quadrupole at 334 nm [17].

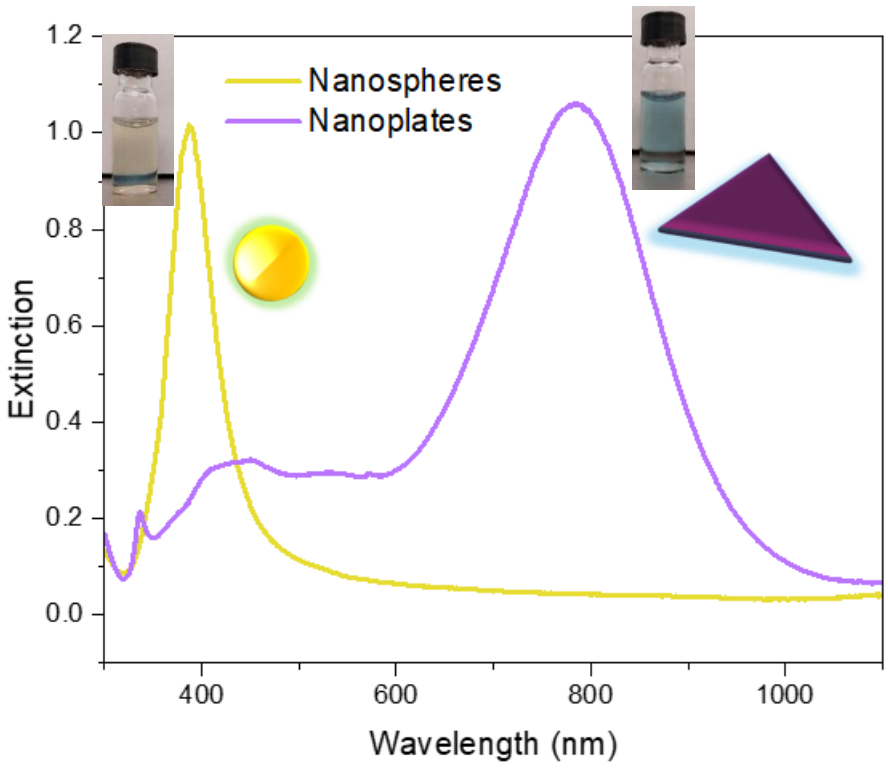

Figure 2.10. a) UV–Vis spectra of AgNSs (in yellow), AgNTPs (in blue).

AgNSs and AgNPTs were employed as SERS substrates in Chapter 4 to compare their catalytic performance with AgNFs to convert nitro group molecules to azo-compounds. Moreover, in Chapter 5, Silver Nanoplates were covered with platinum to develop a stable SERS substrate.

References

[1] E. Fazio *et al.*, "Nanoparticles Engineering by Pulsed Laser Ablation in Liquids: Concepts and Applications," *Nanomaterials 2020, Vol. 10, Page 2317*, vol. 10, no. 11, p. 2317, Nov. 2020, doi: 10.3390/NANO10112317.

[2] L. Petti *et al.*, "A plasmonic nanostructure fabricated by electron beam lithography as a sensitive and highly homogeneous SERS substrate for bio-sensing applications," *Vib Spectrosc*, vol. 82, pp. 22–30, Jan. 2016, doi: 10.1016/J.VIBSPEC.2015.11.007.

[3] B. Khodashenas and H. R. Ghorbani, "Synthesis of silver nanoparticles with different shapes," *Arabian Journal of Chemistry*, vol. 12, no. 8, pp. 1823–1838, Dec. 2019, doi: 10.1016/J.ARABJC.2014.12.014.

[4] G. Compagnini *et al.*, "Growth Kinetics and Sensing Features of Colloidal Silver Nanoplates," *J Nanomater*, vol. 2019, no. 1, p. 7084731, Jan. 2019, doi: 10.1155/2019/7084731.

[5] Q. Chang, X. Shi, X. Liu, J. Tong, D. Liu, and Z. Wang, "Broadband plasmonic silver nanoflowers for high-performance random lasing covering visible region," *Nanophotonics*, vol. 6, no. 5, pp. 1151–1160, Aug. 2017, doi: 10.1515/NANOPH-2017-0010/ASSET/GRAPHIC/J_NANOPH-2017-0010_FIG_006.JPG.

[6] R. Ma, B. Kang, S. Cho, M. Choi, and S. Baik, "Extraordinarily High Conductivity of Stretchable Fibers of Polyurethane and Silver Nanoflowers," *ACS Nano*, vol. 9, no. 11, pp. 10876–10886, Nov. 2015, doi: 10.1021/ACSNANO.5B03864/ASSET/IMAGES/NN-2015-03864J_M005.GIF.

[7] C. Muhammed Ajmal, K. P. Faseela, S. Singh, and S. Baik, "Hierarchically-structured silver nanoflowers for highly conductive metallic inks with dramatically reduced filler concentration," *Sci Rep*, vol. 6, no. 1, pp. 1–9, Oct. 2016, doi: 10.1038/SREP34894.

[8] Y. Wang, P. H. C. Camargo, S. E. Skrabalak, H. Gu, and Y. Xia, "A facile, water-based synthesis of highly branched nanostructures of silver," *Langmuir*, vol. 24, no. 20, pp. 12042–12046, Oct. 2008, doi: 10.1021/LA8020904.

[9] H. Liang *et al.*, "Enormous surface-enhanced Raman scattering from dimers of flower-like silver mesoparticles," *Small*, vol. 8, no. 22, pp. 3400–3405, Nov. 2012, doi: 10.1002/SMLL.201201081.

[10] B. Bin Xu *et al.*, "On-chip fabrication of silver microflower arrays as a catalytic microreactor for allowing in situSERS monitoring," *Chemical Communications*, vol. 48, no. 11, pp. 1680–1682, Jan. 2012, doi: 10.1039/C2CC16612G.

[11] A. Brancato *et al.*, "Ag nanoflowers as single-particle, multi-wavelength SERS active platforms," *Surfaces and Interfaces*, vol. 40, p. 103157, Aug. 2023, doi: 10.1016/J.SURFIN.2023.103157.

[12] H. You and J. Fang, "Particle-mediated nucleation and growth of solution-synthesized metal nanocrystals: A new story beyond the LaMer curve," *Nano Today*, vol. 11, no. 2, pp. 145–167, Apr. 2016, doi: 10.1016/J.NANTOD.2016.04.003.

[13] Z. Liu *et al.*, “Gold mesoparticles with precisely controlled surface topographies for single-particle surface-enhanced Raman spectroscopy,” *J Mater Chem C Mater*, vol. 1, no. 35, pp. 5567–5576, Aug. 2013, doi: 10.1039/C3TC30824C.

[14] H. Kang *et al.*, “Stabilization of Silver and Gold Nanoparticles: Preservation and Improvement of Plasmonic Functionalities,” *Chem Rev*, vol. 119, no. 1, pp. 664–699, Jan. 2019, doi: 10.1021/ACS.CHEMREV.8B00341.

[15] M. Condorelli *et al.*, “Tuning plasmonic reactivity: Influence of nanostructure, and wavelength on the dimerization of 4-NTP,” *J Catal*, vol. 450, p. 116267, Oct. 2025, doi: 10.1016/J.JCAT.2025.116267.

[16] J. Zeng *et al.*, “A Mechanistic Study on the Formation of Silver Nanoplates in the Presence of Silver Seeds and Citric Acid or Citrate Ions,” *Chem Asian J*, vol. 6, no. 2, pp. 376–379, Feb. 2011, doi: 10.1002/ASIA.201000728.

[17] G. Compagnini *et al.*, “Growth Kinetics and Sensing Features of Colloidal Silver Nanoplates,” *J Nanomater*, vol. 2019, no. 1, p. 7084731, Jan. 2019, doi: 10.1155/2019/7084731.

[18] A. Tao, P. Sinsermsuksakul, and P. Yang, “Polyhedral silver nanocrystals with distinct scattering signatures,” *Angewandte Chemie - International Edition*, vol. 45, no. 28, pp. 4597–4601, Jul. 2006, doi: 10.1002/ANIE.200601277.

[19] J. Q. Hu *et al.*, “A Simple and Effective Route for the Synthesis of Crystalline Silver Nanorods and Nanowires,” *Adv Funct Mater*, vol. 14, no. 2, pp. 183–189, Feb. 2004, doi: 10.1002/ADFM.200304421.

[20] J. Arcos-Pareja *et al.*, “Revealing the Synthesis of Triangular Silver Nanoplates: A Study of the Photochemical Growth Mechanism around the pH and Trisodium Citrate Variations,” *physica status solidi (b)*, vol. 258, no. 12, p. 2100189, Dec. 2021, doi: 10.1002/PSSB.202100189.

[21] B. J. Wiley, S. H. Im, Z. Y. Li, J. McLellan, A. Siekkinen, and Y. Xia, “Maneuvering the surface plasmon resonance of silver nanostructures through shape-controlled synthesis,” *Journal of Physical Chemistry B*, vol. 110, no. 32, pp. 15666–15675, Aug. 2006, doi: 10.1021/JP0608628.

Chapter 3

3.1 How to Choose the Wavelength of the Laser Source

Up to this point, only the fundamental theoretical aspects related to the phenomena of LSPR, Raman, and SERS have been discussed. These theoretical concepts form the essential basis for fully understanding how the techniques work and their potential, and serve as a constant reference throughout this work.

Starting from this chapter, the focus will gradually shift toward more practical aspects. Some common issues encountered in the application of the SERS technique will be analyzed, along with possible strategies and solutions developed to address them.

First of all, a Raman measurement requires a very intense monochromatic light source, which makes lasers ideal candidates. In many cases, Raman instrumentation is coupled with a confocal optical microscope, allowing measurements to provide spatial information about the sample composition. The laser beam is focused onto the sample through an objective lens. The light scattered from the sample (both Rayleigh and Raman light) is then collected by the same objective. The Rayleigh light (which has the same wavelength as the laser) must be filtered out using a notch or edge filter to observe the weaker Raman signals. After that, a monochromator selects the light, with a resolution depending on the diffraction grating, and finally, a detector records the signals and their intensities. Typically, the detector is a silicon charged-coupled device (CCD), as it is suited with laser sources ranging from the near-UV to the near-infrared [1]. Figure 3.1 shows the diagram of a typical Raman setup.

Depending on the application, the choice of the source is very important. To perform Raman or SERS measurements, the selection of the source can depend on several factors. First of all, the source must be compatible with the working range of the detector. For example, for lasers with a

wavelength higher than 1100 nm, a CCD detector is not suitable because its quantum efficiency is not sufficient [2].

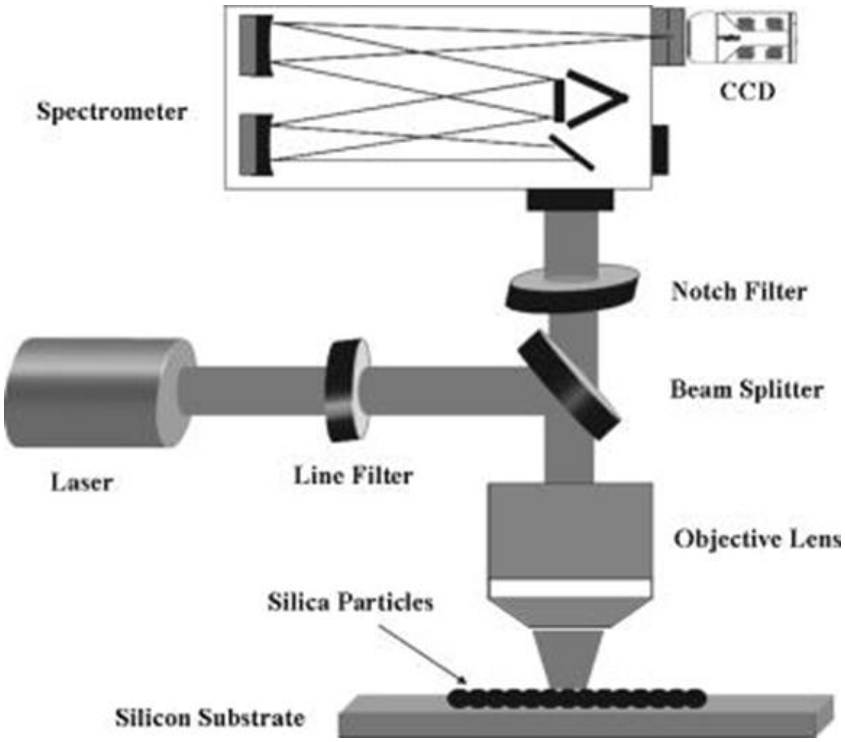

Figure 3.1. Diagram of a typical Raman setup [1].

Another important aspect to consider is that the Raman scattering cross-section of the analyte depends on the wavelength of the source. Each vibration and each molecule can interact with light in different ways, with stronger or weaker effects. In general, the intensity of the Raman signals should increase proportionally to the fourth power of the laser frequency [3]. Therefore, lasers in the near-UV will make Raman scattering much more intense compared to lasers in the near-infrared. Moreover, organic molecules used as Raman analytes can absorb light through electronic transitions in the near-UV or visible range. In these cases, the Raman effect becomes resonant, and the cross-section increases by several orders of magnitude [4].

However, in many cases, electronic transitions can cause fluorescence from the analytes or from contaminants. In many situations, the fluorescence can be so strong that it covers the Raman

signals, making them indistinguishable [2]. In addition, UV or visible radiation could modify or degrade some sensitive analytes, causing photobleaching. Therefore, using near-infrared sources can help reduce photoluminescence and the degradation of analytes. In the biological field, it is useful to use sources between 650 nm and 950 nm or from 1000 nm to 1350 nm. These ranges are the only ones where the absorption and fluorescence of human tissues are minimized, making them suitable for Raman measurements [5].

Finally, we must also take into account the optical properties of the SERS substrate, which can be responsive to the wavelength of the laser source. First of all, the nanostructure of the SERS substrates could absorb light, causing quenching of the Raman scattering. For example, knowing the imaginary part of the dielectric function of gold, it is understandable that a source with a wavelength of 600 nm or higher should be chosen. If a wavelength around 500 nm were chosen, many photons would be lost due to the interband transitions of gold [6]. Silver, on the other hand, is compatible with laser wavelengths around 500 nm.

Furthermore, as explained in Chapter 1, to achieve an enhancement of the Raman signals, the plasmonic SERS substrate must be in resonance with the incident laser light. The plasmonic resonance can depend on multiple geometric factors of the nanoparticles. For example, dimers of nanospheres can have completely different plasmonic characteristics compared to single nanospheres. Le Ru and Etchegoin presented simulations demonstrating that as two gold nanoparticles approach each other, the plasmonic resonance undergoes a pronounced red-shift. Specifically, the resonance shifts from approximately 530 nm, corresponding to a single isolated nanosphere, to about 670 nm. They also calculated the SERS enhancement factor (Fig. 3.2c), showing that the EF can increase by up to 10^8 compared to a single nanoparticle. This strong amplification is due to the intense confinement of the electric field in the gap region between the particles, which creates highly localized hot spots. In addition, the EF is wavelength-dependent, with the maximum enhancement occurring at the plasmonic extinction of the dimers [7]. These

results confirm the strong correlation between the geometric features of the nanostructure, its plasmonic resonance, and the resulting EF.

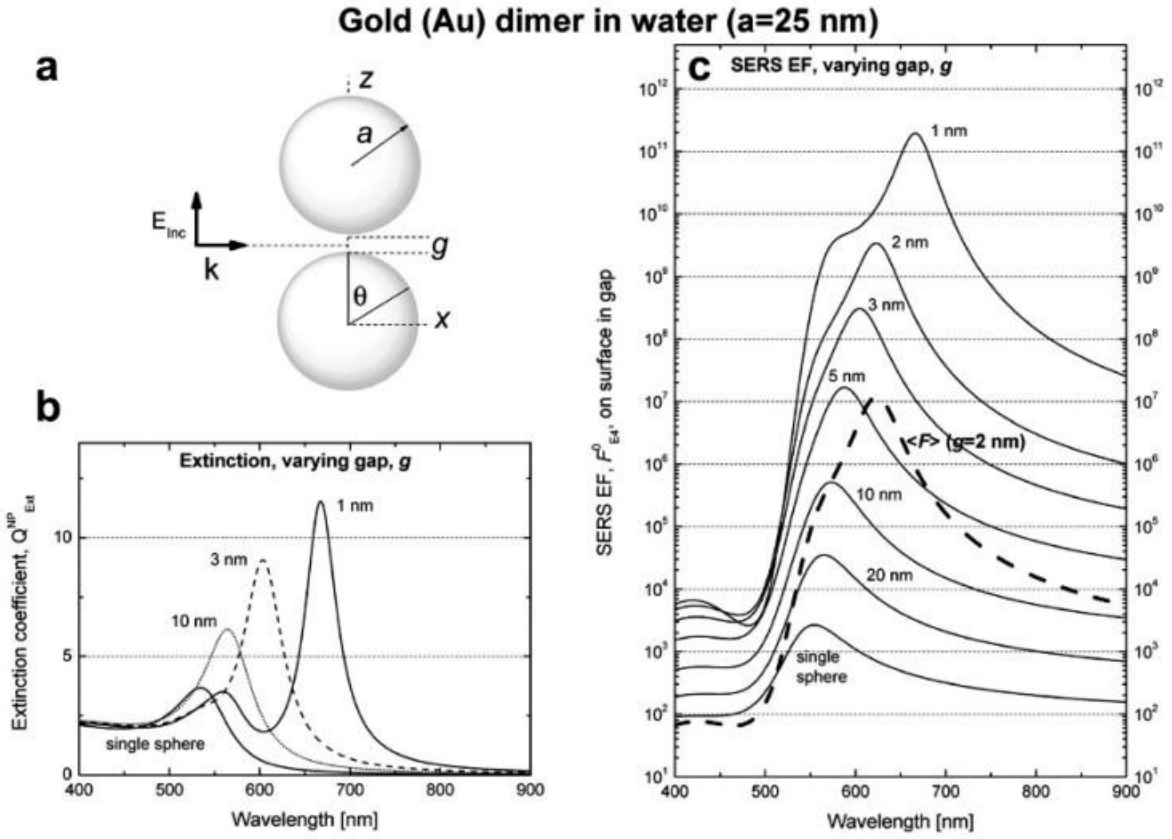

Figure 3.2 a) The dimer is formed by two gold nanoparticles with a radius of 25 nm and separated by a variable gap. b) Simulated extinction spectra for a single sphere and the dimers as a function of the wavelength. c) SERS enhancement factors for a single sphere and the dimers as a function of the wavelength [7].

Experimentally, the EF has a strong connection with the plasmonic characteristics of the SERS substrate and it has also been confirmed by McFarland et al. fabricating different substrates with varying plasmonic characteristics and, consequently, distinct extinction spectra. Benzenethiol was used as the Raman analyte adsorbed on the substrate surface. By using different excitation wavelengths, they have observed how the EF varied depending on the wavelength. finding that the maximum EF corresponds with the extinction spectra of the substrates, with a slight shift due to the vibrational and adsorption characteristics of the analyte on the substrate (fig. 3.3) [8].

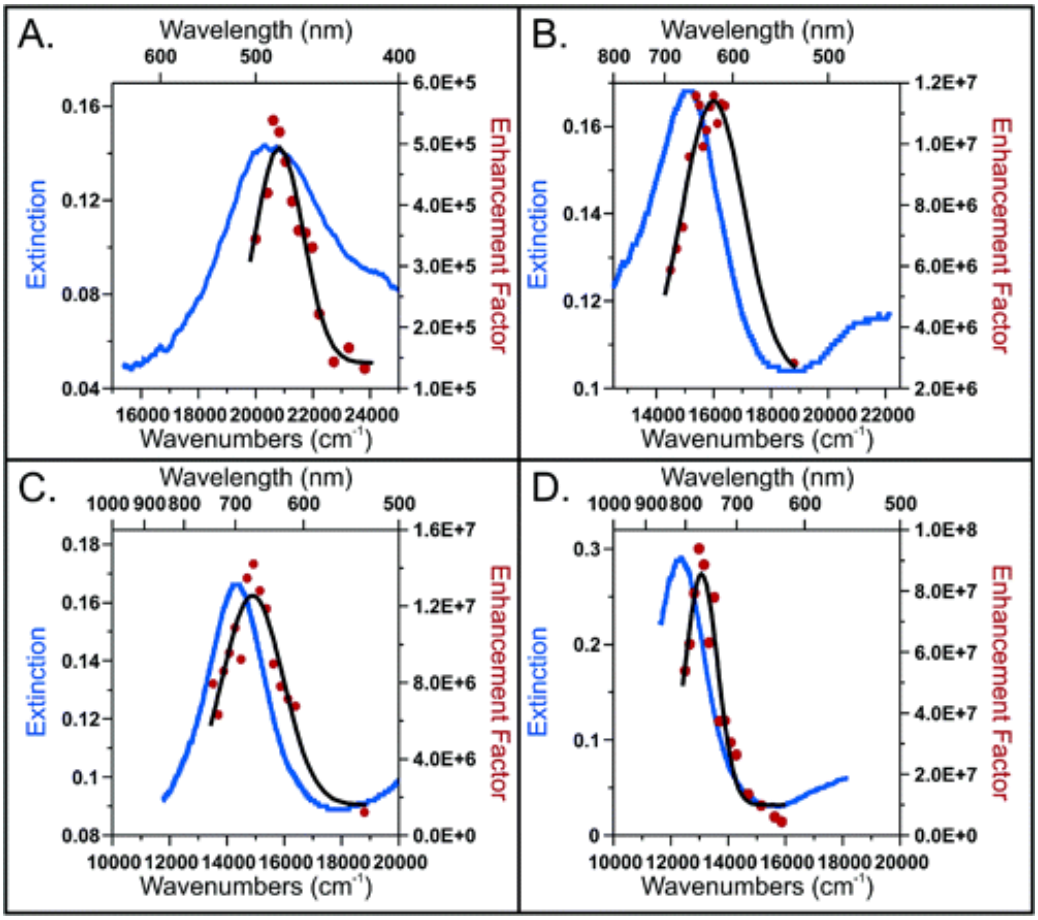

Figure 3.3. Extinction spectra and corresponding EF as a function of the laser wavelength [8].

In conclusion, the choice of exciting laser must be matched to both the application and the substrate. However, this would require access to multiple lasers with different wavelengths or tunable sources, which is often not practical due to logistical limitations, instrument incompatibilities, and high costs. A more practical approach is to design and fabricate substrates that are compatible with the available laser.

3.2 AgNFs as a Multi-Wavelength SERS Platform

The goal of this section is to obtain a SERS substrate that can be universally used with several laser wavelengths and Silver Nanoflowers seem to be the ideal candidate thanks to their optical properties showed in Chapter 2. The strong broad extinction along the visible an NIR range are connected with the size of the particles and simulation are carried out to better understand the plasmonic behaviour of big size particles as AgNFs. In figure 3.4 is showed the relative intensity (fig. 3.4a) and the absorption and scattering cross-section (fig. 3.4b) of different silver nanospheres with increasing diameters, calculated using the finite element software COMSOL Multiphysics. When the size of the nanosphere is much smaller than the incident wavelength (for example, 30 nm), we can observe the dipole plasmon resonance, which appears in the spectrum at a wavelength of about 400 nm. When the nanoparticle diameter increases to 100 nm, the dipole resonance undergoes a red shift to about 470 nm, and higher-order resonances (quadrupole mode) appear around 400 nm. For sizes up to the micrometer scale, a continuous extinction is obtained across the entire spectrum. The oscillations in the simulated extinction spectra correspond to resonances of surface plasmon modes propagating around the particles (dipole, quadrupole, octupole, etc.). Figure 3.4b shows that the extinction spectrum of a colloid of silver spheres with a 1 μm diameter is almost entirely due to scattering. Therefore, thanks to the strong interaction with the electromagnetic field throughout the VIS-NIR range, it could be used as a SERS substrate with different laser excitation wavelengths.

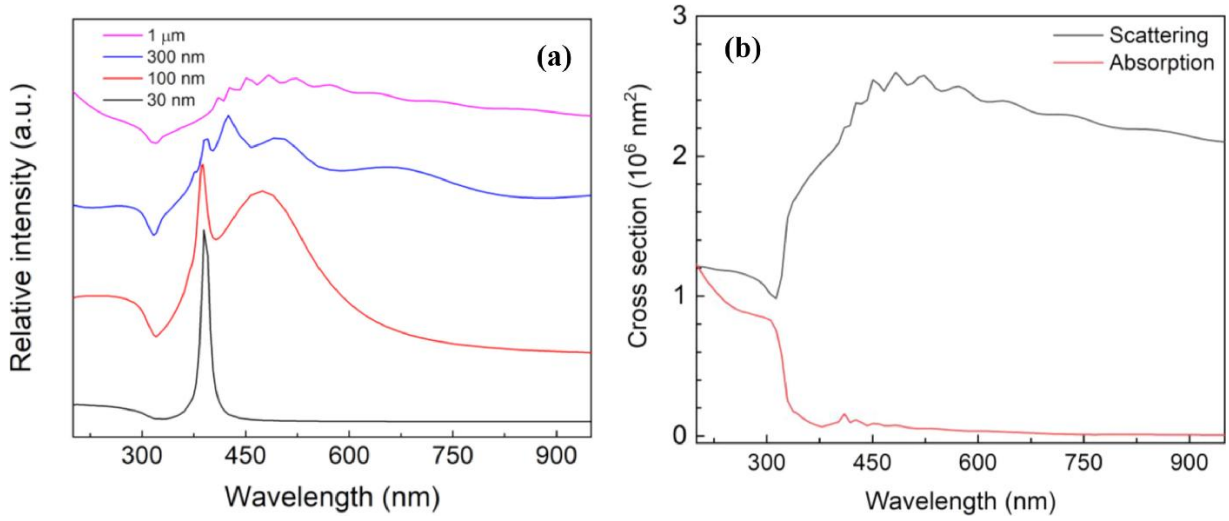

Figure 3.4. a) The simulated extinction cross-section of Ag spheres with a diameter ranging from 30 nm to 1 μm immersed in water (the curves are shifted arbitrarily along the Y axis for a better understanding). b) The scattering and absorption cross-section for an Ag sphere with 1 μm diameter [9].

The chosen analyte for the SERS test is 4-mercaptobenzoic acid (4-MBA) (fig. 3.5a). This molecule has an aromatic ring with a carboxylic group (-COOH) and a thiol group (-SH) in the para position. Both functional groups can interact with the silver surface, allowing the molecule to adsorb onto it [10].

First, the normal Raman spectra (in the absence of silver nanoflowers) of a 1 M ethanolic solution of 4-MBA were acquired by using a confocal micro-Raman spectrometer (WITEC Alpha r100), with three laser wavelengths: 532, 632, and 785 nm. The laser used for the normal Raman measurement is the 532 nm with a power of 15 μW to avoid analyte degradation and a 100x objective. The acquisition time was 10 seconds with 10. A spectrum of the pure solvent was also acquired beforehand with the same experimental conditions as a blank and then subtracted from the analyte spectrum to isolate the peaks of 4-MBA. The only two peaks observed in the normal Raman spectrum, shown in Figure 3.5b, are centered at 1078 cm^{-1} and 1580 cm^{-1}, and are associated, respectively, with δ(CH) in-plane bending and ν(CC) stretching of the aromatic ring [11]. The most intense peak, centered at 1580 cm^{-1} in the normal Raman spectrum, was chosen for the estimation of the enhancement factor (EF).

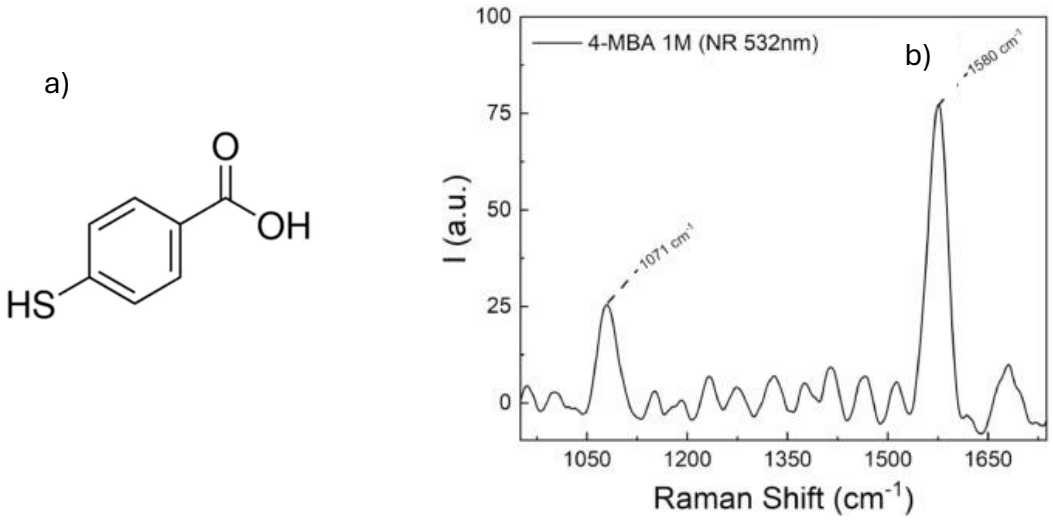

Figure 3.5. a) Representation of the molecule p-mercaptobenzoic acid (4-MBA). b) Raman spectrum of 4-MBA at a concentration of 1 M with an excitation wavelength of 532 nm [9].

As showed in Figure 3.6, to prepare the SERS samples, 2.0 mg of AgNFs were weighed and dispersed in 2 ml of ethanolic solutions of 4-MBA at different concentrations (10^{-8}, 10^{-6}, 10^{-4} M). The resulting mixture was left to rest for 24 hours to promote interaction between the NFs and the 4-MBA and then centrifuged. The supernatant solution was separated, and a UV spectrum was recorded by monitoring the signal of 4-MBA at around 270 nm. By comparing the absorbance difference with the ethanolic solution before the 24 hours, it was possible to estimate the number of 4-MBA molecules adsorbed on the NFs.

Then, the AgNFs with 4-MBA adsorbed on their surface were redispersed in 2 ml of ethanol, and one drop was placed on a silicon substrate and left to dry as the ethanol quickly evaporated. As shown in figure 3.6, the individual microparticles are distinguishable and well separated from each other.

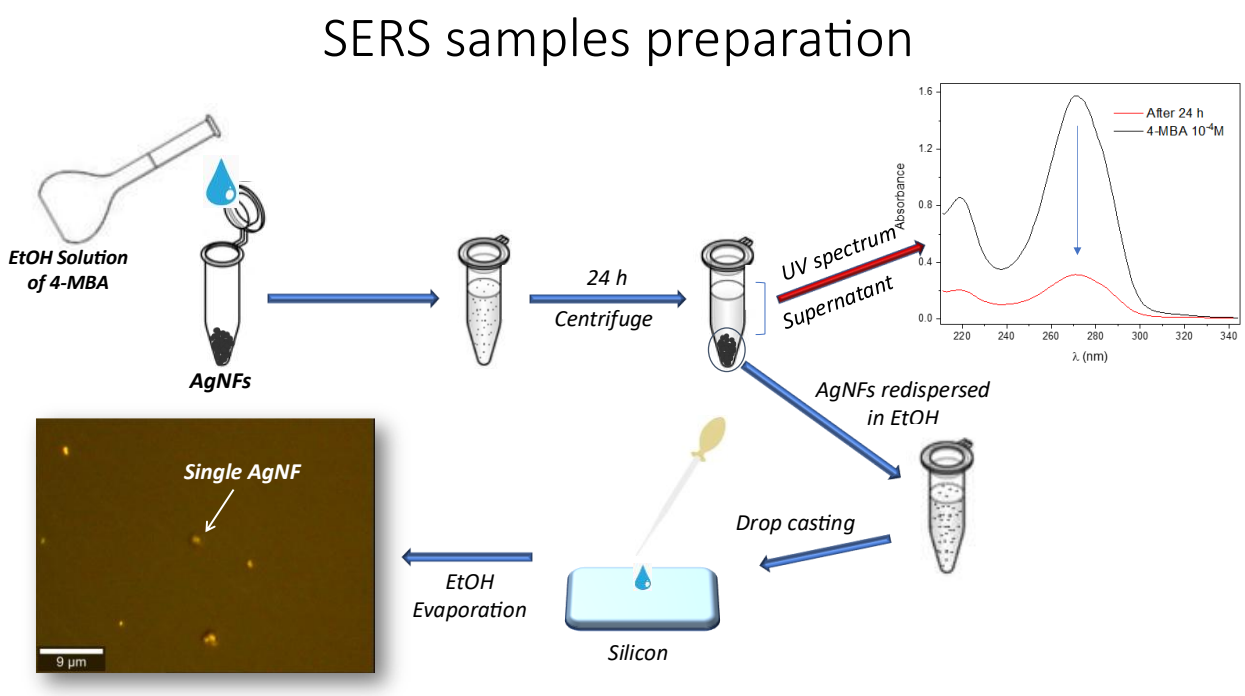

Figure 3.6. Diagram of the SERS sample preparation process.

.

The distinctive feature of silver nanoflowers compared to conventional metal nanoparticles is mainly in their large size, which makes them easily visible even with an optical microscope. By combining the Raman system with a confocal microscope, it is possible to direct the laser beam precisely onto a single flower. This setup offers a simple and practical way to perform SERS measurements on individual particles (single particle-SERS) (fig. 3.7b).

Figure 3.7a shows the SERS spectra in the presence of AgNFs at different concentrations of 4-MBA. As expected, the 4-MBA signals are several orders of magnitude more intense than those of normal Raman spectra, additionally, new signals can be identified, including a very intense new peak at 1365 cm^{-1} related to the ν(COO^-) vibration [11]. The possibility of distinguishing the Raman signals of 4-MBA at low concentrations shows that AgNFs could be powerful enough to allow detection at sub-nanomolar concentrations, thanks to their highly rough and nanostructured surface rich in hot-spots, which are concentrated at the tips and cavities of the particles, making AgNFs a potentially very sensitive substrate.

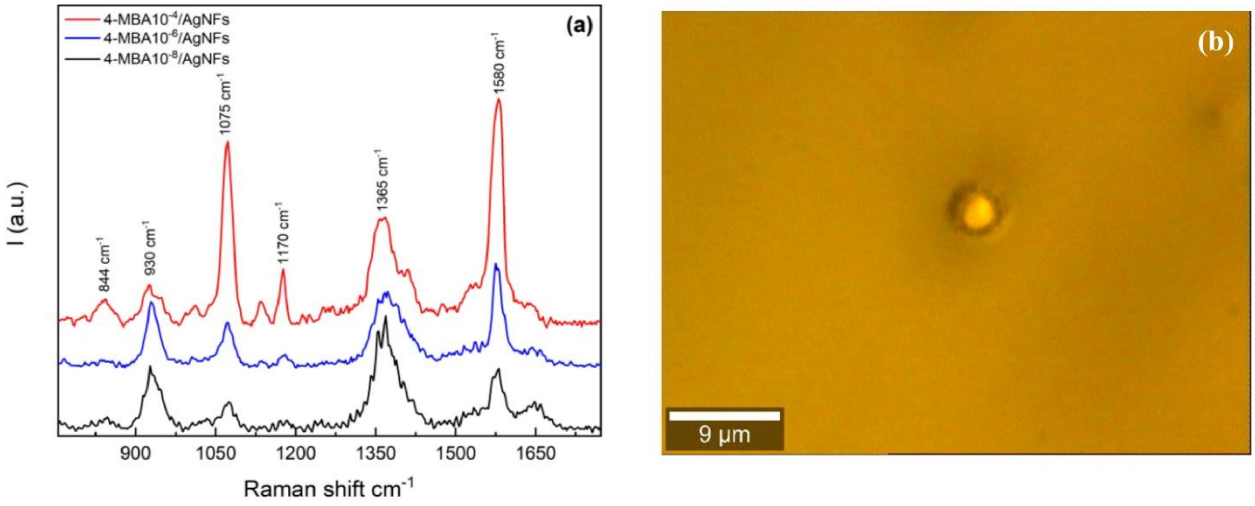

Figure 3.7. a) SERS spectra of 4-MBA (10^{-4} M to 10^{-8} M concentration range) on the same single AgNF at a laser excitation wavelength of 532 nm; b) Optical image of a single AgNF deposited onto a Silicon substrate (optical magnification 100x) [9].

Subsequently, SERS spectra were acquired for a 4-MBA concentration of 10^{-6} M using the three available laser wavelengths (532 nm, 632 nm, 785 nm). The spectra were compared with the normal Raman spectra, showing that strong enhancement occurs at all tested wavelengths (fig. 3.8a, 3.8b, 3.8c). In Figure 3.8d are shown the normal Raman spectra for the three excitation wavelengths used with very weak signals.

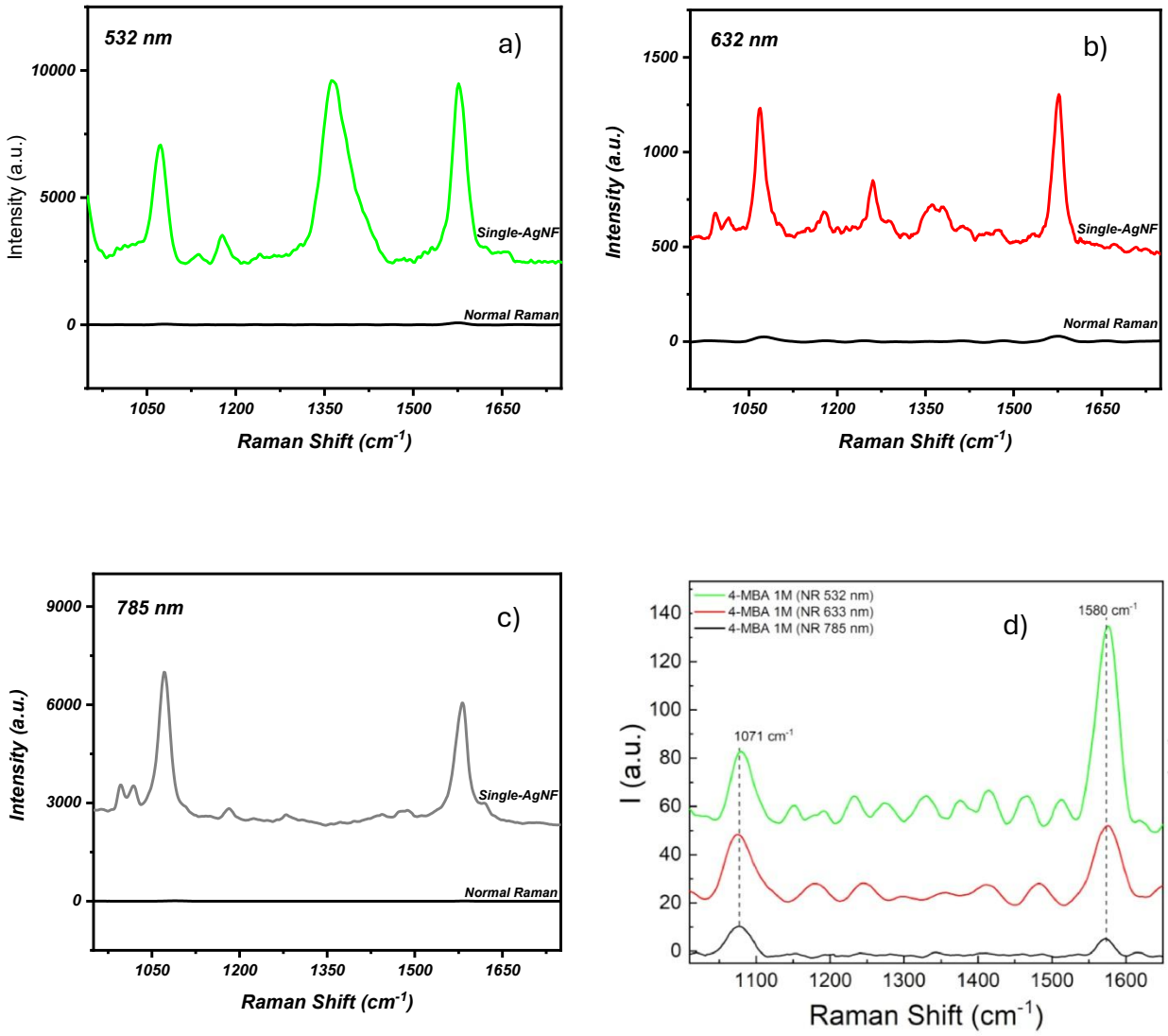

Figure 3.8. SERS spectra compared with normal Raman using lasers at a) 532 nm, b) 632 nm, c) 785 nm. d) Normal Raman spectra for the three wavelengths used [9].

To evaluate the wavelength-dependent enhancement efficiency of AgNFs, the Enhancement Factor (EF) was calculated using equation (19) from chapter 1.

I_{SERS} is the value of the signals at 1585 cm^{-1} in the spectra of Figures 3.8a, 3.8b, and 3.8c. I_{Raman} can be obtained in the same manner from Figure 3.8d.

To calculate quantitatively the EF, it is necessary to estimate the number of molecules within the laser scattering volume for the normal Raman measurement (N_{Raman}), and the number of molecules adsorbed on a single AgNF (N_{SERS}).

Knowing that the laser spot diameter is 1.8 μm, the scattering volume can be approximated as spherical. Therefore, the number of molecules probed in normal Raman is:

$$N_{Raman} = V_{scattering} C N_A \tag{25}$$

Where C is the analyte concentration (1 M) and N_A is Avogadro's number. The number of molecules adsorbed on a single AgNF is given by the ratio between the total number of 4-MBA molecules transferred from the solution to the AgNFs (N_{4-MBA}), estimated via UV spectroscopy in Fig. 3.6, and the number of AgNFs dispersed in the ethanolic solution (N_{AgNFs}). Therefore:

$$N_{SERS} = \frac{N_{4-MBA}}{N_{AgNFs}} = \frac{N_A \; V_{MBA\,solution} \; C}{\left(\frac{Weigth\,of\,Ag}{Density\,of\,Ag}\right) \Big/ V_{AgNF}} \tag{26}$$

Here, N_A is again Avogadro's number, $V_{MBA\,solution}$ is the volume used (2 ml) to prepare the samples, and C is the 4-MBA concentration of 10^{-6} M. The volume of a single AgNF (V_{AgNF}) is estimated from the average dimensions measured by SEM. Meanwhile, the weight of silver used per prepared sample is 2.0 mg.

The EF was calculated obtaining the following values for each of the three laser wavelengths: $EF_{532\ nm}$= 1,68 × 10^4, $EF_{632\ nm}$= 3,00 × 10^3, $EF_{785\ nm}$= 6,65 × 10^4. The highest enhancement is achieved by exciting the AgNFs with the 785 nm wavelength. This result opens the possibility of using IR radiation, which is not absorbed by most organic molecules, thus avoiding unwanted effects such as molecular degradation or luminescence, for the study of various biologically and medically relevant analytes.

Furthermore, the single AgNF enables analyte detection and identification even at very low concentrations, maintaining this capability regardless of the specific wavelength used to excite the nanostructures.

This result demonstrates that the detection performance of AgNF is not limited to a narrow spectral range, opening up the possibility of studying and monitoring a wide variety of analytes at trace levels with a free choice of excitation wavelength. Consequently, potential spectral interference or wavelength-dependent limitations can be minimized or completely avoided.

References

[1] K. J. Yi, H. Wang, Y. F. Lu, and Z. Y. Yang, "Enhanced Raman scattering by self-assembled silica spherical microparticles," *J Appl Phys*, vol. 101, no. 6, p. 8, Mar. 2007, doi: 10.1063/1.2450671/1028031.

[2] R. Pilot, R. Signorini, C. Durante, L. Orian, M. Bhamidipati, and L. Fabris, "A Review on Surface-Enhanced Raman Scattering," *Biosensors (Basel)*, vol. 9, no. 2, p. 57, Jun. 2019, doi: 10.3390/BIOS9020057.

[3] G. Keresztury, "Raman Spectroscopy: Theory," *Handbook of Vibrational Spectroscopy*, Dec. 2001, doi: 10.1002/0470027320.S0109.

[4] D. P. Strommen and K. Nakamoto, "Resonance raman spectroscopy," *J Chem Educ*, vol. 54, no. 8, pp. 474–478, 1977, doi: 10.1021/ED054P474..

[5] A. M. Smith, M. C. Mancini, and S. Nie, "Bioimaging: Second window for in vivo imaging," *Nat Nanotechnol*, vol. 4, no. 11, pp. 710–711, 2009, doi: 10.1038/NNANO.2009.326.

[6] S. A. Maier, "Plasmonics: Fundamentals and applications," *Plasmonics: Fundamentals and Applications*, pp. 1–223, 2007, doi: 10.1007/0-387-37825-1.

[7] E. C. Le Ru and P. G. Etchegoin, "Principles of Surface-Enhanced Raman Spectroscopy," *Principles of Surface-Enhanced Raman Spectroscopy*, 2009, doi: 10.1016/B978-0-444-52779-0.X0001-3.

[8] A. D. McFarland, M. A. Young, J. A. Dieringer, and R. P. Van Duyne, "Wavelength-scanned surface-enhanced Raman excitation spectroscopy," *Journal of Physical Chemistry B*, vol. 109, no. 22, pp. 11279–11285, Jun. 2005, doi: 10.1021/JP050508U.

[9] A. Brancato *et al.*, "Ag nanoflowers as single-particle, multi-wavelength SERS active platforms," *Surfaces and Interfaces*, vol. 40, p. 103157, Aug. 2023, doi: 10.1016/J.SURFIN.2023.103157.

[10] H. Kang *et al.*, “Stabilization of Silver and Gold Nanoparticles: Preservation and Improvement of Plasmonic Functionalities,” *Chem Rev*, vol. 119, no. 1, pp. 664–699, Jan. 2019, doi: 10.1021/ACS.CHEMREV.8B00341.

[11] C. H. Ho and S. Lee, “SERS and DFT investigation of the adsorption behavior of 4-mercaptobenzoic acid on silver colloids,” *Colloids Surf A Physicochem Eng Asp*, vol. 474, pp. 29–35, Jun. 2015, doi: 10.1016/J.COLSURFA.2015.03.004.

Chapter 4

4.1 Plasmon-driven reactions monitored by SERS

Raman and SERS techniques can be used to monitor the development of a chemical reaction due to their capability to record and monitor in real time the formation of chemical species [1]. It is well known that Raman spectroscopy detects the active molecular vibrations and that each vibration is associated with a specific molecular functional group and with a corresponding vibrational energy. At the same time, by exploiting the laser source of this technique, it is possible to start chemical transformations. In this study, the attention was focused on the investigation of the photo-stimulated chemical reactions involving the functional groups of the 4-MBA molecule, As reported in the Raman spectra of figure 4.1, this molecule is characterized by a peak at 1078 cm^{-1}, associated with δ(CH) in-plane bending while the signal at 1365 cm^{-1} is related to the ν(COO^-) vibration and the one at 1580 cm^{-1} corresponds to the ν(CC) stretching of the aromatic ring [2].

Therefore, if Raman signal intensities change over time, it could be that the molecules are being modified in new species. For instance, under certain conditions, 4-MBA molecules can undergo decarboxylation, losing the carboxylic functional group. This loss transforms the molecule into benzenethiol (BT), and the 1365 cm^{-1} peak related to the ν(COO^-) vibration disappears. Moreover, two new signals appear at 998 and 1022 cm^{-1}, indicating that decarboxylation has occurred. These peaks are typical of thiophenols (fig. 4.1) [3].

During the decarboxylation of 4-MBA, the aromatic group remains unchanged, so the peaks at 1078 and 1580 cm^{-1}, associated with δ(CH) in-plane bending and ν(CC) stretching of the aromatic ring respectively, are always visible and almost stable in intensity. Thus, one of the advantages of the Raman technique is the ability to observe a reaction as it happens.

It is well known that many chemical reactions can only occur in presence of hazardous reagents and highly polluting environmental conditions [4]. However, some interesting green alternatives have been developed for example by using photocatalysts such as TiO_2 and ZnO often coupled with noble metals in order to harness plasmon resonance properties for an enhanced photocatalysis. [5]. In addition, some studies have shown that the electrons, collectively excited in plasmon resonance of metallic particles are also able to directly drive chemical reactions [6].

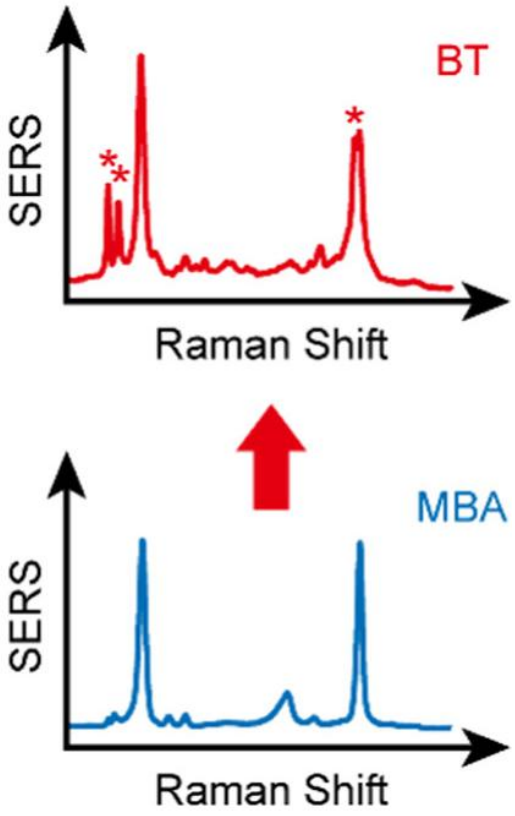

Figure 4.1. SERS spectra of 4-MBA (in blue) before irradiation, and of BT (in red) after irradiation [3].

When a plasmon mode is excited, electrons move to a higher-energy state and can be transferred into the lowest unoccupied molecular orbitals (LUMO) of adsorbed molecules, sometimes promoting reactions involving a change in functional groups (fig. 4.2) [7]. The electrons

transferred from the metal particle to the adsorbed molecule are named hot electrons, and they are concentrated near the so-called hot-spots, increasing the probability of transfer.

In addition, it is well known that noble metal nanoparticles can be exploited in the Raman technique to enhance vibrational features and to get SERS measurements. Keeping in mind what has just been discussed, the coupling of the SERS technique with the possibility to induce plasmon-driven reactions during a SERS measurement is a really exciting green approach to investigate, in real time, mechanisms involved in the chemical reactions. More explicitly, the laser source of an appropriately chosen wavelength excites the plasmonic substrate, composed by metal nanoparticles, which can transfer electrons to the adsorbed molecules. If several spectra are recorded over time, changes in the relative intensities of the signals can be observed [1], [3].

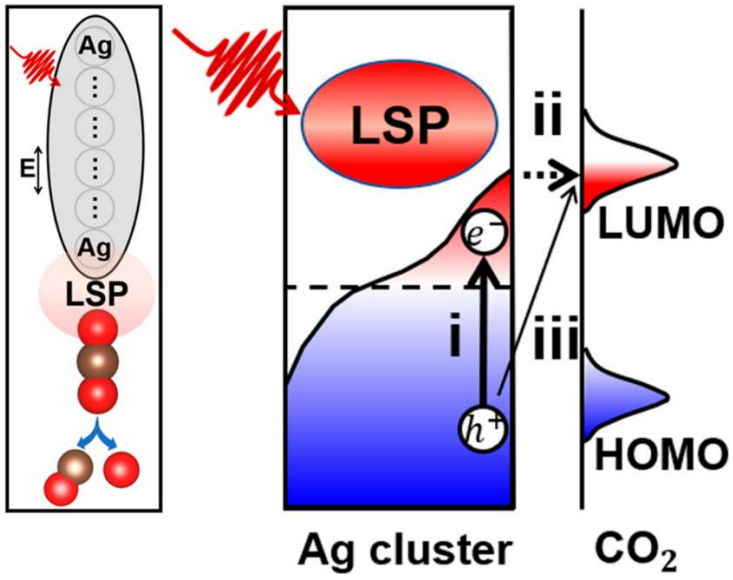

Figure 4.2. Plasmon-driven reaction scheme for CO_2 photoreduction on irradiated silver substrate [8].

Many plasmon-induced reactions, such as decarboxylation [3], dehalogenation [9], graphitization [10], and polymerization [11], have already been studied in depth by researchers. For example, the dissociation of the carbon-halogen bond on gold nanoparticles was investigated by R. Schürmann et al. and it was found that the reaction rate changed with the laser wavelength but was independent

of the type of halogen atom. It was also explained that the process was mainly driven by the optical properties of the nanoparticles [9].

In another study, an important result was reported by H. Huh et al. [3], regarding the decarboxylation of 4-MBA in presence of gold nanostructures. It was highlighted that the process was more efficient with a 785 nm laser source than a 532 nm one and this behaviour was attributed to the excitation of a LSPR mode located at around 730 nm.

Many factors affect the efficiency of a chemical reaction, among them the geometry of metallic nanoparticles which plays a crucial role in plasmonic properties and also the distribution and density of hot-spots which are highly dependent on the shape and size of the particles. For example, an improvement in plasmonic photocatalysis near hot-spots on aluminum particles (such as octopods or nanocubes) during hydrogen dissociation has also been reported [12]. Tip Enhanced Raman Spectroscopy (TERS) studies have further shown that, in silver particles, reactions occur mainly at the edges, where the electric field is most strongly localized [13].

In this chapter, the reduction of 4-nitrothiophenol (4-NTP) to dimercaptoazobenzene (DMAB), its dimer, will be considered. This is one of the most studied model reactions for plasmon-driven chemistry, as it helps in understanding the mechanisms of hot-electron transfer [14].

Under plasmonic excitation, the 4-NTP molecules adsorbed on silver nanostructures undergo electron transfer from the metal, activating the nitro group. This process promotes a surface-assisted dimerization, leading to the formation of DMAB through N=N bond coupling. Alternatively, depending on chemical environments conditions and electron transfer can follow a reduction pathway, yielding 4-ATP via conversion of the nitro group to an amine.

In this study, the plasmonic substrates were silver nanoparticles in the form of nanospheres (AgNSs), nanoplates (AgNPTs) and nanoflowers (AgNFs) and two laser sources respectively at wavelength of 532nm and 785 nm. Among the main results by using the 532 nm laser radiation, a

strong correlation between the morphology of the metallic particles (i.e. number of hot spots) and the reaction kinetics for the conversion of 4-NTP into DMAB was found.

Furthermore, an interesting behaviour on the product formation was observed on AgNFs by using a 785 nm laser. In this case, the reduction of 4-NTP to 4-aminothiophenol (4-ATP) and not to DMAB was observed. This result is remarkable, considering that the reduction of 4-NTP to 4-ATP usually requires reducing agents such as $NaBH_4$ [15] or HCl [16].

4.2 Influence of nanostructure and wavelength on the dimerization of 4-NTP

The preparation of three SERS substrate was carried out with the AgNS, AgNPT, and AgNF colloids were obtained, anchoring them to a silicon wafer according to the following procedure [17] schematically reported in fig. 4.3. In detail, some silicon pieces slices were immersed in a reverse piranha solution (H_2SO_4:H_2O_2 = 1:3) for 30 minutes at 90 °C. The silicon substrates were then rinsed in Milli-Q water and immersed in a 10 mL of (3-aminopropyl)triethoxysilane (APTES) solution for 30 minutes. After that, the silicon pieces were immersed in the three different silver colloid dispersions, all characterized by an extinction intensity of∼1, for a time of 30 minutes (fig. 4.3).

By this way, silver metallic particles can be anchored to APTES-functionalized silicon substrates thanks to strong electrostatic attraction. These charge interactions arise because APTES molecules positively charge the silicon surface, while the metallic particles have a negatively charged surface due to the presence of the employed capping agents.

Finally, each of the three substrates was immersed in an aqueous solution of 4-NTP at a concentration of 10^{-4} M for 24 hours (fig. 4.3). Afterwards, the substrates were rinsed with water to remove unbound molecules and were left to dry for one day.

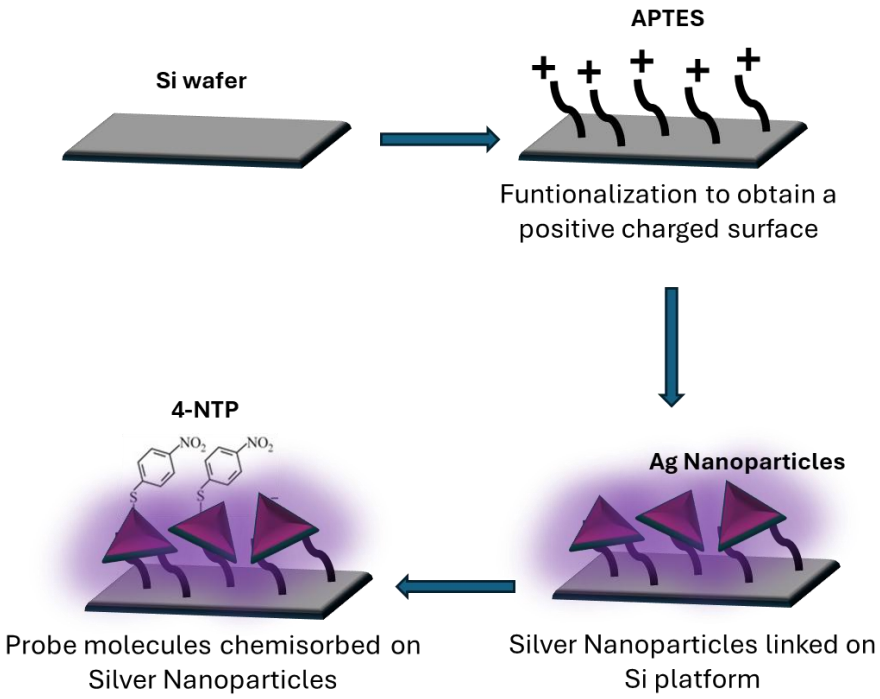

Figure 4.3. SERS substrates fabrication scheme.

In Figure 4.4a, the molecular structure of the 4-NTP is shown, the molecule is characterized by the presence of an aromatic ring bonded in para to a thiol group (useful for binding to silver) and to a nitro group (the reactive side). As you can see in Figure 4.4b, the molecule adsorbed on the three different plasmonic substrates was characterized by SER spectroscopy by using an exciting wavelength of 532 nm. Particularly, SERS spectra of 4-NTP molecules at a concentration of 10^{-4} M adsorbed on AgNSs (in yellow), AgNPTs (in blue), and AgNFs (in black) only differ for the intensity of vibrational signals. It is important to highlight that the characteristic signals of 4-NTP at 1075 cm^{-1} (νC–S), 1334 cm^{-1} (νsNO₂), and 1570 cm^{-1} (νC–C, aromatic ring stretching) are visible thanks to the signal enhancement due to the presence of nanostructure, otherwise not easily detectable.

In particular, AgNFs are able to generate stronger vibrational signals compared to the plasmonic platforms of AgNPTs and AgNSs. This is due to the finely nanostructured surface of the flowers.

The petals on the surface act like tips capable of amplifying the electric field, and the interparticle spaces between petals create a high number of intrinsic hotspots [18].

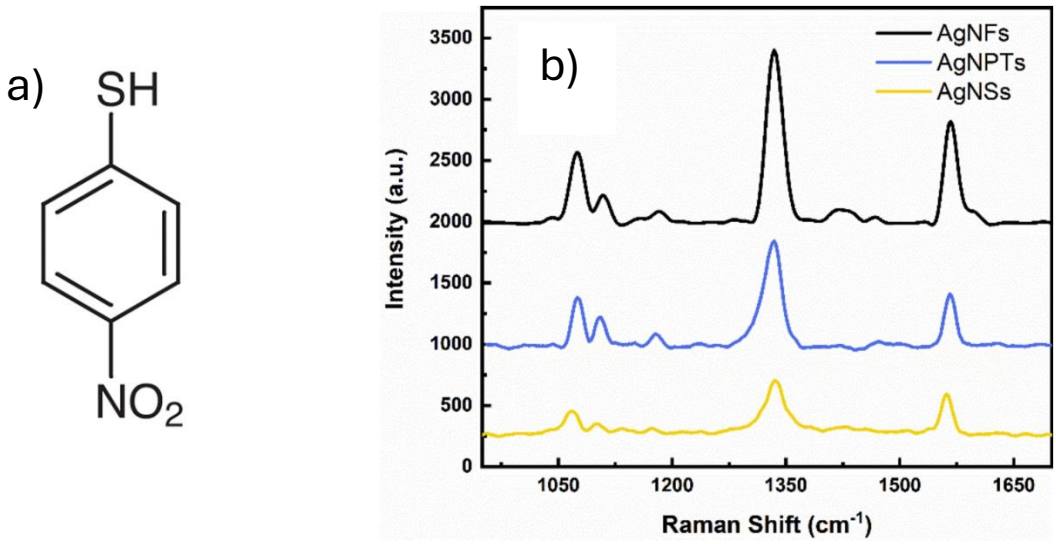

Figure 4.4. a) 4-NTP molecule. b) SERS spectra of 4-NTPs on AgNSs (yellow), AgNPTs (blue), and AgNFs (black).

In contrast, AgNSs show the weakest signals due to the absence of surface structures on nanoscale or tips. Moreover, their plasmon peak is far from the excitation wavelength (532 nm).

On the other hand, when using AgNPTs as a substrate, the peaks characteristic of the 4-NTP show a higher intensity than those recorded on the AgNSs thanks to the presence of tips which act as hotspots, increasing locally the electric field of the incoming light by several orders of magnitude. However, the signals are weaker than those observed on AgNFs. In fact, AgNPTs, have a lower hotspot density than AgNFs and also a lower ability to adsorb 4-NTP molecules on the almost flat surface.

The characterized samples were then employed for the dimerization reaction of 4-NTP. For kinetic comparison studies among the three substrates, a 532 nm wavelength laser was used, the same source employed during SERS measurements. The SERS spectra were acquired by focusing the beam through a 100x objective, with an acquisition time of 0.5 s per spectrum and 5 accumulations.

The SERS spectra of all samples were then recorded continuously over a period of 10 minutes. To monitor the reaction, the laser power was set to 20 μW. Lower powers could be difficult to control due to value fluctuations, while higher powers did not allow to monitor the reaction because of the sudden conversion. The same laser power was used for salmples of 4-NTP linked with AgNSs, AgNPTs, and AgNFs. In the case of the AgNF SER substrate, it was also possible to study the kinetic reaction performing single-particle measurements thanks to their micrometric size, as already discussed in Chapter 2. Anyhow in all samples, by monitoring the evolution of the SERS spectra over time, it was possible to observe the formation of DMAB on the silver particles (fig. 4.5), even if best results were obtained when AgNFs were employed. Precisely for this reason, they will be discussed first and then compared with the other two types of silver nanoparticles (nanospheres and nanoplates).

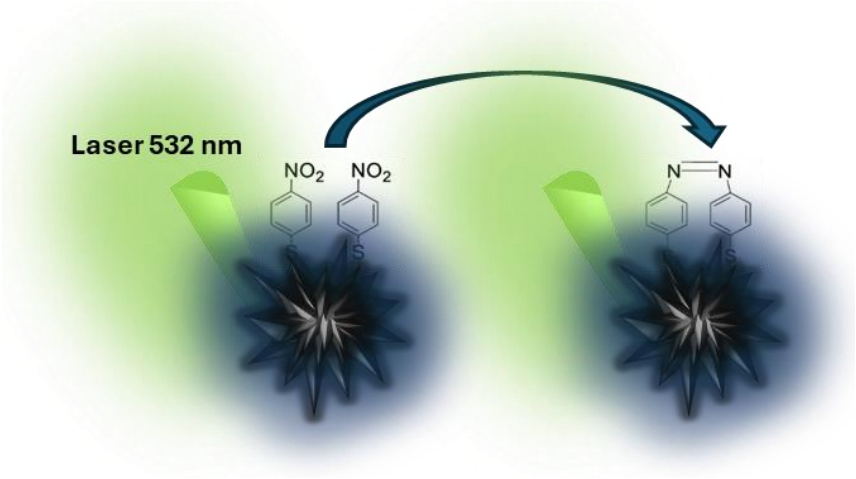

Figure 4.5. Scheme of 4-NTP reduction into DMAB on Silver particle, triggered by 532 nm laser.

SERS spectra recorded on a single AgNF (fig. 4.6a and 4.6b) show clearly the conversion of 4-NTP into the reaction product DMAB, thanks to the appearance of signals at 1134 cm^{-1} (νC–N), 1387 cm^{-1} (νN=N), and 1434 cm^{-1} (νN=N) which increase in intensity over time [19]. At the same time, the signal related to the nitro group (1332 cm^{-1}) of 4-NTP decreases in intensity.

By plotting the signal intensity at 1142 cm^{-1}, associated with the presence of DMAB, versus time (fig. 4.6c in grey), it is possible to simulate the reaction kinetic mechanism with a bimolecular model which fits the experimental data well [20]:

$$I_P(t) = \sigma_P \frac{Kt}{1+Kt} \tag{27}$$

Where $I_P(t)$ is the Raman intensity of the signal at 1142 cm^{-1} related to DMAB, σ_P is the corrected Raman cross-section of the product (Raman intensity at infinite time), K is the kinetic constant and t is the reaction time.

In the same way, the signal intensity at 1332 cm^{-1}, associated with the 4-NTP, can be plotted versus time (fig. 4.6c in red):

$$I_R(t) = \sigma_R \frac{1}{1+Kt} \tag{28}$$

Where $I_R(t)$ is the Raman intensity of the signal at 1332 cm^{-1} related to 4-NTP, and σ_R is the corrected Raman cross section of the reactant. This reactant disappearance model also represents a bimolecular kinetics which fits the experimental data well. Moreover, the extrapolated reaction constants ($K = (3{,}17 \pm 0{,}91) \times 10^{-3}\ s^{-1}$, for DMAB production and $K = (3{,}03 \pm 0{,}13) \times 10^{-3}\ s^{-1}$, for 4-NTP consumption) well match with each other.

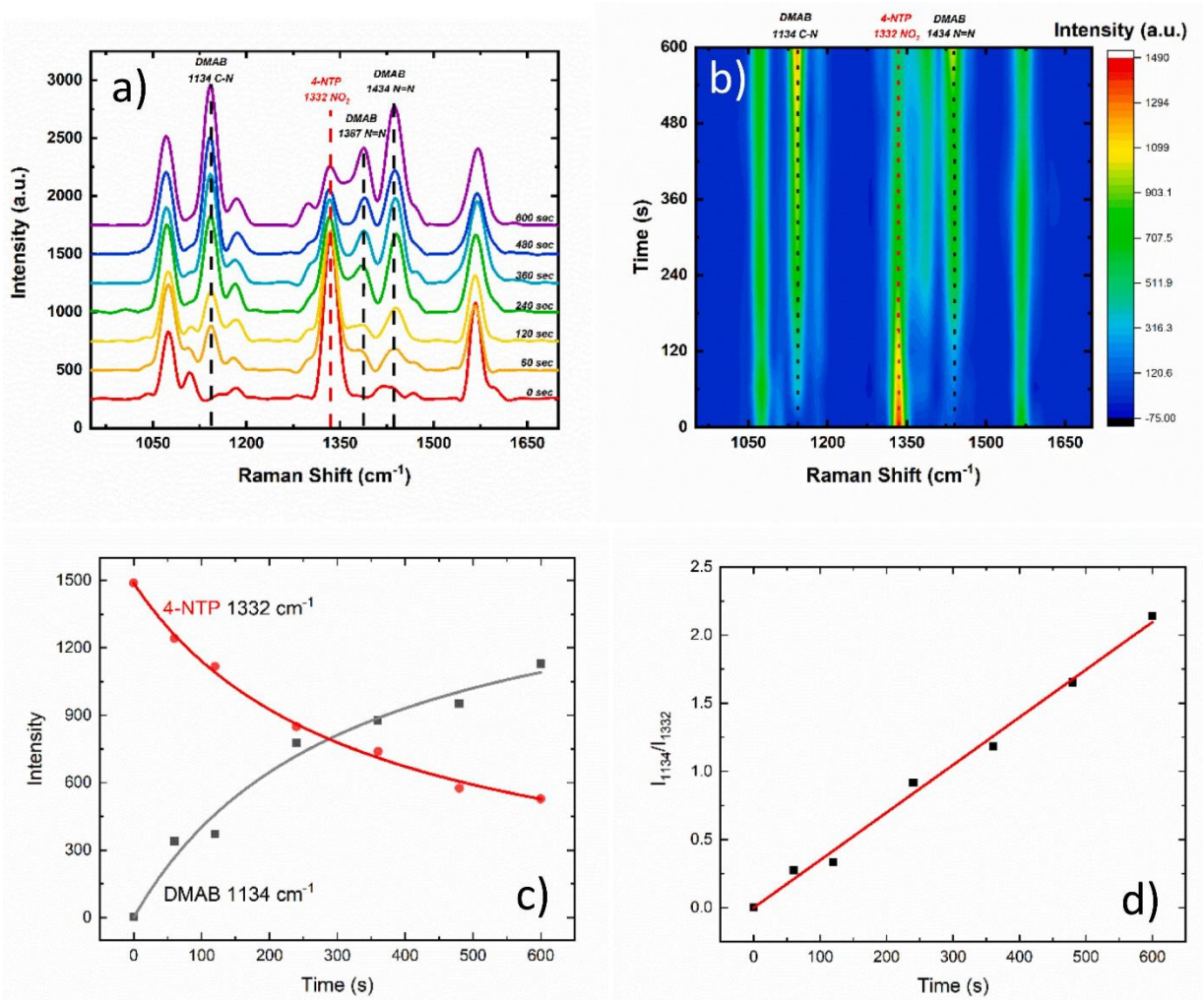

Figure 4.6. a) Temporal evolution of Raman spectra of 4-NTP on AgNFs obtained by laser excitation at 532 nm. b) Temporal map of Raman spectra. c) Plot and fitting of the experimental data relative to the Raman signal intensity of 4-NTP (in red) and DMAB (in grey). d) Plot and fitting of the experimental data relative to the Raman signal intensity ratio of the products and reactants [17].

Finally, it is possible to report the ratio between the last two equations (27) and (28) (fig. 4.6c) which represents the ratio between the intensities of the product and reactant signals as a function of time:

$$\frac{I_P(t)}{I_R(t)} = \frac{\sigma_P}{\sigma_R} Kt \qquad (29)$$

This is the equation of a linear function and it allows to evidence the degree of selectivity in the conversion of the reactants in the dimer. In case of deviation of the experimental data from the linear trend, the presence of reaction by-products should be considered. In our case, the experimental points fit the linear behaviour well, therefore the AgNFs are able to convert 4-NTP molecules into the DMAB dimer. This statement is also supported by the spectroscopic results as no chemical species other than 4-NTP and DMBA were detected. This result could be explained in terms of nanoroughness of AgNFs and thus by their high hotspot density on the nanoparticle surface. Because of this high density value, almost all the 4-NTP reactant molecules can be located on the tips and in the surface gaps, experiencing strong enhanced electric fields which drive the reaction toward the dimerization.

For AgNSs, the conversion of 4-NTP to DMAB is very low, as the extremely weak DMAB signals in the spectra reported in Figure 4.7a demonstrate. The wavelength mismatch between the position of the plasmon resonance and the 532 nm excitation [21], together with the particle morphology, limits the hotspot formation; the few hotspots are due to the presence of gaps between among close spherical nanoparticles. Therefore, the weak DMAB signals likely arise from a few nanosphere aggregates where dimerization occurs. Thus, only a small fraction of 4-NTP molecules reacts, without a full conversion of the reactant into the dimer.

Moreover, the bimolecular model of reactant consumption, previously applied to AgNFs, does not fit the experimental data well (fig. 4.7c, solid red line). However, by adding a constant representing the Raman intensity of the unreacted molecules (I_∞) to the equation (28), the following expression is obtained:

$$I_R(t) = \sigma_R \frac{1}{1+Kt} + I_\infty \qquad (30)$$

This equation fits very well with the experimental data for the consumption of 4-NTP over time (fig. 4.7c, red dashed line), confirming that many molecules do not react.

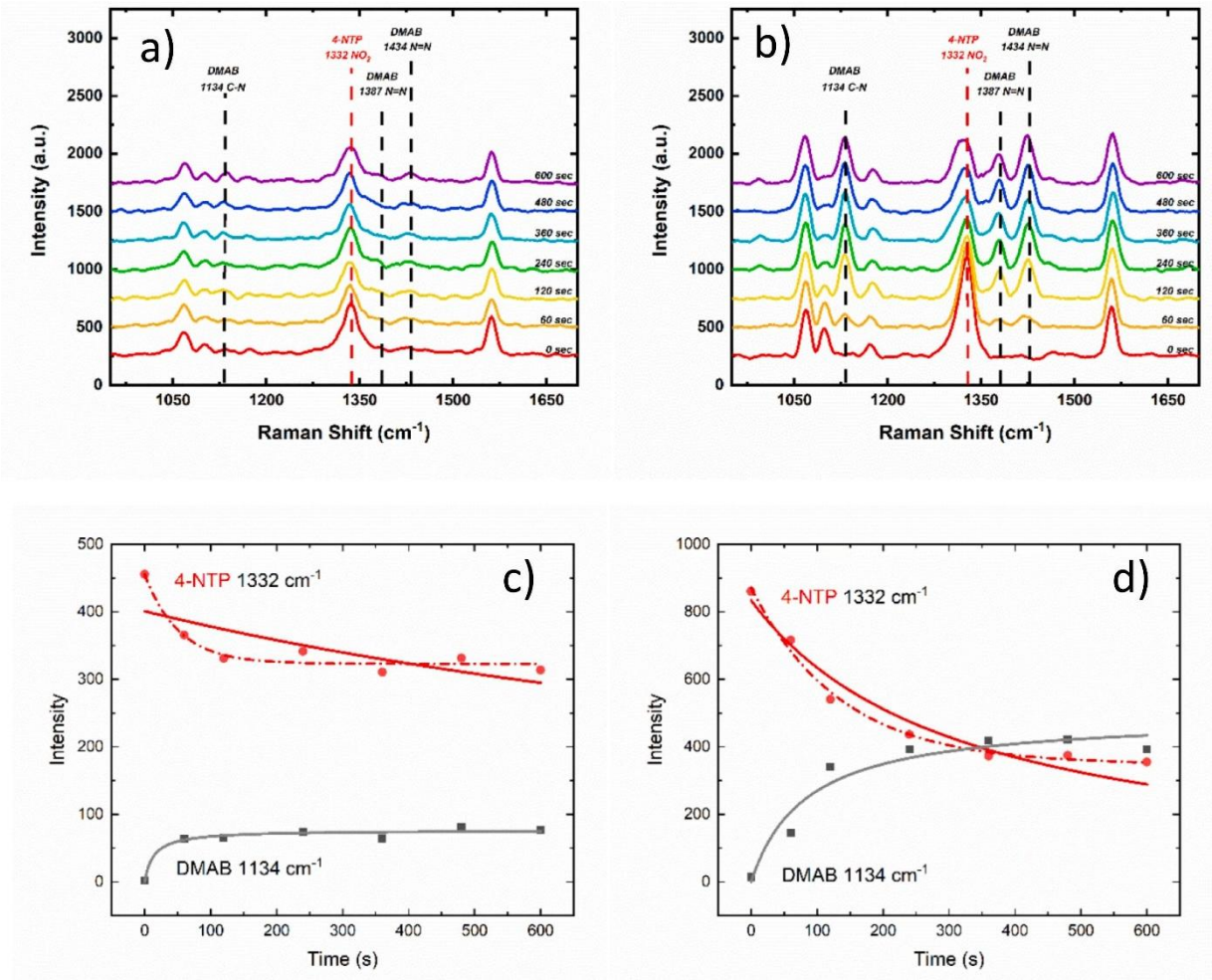

Figure 4.7. a) Temporal evolution of Raman spectra of 4-NTP on AgNSs and b) on AgNPTs obtained by laser excitation at 532 nm. c) Plot and fitting of experimental data relative to the Raman signal intensity of 4-NTP (in red) and DMAB (in grey) on AgNSs and d) on AgNPTs [17].

Thus, it was demonstrated that the morphology of the metallic particles strongly influence the reaction kinetics of the adsorbed molecules.

From experimental data, it was supposed that the field strength of individual hot-spot and their density on the particle surface can strongly influence the reaction kinetics. To rationalize in terms of the efficiency of electromagnetic enhancement, it was calculating the intensity of the electriv field on the surface of each nanostructure, by mean of finite-difference time-domain method

(FDTD) methods, which can solve the Maxwell equations and quantifying the variation, distribution, and intensity of electric field.

Local field enhancement calculations were obtained using the FDTD using Lumerical by ANSYS. The nanoparticles used in the simulation were modeled following the morphological data from Chapter 2 in terms of dimension, shape, and surface roughness. The wavelength used for near-field simulations was 532 nm. The adopted source type is Total field scattered-field.

Figure 4.8a show the electric field calculated for AgNSs with a diameter 20 nm. In detail, it was considered a system consisting of two contiguous nanospheres separated by a 1 nm gap, designed to model the characteristics of our substrate more accurately. The analysis revealed that the maximum field intensity is localized within the gap region between the surfaces of the two nanoparticles. However, the overall field intensification is relatively low. This explains why the reaction almost did not occur in the presence of AgNSs. Otherwise, when the shape of the nanostructure changed giving place to tips or roughness the intensity and distribution of the electric field drastically changed as in the case of the AgNPTs (figure 4.8c) and the AgNFs (figure 4.8b).

In this case, we modeled a triangular nanostructure with a side length of 120 nm. To account for the substrate's morphology, it was represented the system as two contiguous nanotriangles separated by a 1 nm gap between their tips. This configuration exhibited a pronounced enhancement of the local electromagnetic field, with the maximum intensity localized near the tips of the triangles, consistent with the well-known lightning rod effect. Notably, the highest field intensity was observed within the gap region between the tips of the two nanostructures. However, the field enhancement across the rest of the nanostructures surfaces is relatively low. As a result, only the molecules bound to the tips experience a very strong electric field, allowing them to react quickly. On the other hand, Figure 4.8b illustrates the near field of AgNFs (1 μm diameter), where, even if the field intensity is not as high as in the triangular nanostructures, the density of hot spots is much greater due to the high surface roughness. This allows almost all molecules to experience

a strong electric field, facilitating dimerization. These findings align with the earlier hypotheses: the small spherical nanoparticles show the lowest reaction efficiency, the AgNPTs show a fast reaction but only partial conversion of 4-NTP to DMAB, and the AgNFs, while having an average kinetic constant, catalyze complete dimerization of the molecules.

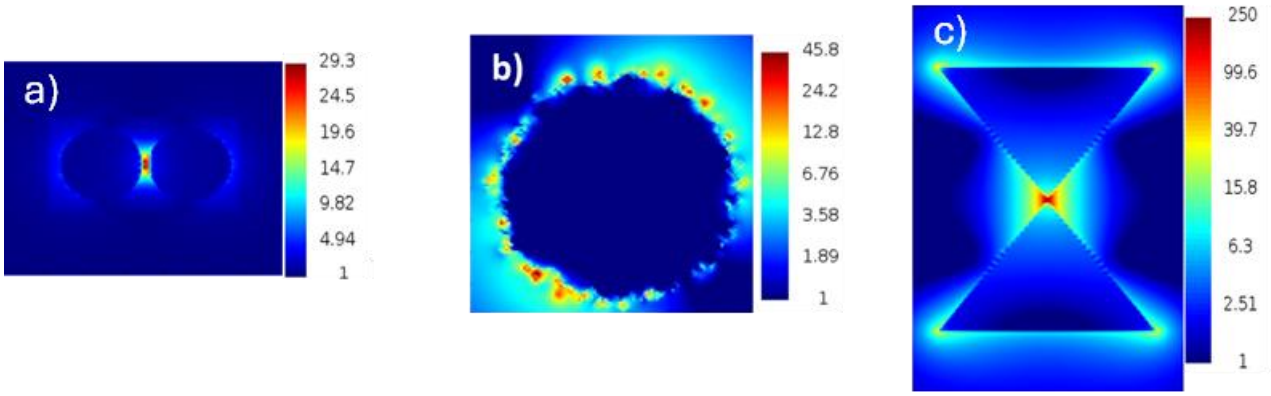

Figure 4.8. Local Field enhancement simulation for the three NPs studied, a) AgNSs b) AgNFs c) AgNTPs [17]. The electric field intensity is normalized.

Subsequently, experiments were performed using a 785 nm laser to investigate how the excitation wavelength could affect the reactivity of 4-NTP. In this case, the attention was on AgNFs that not only showed the best efficiency in 4-NTP conversion, but also possess a plasmon resonance covering the entire visible and near-infrared range, well matching the excitation wavelength.

In figure 4.9a and b the temporal evolution of Raman spectra of 4-NTP adsorbed on AgNFs and a zoom in the range 1550-1600 cm^{-1} over a time of 26 minutes are respectively shown. At the beginning, in a range of about 3-4 minutes, only the 4-NTP peaks were observed at 1075 cm^{-1} (νC–S), 1339 cm^{-1} ($\nu_s(NO_2)$), and 1569 cm^{-1} (νC–C). However, unlike the 532 nm experiment, the reaction displayed an unexpected evolution (fig. 4.9a). The nitro group signal decreased, suggesting an additional transformation of the molecule according to further reaction pathways which add to the only one previously observed using 532 nm laser. Anyway, the formation of DMAB was confirmed by the presence of its characteristic peaks. These ones were weak and

disappeared after five minutes, indicating further transformation. Moreover, the 1569 cm^{-1} peak, corresponding to the aromatic C–C stretch of 4-NTP, shifted to a new peak at 1587 cm^{-1} (fig. 4.9b), indicating the formation of aromatic molecules containing an amino group, i.e., 4-ATP [21].

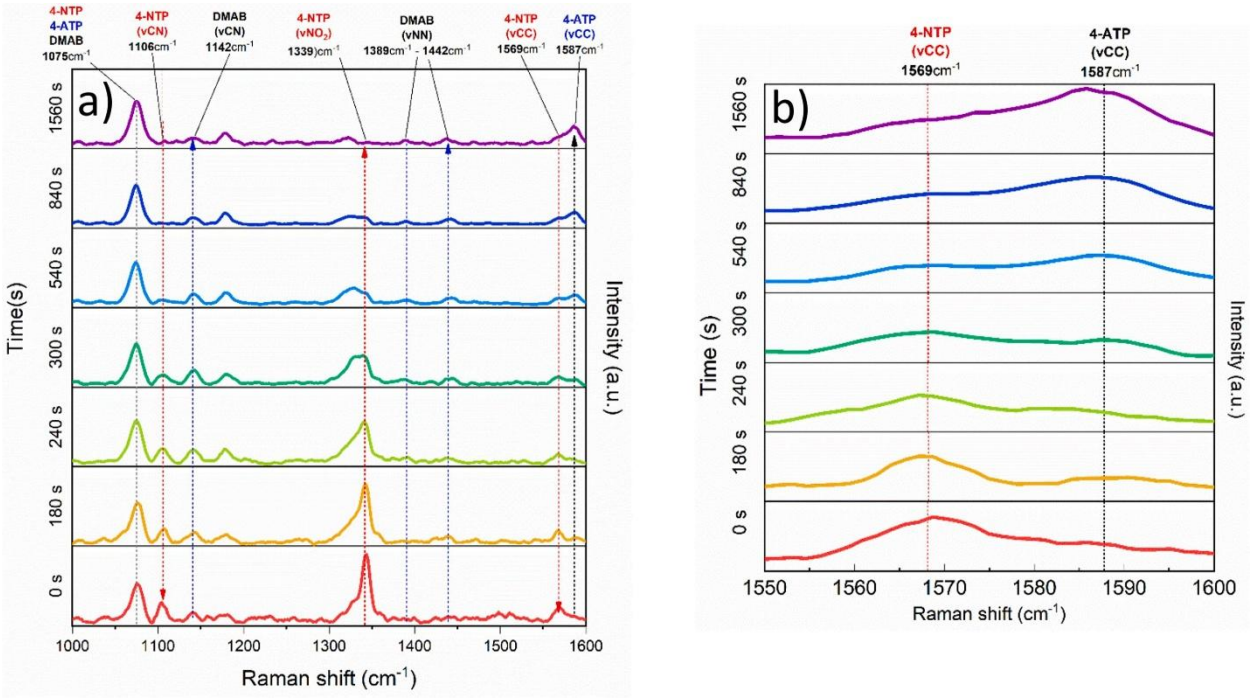

Figure 4.9. a) Temporal evolution of Raman spectra of 4-NTP on AgNFs obtained by laser excitation at 785 nm. b) Signals related to the vibration of the aromatic ring of 4-NTP and 4-ATP [17].

The formation of 4-ATP can be explained by considering two possible electron transfer pathways from a metal nanoparticle to an adsorbed molecule: indirect and direct [22]. Electrons must be excited from the metal Fermi level to the LUMO of the adsorbate to reach the energy gap (fig. 4.10a).

In the indirect pathway, electrons are excited via the LSPR and injected into the LUMO of the molecule (fig. 4.10c). This process is more effective at shorter wavelengths such as 532 nm, but it is limited by scattering losses.

The direct pathway involves electron excitation straight from the Fermi level to the LUMO of the adsorbate (fig. 4.10b) and is most efficient when the light energy closely matches the Fermi-

LUMO gap [22]. The Fermi-LUMO gap for DMAB is 1.85 eV. Instead, for 4-NTP activated molecule and 4-ATP, the gap is ~1.63 eV, closely matching the 785 nm photon energy (1.58 eV), promoting direct electron injection from silver to the 4-NTP LUMO and its conversion to 4-ATP. This is one of the mechanisms supported by the reaction pathway proposed by Zhao et al. [14].

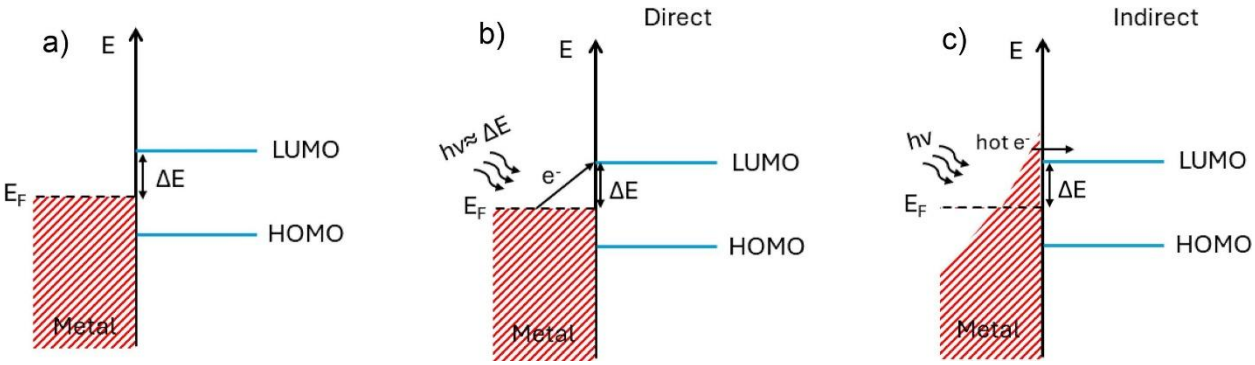

Figure 4.10. Schematic representation of the possible electron transfer mechanism from metal nanostructure to an adsorbed molecule: a) system before light interaction, b) direct electron transfer after light interaction, c) indirect electron transfer after light interaction [17].

Thus, the products of plasmon-driven reactions can be selectively controlled by adjusting the excitation wavelength. This strategy allows for precise tuning of the conversion of nitro groups into amines while adopting a greener and more sustainable approach. Moreover, the overall results suggest that a careful and targeted design of the plasmonic substrate could further enhance hot-carrier-driven processes, enabling the efficient transformation of environmental pollutants from various matrices into less harmful or even value-added compounds

References

[1] M. Hu, Z. Huang, R. Liu, N. Zhou, H. Tang, and G. Meng, 'SERS spectral evolution of azo-reactions mediated by plasmonic Au@Ag core–shell nanorods', *Nanoscale Adv*, vol. 4, no. 22, pp. 4730–4738, Nov. 2022, doi: 10.1039/D2NA00486K.

[2] C. H. Ho and S. Lee, 'SERS and DFT investigation of the adsorption behavior of 4-mercaptobenzoic acid on silver colloids', *Colloids Surf A Physicochem Eng Asp*, vol. 474, pp. 29–35, Jun. 2015, doi: 10.1016/J.COLSURFA.2015.03.004.

[3] H. Huh, H. D. Trinh, D. Lee, and S. Yoon, 'How Does a Plasmon-Induced Hot Charge Carrier Break a C-C Bond?', *ACS Appl Mater Interfaces*, vol. 11, no. 27, pp. 24715–24724, Jul. 2019, doi: 10.1021/ACSAMI.9B05509.

[4] 'Chemistry of Waste Minimization', *Chemistry of Waste Minimization*, 1995, doi: 10.1007/978-94-011-0623-8.

[5] M. Y. Zhao, Y. F. Tang, and G. Z. Han, 'Recent Advances in the Synthesis of Aromatic Azo Compounds', *Molecules 2023, Vol. 28, Page 6741*, vol. 28, no. 18, p. 6741, Sep. 2023, doi: 10.3390/MOLECULES28186741.

[6] B. Mondal and P. S. Mukherjee, 'Cage Encapsulated Gold Nanoparticles as Heterogeneous Photocatalyst for Facile and Selective Reduction of Nitroarenes to Azo Compounds', *J Am Chem Soc*, vol. 140, no. 39, pp. 12592–12601, Oct. 2018, doi: 10.1021/JACS.8B07767.

[7] J. Zhao, J. Wang, A. J. Brock, and H. Zhu, 'Plasmonic heterogeneous catalysis for organic transformations', *Journal of Photochemistry and Photobiology C: Photochemistry Reviews*, vol. 52, p. 100539, Sep. 2022, doi: 10.1016/J.JPHOTOCHEMREV.2022.100539.

[8] Y. Zhang *et al.*, 'Plasmon-Mediated CO2Photoreduction via Indirect Charge Transfer on Small Silver Nanoclusters', *Journal of Physical Chemistry C*, vol. 125, no. 48, pp. 26348–26353, Dec. 2021, doi: 10.1021/ACS.JPCC.1C07575.

[9] R. Schürmann, A. Dutta, K. Ebel, K. Tapio, A. R. Milosavljević, and I. Bald, 'Plasmonic reactivity of halogen thiophenols on gold nanoparticles studied by SERS and XPS', *Journal of Chemical Physics*, vol. 157, no. 8, p. 84708, Aug. 2022, doi: 10.1063/5.0098110/2841944.

[10] Z. Zhang *et al.*, 'Enhancement of the low-temperature catalytic graphitization of polyacrylonitrile by incorporating Cu nanostructures as plasmonic photocatalyst', *J Mater Sci*, vol. 57, no. 3, pp. 1703–1713, Jan. 2022, doi: 10.1007/S10853-021-06742-Z.

[11] F. Kameche *et al.*, 'Plasmon-triggered living photopolymerization for elaboration of hybrid polymer/metal nanoparticles', *Materials Today*, vol. 40, pp. 38–47, Nov. 2020, doi: 10.1016/J.MATTOD.2020.03.023.

[12] L. Yuan *et al.*, 'Morphology-Dependent Reactivity of a Plasmonic Photocatalyst', *ACS Nano*, vol. 14, no. 9, pp. 12054–12063, Sep. 2020, doi: 10.1021/ACSNANO.0C05383.

[13] Z. Li and D. Kurouski, 'Elucidation of Photocatalytic Properties of Gold-Platinum Bimetallic Nanoplates Using Tip-Enhanced Raman Spectroscopy', *Journal of Physical Chemistry C*, vol. 124, no. 23, pp. 12850–12854, Jun. 2020, doi: 10.1021/ACS.JPCC.0C04274.

[14] L. Bin Zhao, J. L. Chen, M. Zhang, D. Y. Wu, and Z. Q. Tian, 'Theoretical study on electroreduction of p-nitrothiophenol on silver and gold electrode surfaces', *Journal of Physical Chemistry C*, vol. 119, no. 9, pp. 4949–4958, Mar. 2015, doi: 10.1021/JP512957C.

[15] G. Zheng, L. Polavarapu, L. M. Liz-Marzán, I. Pastoriza-Santos, and J. Pérez-Juste, 'Gold nanoparticle-loaded filter paper: a recyclable dip-catalyst for real-time reaction monitoring by

surface enhanced Raman scattering', *Chemical Communications*, vol. 51, no. 22, pp. 4572–4575, Mar. 2015, doi: 10.1039/C4CC09466B.

[16] W. Xie and S. Schlücker, 'Hot electron-induced reduction of small molecules on photorecycling metal surfaces', *Nature Communications 2015 6:1*, vol. 6, no. 1, pp. 1–6, Jul. 2015, doi: 10.1038/ncomms8570.

[17] M. Condorelli *et al.*, 'Tuning plasmonic reactivity: Influence of nanostructure, and wavelength on the dimerization of 4-NTP', *J Catal*, vol. 450, p. 116267, Oct. 2025, doi: 10.1016/J.JCAT.2025.116267.

[18] Q. Ding, H. Zhou, H. Zhang, Y. Zhang, G. Wang, and H. Zhao, '3D Fe3O4@Au@Ag nanoflowers assembled magnetoplasmonic chains for in situ SERS monitoring of plasmon-assisted catalytic reactions', *J Mater Chem A Mater*, vol. 4, no. 22, pp. 8866–8874, May 2016, doi: 10.1039/C6TA02264B.

[19] Y. Liu *et al.*, 'A study of plasmon-driven catalytic 4-NBT to DMAB in the dry film by using spatial Raman mapping spectroscopy', *Nano Res*, vol. 15, no. 7, pp. 6062–6066, Jul. 2022, doi: 10.1007/S12274-022-4310-X.

[20] W. Koopman, R. M. Sarhan, F. Stete, C. N. Z. Schmitt, and M. Bargheer, 'Decoding the kinetic limitations of plasmon catalysis: the case of 4-nitrothiophenol dimerization', *Nanoscale*, vol. 12, no. 48, pp. 24411–24418, Dec. 2020, doi: 10.1039/D0NR06039A.

[21] A. Bhattarai, I. V. Novikova, and P. Z. El-Khoury, 'Tip-Enhanced Raman Nanographs of Plasmonic Silver Nanoparticles', *Journal of Physical Chemistry C*, vol. 123, no. 45, pp. 27765–27769, Nov. 2019, doi: 10.1021/ACS.JPCC.9B07811.

[22] H. Tang *et al.*, 'Plasmonic hot electrons for sensing, photodetection, and solar energy applications: A perspective', *Journal of Chemical Physics*, vol. 152, no. 22, Jun. 2020, doi: 10.1063/5.0005334/1061964.

Chapter 5

5.1 Challenges towards quantitative SERS

As reported until now, SERS is a very useful technique thanks to its versatility, specificity, and above all its very high sensitivity. From a qualitative point of view, SERS has all the features to be adopted as analytical method in many application fields. However, its application remains limited due to challenges in quantitative reliability [1], [2].

SERS can give accurate information about the chemical composition of a sample, even when for complex samples, thanks to the development of data analysis based on multivariate methods [2]. In addition, SERS can detect analytes at very low concentrations, even to a single molecule. These strong advantages have encouraged the development of more and more efficient and enhancing substrates, but the high sensitivity of SERS substrates is often associated with low repeatability and reproducibility, which makes quantitative measurements and real applications difficult [3], [4].

Methods to improve quantitative performance include measurement protocols such as building a calibration curve of SERS intensity versus analyte concentration and determining the limit of detection (LOD) and the limit of quantification (LOQ) [2], [4]. The calibration curve can ideally provide a linear range, from which an equation can be obtained to link Raman intensity with analyte concentration. Typically, SERS calibration curves have a sigmoidal shape (fig. 5.1a) [5]. The first part of the curve helps determine the LOD and LOQ, where the analyte signal is indistinguishable from the noise. The central part gives the linear interval needed for quantification. In the final part, signal intensity reaches a plateau because, as the analyte concentration increases, the SERS substrate surface becomes saturated and further adsorption is blocked.

However, using only the calibration curve for quantitative analysis is not enough. Measurement variance can be very high, depending both on the instrument and on the SERS substrate itself. For example, the laser power may decrease over time or the plasmonic particles on the substrate may have different levels of aggregation, producing very different signal intensities at the same analyte concentration. For this reason, internal standards are often used [1], [2]. The internal standard must give a signal clearly different to the analyte (fig. 5.1b). When constructing the calibration curve, the intensity ratio between analyte and standard signals is used as a function of analyte concentration. During the analysis the concentration of the standard must remain constant. In this way, if the laser power changes, both signals are affected equally, and the ratio cancels out this effect.

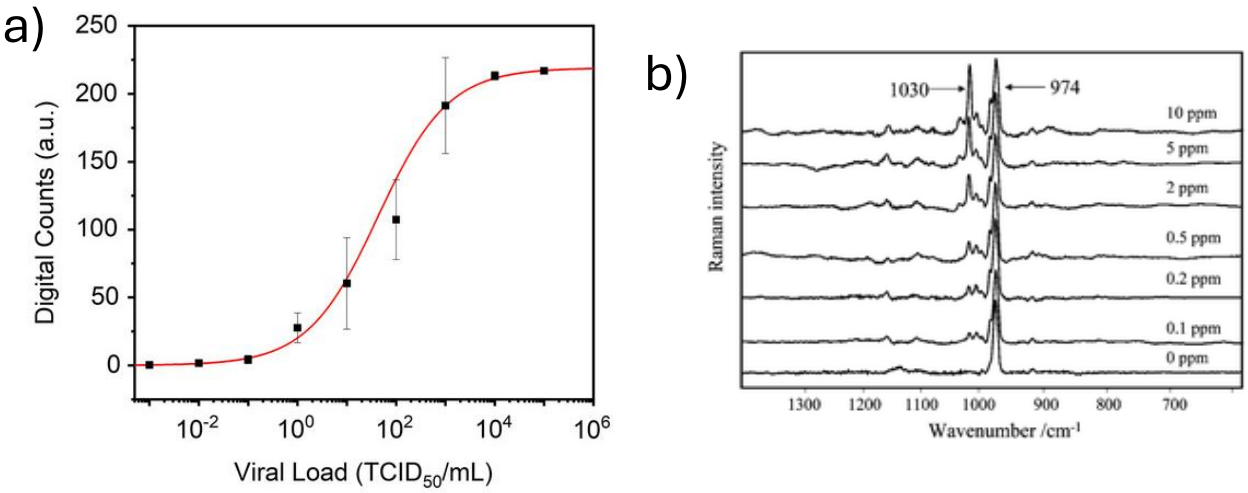

Figure 5.1. a) Calibration curve for SERS quantification of SARS-CoV-2N protein viral load [5]. b) SERS spectra of nicotine (1030 cm^{-1}) at various concentrations with an internal standard (974 cm^{-1}) [6].

However, even internal standards may not be enough. The standard can compete with the analyte for adsorption on the substrate surface. As a result, it may saturate the surface unevenly, occupying the hot-spot sites that became forbidden for analyte adsorption [7]. This can reduce the concentration range measurable or make the analyte-standard ratio non-linear [8]. To solve this problem, an interesting method has been developed [9]: plasmonic particles are synthesized so that

the internal standard is adsorbed first, then the particles are covered with another plasmonic layer, forming a core–shell structure where the standard molecules are trapped inside. The external surface remains free for analyte adsorption, without interference.

Despite these strategies, one of the main problems of quantitative SERS still remains: the substrate stability. For example, in plasmonic nanoparticle colloids, particles are in suspension because of the electrostatic repulsion; each nanoparticle has a surface charge given by capping molecules. To increase sensitivity one strategy could be to bring the nanoparticles closer together, the aggregation can be induced by adding salt which screens the charges and at the same time creates more hot-spots, thus stronger SERS signals. However, aggregation is hard to control: at first it increases signals, but later large aggregates form, sink, and cause a strong decrease in SERS intensity [10]. In addition metal nanoparticles when dispersed in water are susceptible of oxidation which can lead to a change in the nanoparticle's properties.

About this, silver colloids for SERS employ have the best plasmonic and enhancing properties, but they are unstable over time. In fact, oxidation changes particle surfaces, strongly affecting SERS signals, since the oxide layer reduces plasmonic properties and electromagnetic enhancement [11]. For example, silver oxidation and carbon contamination happen just by exposing substrates to air, and signals can drop by up to 60% within a few hours (fig. 5.2) [12]. Oxidation also reduces analyte adsorption and charge transfer between metal and analyte, lowering chemical enhancement and sensitivity [13].

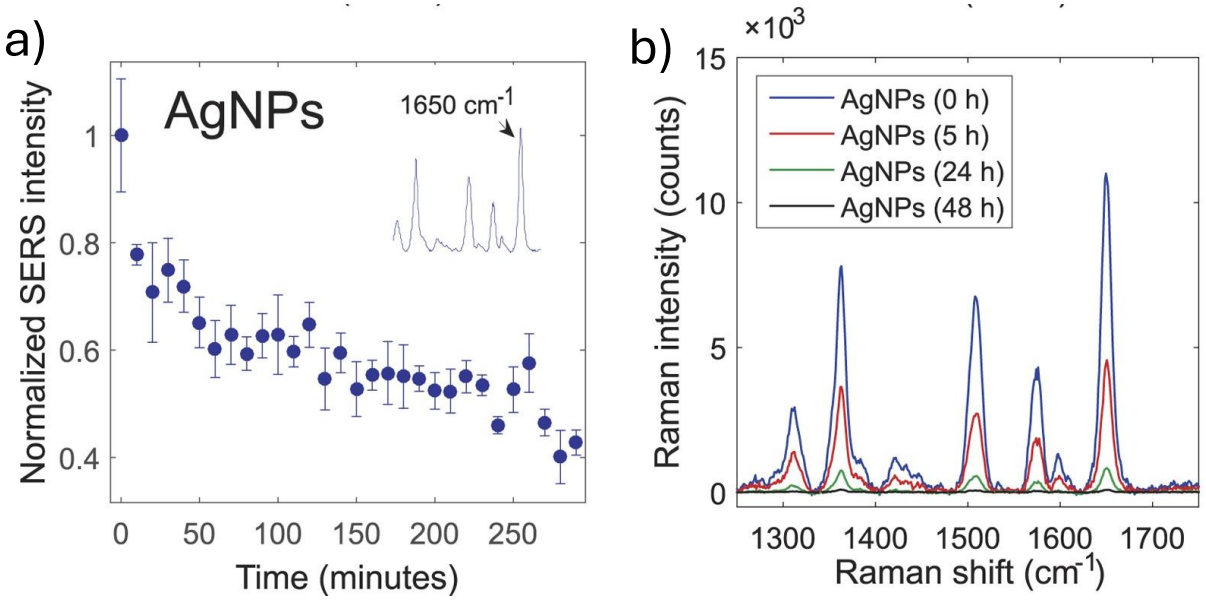

Figure 5.2. a) Normalized Raman intensity of Rhodamine6G and b) Raman spectra decrease over the time on silver nanoparticles [12].

Another important factor is the interaction between the substrate and the laser during SERS measurements. Hot electrons can decay non-radiatively, releasing energy as heat through electron–phonon and phonon–phonon scattering [14]. This photoheating can change analyte adsorption over time. For example, benzenthiol has been observed to desorb from the substrate, with up to 90% signal loss in only 25 minutes (fig. 5.3a) [15]. Laser interaction can even modify substrate morphology: strong heating can cause evaporation and fragmentation of nanoparticles (fig. 5.3b) [16].

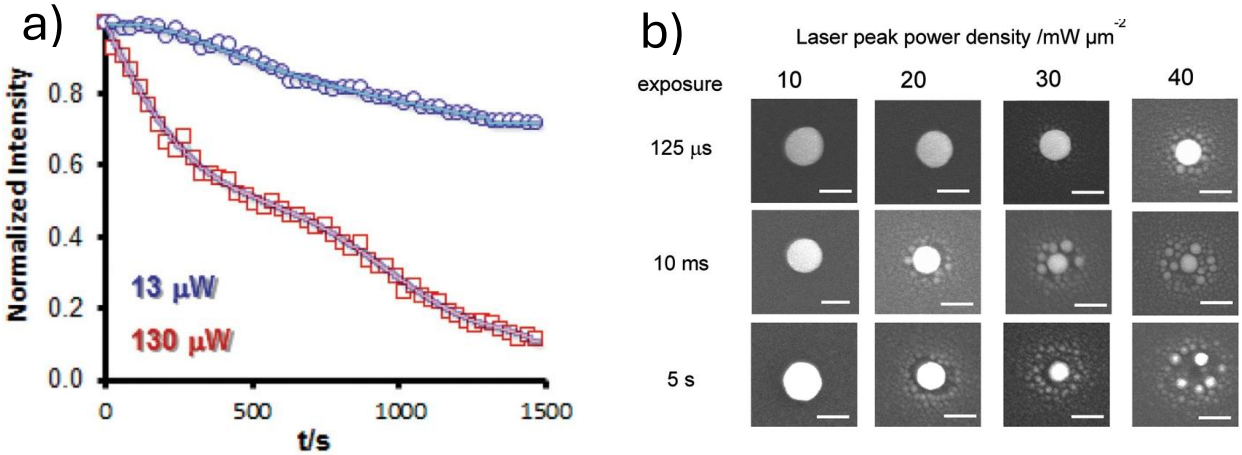

Figure 5.3. a) Normalized Raman Intensity of benzenthiol decrease over the time [15]. b) Gold nanoparticles reshaping and fragmentation after laser exposure [16].

A possible solution is to coat silver or gold nanoparticles with a material resistant to laser effects. Platinum, for example, shows high resistance and stability under laser irradiation [17].

This chapter presents a mechanistic study of the synthesis of Silver/Platinum Nanoplates (Ag/Pt NPTs), aiming to improve SERS substrate stability.

Platinum was chemically deposited onto colloidal silver nanoplates, under controlled conditions such as pH, reducing agent concentration and other. The resulting nanoplates showed a significantly better stability and measurement repeatability. Although higher platinum coverage reduced SERS intensity, due to platinum lower plasmonic activity compared to silver [18], the coating effectively protected silver from photothermal effects induced by the laser. Systematic adjustment of synthesis conditions made it possible to link coating characteristics to SERS performance. The balance between signal intensity and substrate stability shows the potential of Ag/Pt NPTs as reliable platforms for SERS applications.

5.2 Synthesis of Silver Nanoplates covered with Platinum

Bimetallic nanoparticles are materials made of two metallic elements such as gold, silver, platinum, palladium, etc., and they offer unique properties by combining synergically the behaviours of each individual metal. Different types of metallic nanoparticles can be obtained depending on the synthesis method used. Considering only wet chemical methods, three main types of synthesis can be carried out [19].

First of all, two metal precursors are needed. For example, synthesizing a bimetallic particle of silver and copper, is necessary to start from their water-soluble salts (such as silver nitrate and

copper acetate), which provide Ag^{+} and Cu^{2+} ions. These metal ions are then reduced by suitable reducing agents.

The first type of synthesis is the co-reduction of the two metal species at the same time. In this case, a solution containing both salts is prepared, and the reducing agent is added. The result is the formation of alloy nanoparticles (Fig. 5.4a), which are a solid mixture of the two elements [20].

The second type of synthesis involves the reduction of the two metal precursors at different times. First, monometallic nanoparticles are synthesized. Afterwards, the second metal precursor is introduced into the solution and reduced on the surface of the preformed nanoparticles, leading to core-shell structures [21]. This method is called seeded-growth (Fig. 5.4b).

A third type of synthesis derives from the seeded-growth method. Synthesizing a core-shell particle of silver coated with gold, first, silver nanoparticles are prepared, and then gold is reduced on their surface. However, gold is a more noble metal than silver, so redox chemistry rules that Au^{3+} ions will be reduced onto the silver surface, while metallic silver will be oxidized and dissolved in solution as Ag^{+} ions. This process is called anodic dissolution or galvanic replacement, and the result is the formation of hollow nanoparticles [22] with a gold shell and residual silver (Fig. 5.4c).

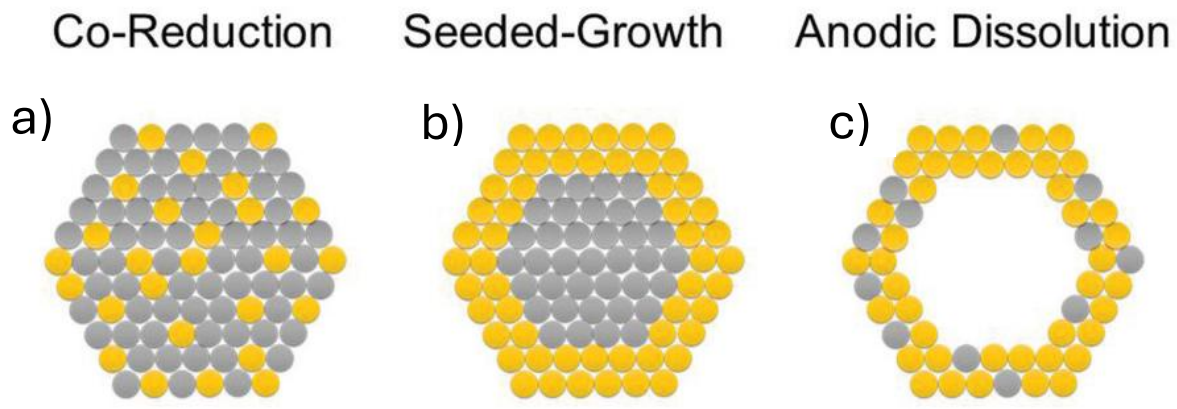

Figure 5.4. Bimetallic nanoparticles: a) nanoalloy obtained by co-reduction, b) core–shell obtained by seeded-growth, c) hollow structure obtained by anodic dissolution [19].

Bimetallic nanoparticles are mainly used in the biomedical field and in heterogeneous catalysis [23], [24]. For example, it is well known that silver is cytotoxic in biological environments because it releases Ag^+ ions, which generate reactive oxygen species. Therefore, regulating cytotoxicity can be useful, and Ting Li et al. observed that bimetallic nanoparticles of gold and silver can be effective depending on their composition [25].

In the field of catalysis, many processes employ catalytic species such as platinum or palladium, but several studies have shown that the addition of a second metallic component can improve catalytic performance and increase catalyst stability. This effect is due to the creation of new active sites and new electronic states which regulate the binding energy with reaction intermediates more effectively than in monometallic particles [24].

Bimetallic nanoparticles are also reported in SERS studies. For instance, Jie Yang et al. showed that silver nanoplates coated with palladium can provide better catalytic performance in the conversion of 4-NTP to 4-ATP in the presence of $NaBH_4$ [26].

Silver/Platinum bimetallic nanoparticles are interesting because they combine the strong plasmonic properties of silver with the unique catalytic abilities of platinum [27]. The presence of platinum allows an easy tuning of the silver LSPR band towards the near-infrared region [28], [29]. Moreover, the difference in electronegativity between the two metals causes an electron transfer from silver to platinum, which modifies their electrocatalytic performance for water splitting [30].

The synthesis of silver nanoparticles coated with platinum has been studied in several reports, and it was observed that the control of reaction parameters is essential to obtain the desired products [31], [32], [33], [34]. Each variable, such as pH, the platinum precursor, the reducing agent, the concentrations, can drastically change the elemental composition and morphology of the bimetallic particles.

The synthesis of Silver/Platinum Nanoplates was carried out using the "seeded-growth" approach, mainly controlling the reaction pH and the concentration of the reducing agent, following the scheme shown in Figure 5.5. First, silver nanoplates (AgNPTs) were synthesized as described in Chapter 2. Then, a 200 µl aliquot of the AgNPT colloid was added to 3 ml of an aqueous solution of polyvinylpyrrolidone (PVP) at a concentration of 4 mg/ml. To this solution, a variable volume (from 50 µl to 250 µl) of 0.01 M ascorbic acid (AA) was added. The reaction pH was controlled by adding NaOH. Afterwards, 50 µl of the platinum precursor, 0.01 M hexachloroplatinic acid (H_2PtCl_6), was introduced. It should be noted that the reaction pH was set between 6 and 10, considering the pH change due to the addition of the platinum precursor. After one hour, the obtained particles were washed with MilliQ water through cycles of centrifugation and redispersion, and finally collected in 400 µl of MilliQ water.

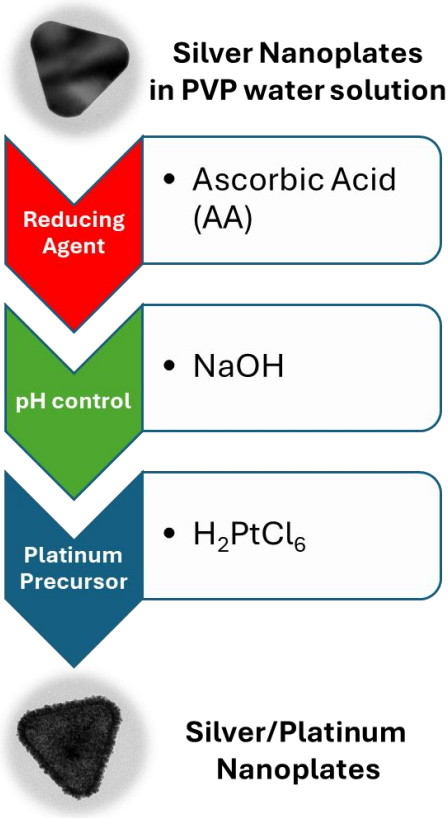

Figure 5.5. Synthesis scheme of Silver/Platinum Nanoplates.

Each sample of bimetallic particles obtained was named Ag/Pt NPTs followed by the amount of ascorbic acid and the pH value used. In particular, the amount of ascorbic acid refers to the molar ratio with the platinum precursor. If an equimolar amount of AA and H_2PtCl_6 was used, it is indicated as AAx1. If the molar amount of ascorbic acid was five times higher than platinum, it is indicated as AAx5. Thus, the label "Ag/Pt NPTs AAx3 pH8" refers to a sample of silver/platinum nanoplates synthesized with a reducing agent three times higher in molar ratio than the platinum precursor, at pH 8.

The obtained nanoparticles were deposited on copper grids for morphological characterization by transmission electron microscopy (TEM), using a Zeiss 900 N TEM operating at 80 kV. The elemental distribution was monitored by scanning TEM and energy-dispersive X-ray spectroscopy (EDS) measurements, performed with a Jeol JEM2100 F at an acceleration voltage of 200 kV. To determine the elemental speciation, the nanoparticles were deposited on silicon wafers and XPS spectra were acquired with a Thermo Fisher ESCALAB 250Xi, using monochromatic Al Kα radiation and argon-assisted charge compensation. All spectra were averaged over 10 scans and measured with a pass energy of 10 eV, a step size of 0.05 eV, and a dwell time of 100 ms.

Figure 5.6 reports the characterizations of the silver nanoplates that were dispersed in PVP solution before the addition of any reagents, and therefore without platinum coating. Before the characterizations, the AgNPTs were washed to remove the excess PVP. TEM images (Fig. 5.6a and 5.6b) show silver particles with mainly triangular and hexagonal morphology, with triangle's side-tip distances of about 150 nm. This size justifies the position of the plasmon resonance signal in the UV–Vis–NIR extinction spectrum (Fig. 5.6c), which is found in the near-infrared region at about 950 nm, corresponding to the in-plane dipolar mode [35]. The XPS spectrum (Fig. 5.6d) shows the two typical signals of the silver 3d orbitals [36], separated by 6 eV due to spin-orbit coupling, with binding energies centered at 368.04 eV and 374.04 eV and a full width at half maximum (FWHM) of 0.55 eV. These results confirm that the silver forming the nanoplates is in

the metallic state with no residual oxidation. The protection against oxidation is due to the presence of the capping agent PVP, which protects the metallic surface from oxidation.

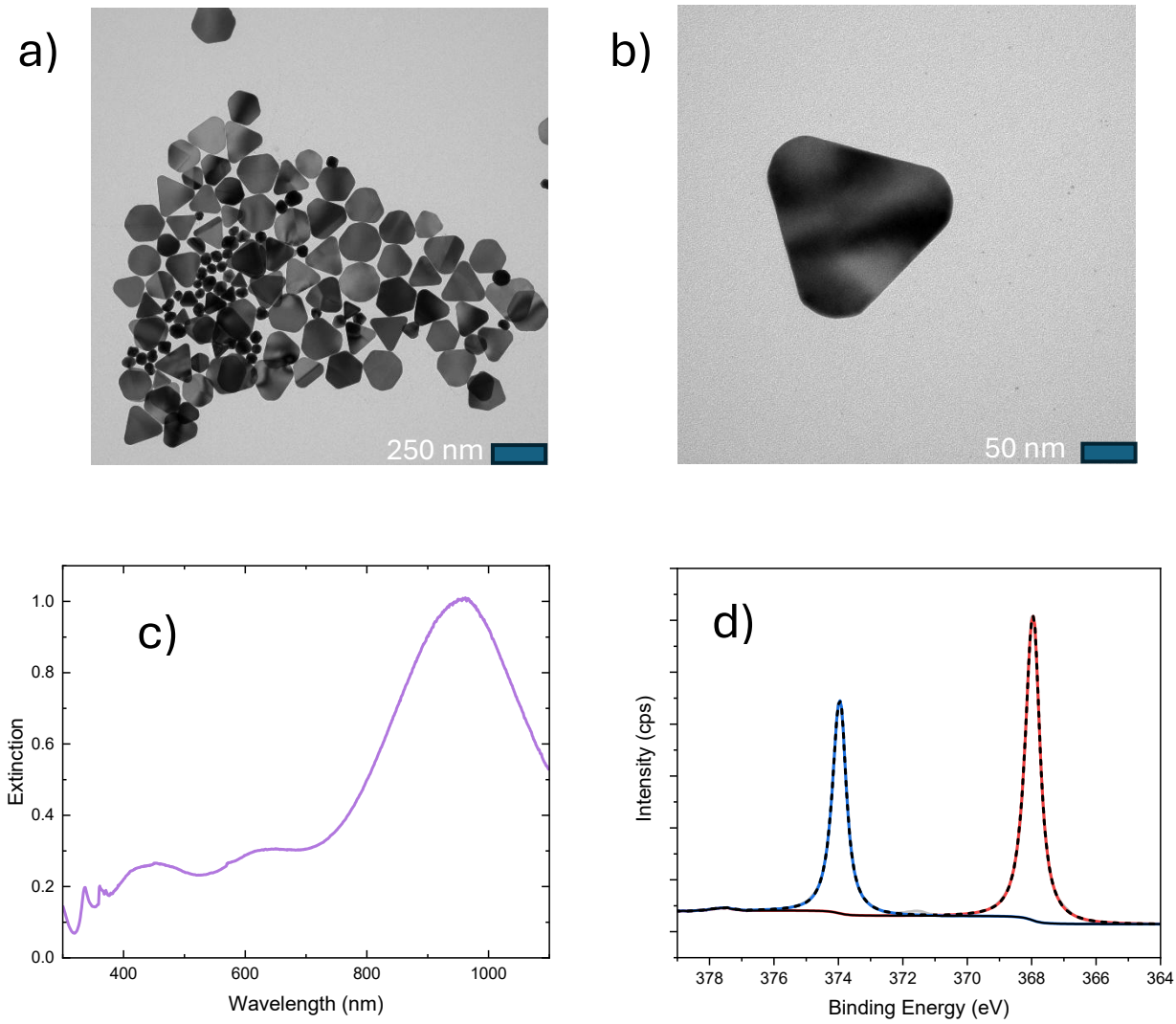

Figure 5.6. a) TEM image of AgNPTs and b) TEM image at higher magnification. c) Extinction spectrum of AgNPTs aqueous colloid. d) XPS spectrum of AgNPTs deposited onto a silicon wafer.

The chemical growth of platinum on silver nanoplates involves galvanic replacement processes which lead to the corrosion of the silver particle, since platinum is a more noble metal than silver and therefore tends to be reduced by oxidizing silver [32]. As previously discussed, the anodic dissolution process initially promotes the formation of hollow platinum particles, since corrosion

progressively perforates and etches the silver template. If this process occurs without control, it proceeds rapidly and aggressively, ultimately resulting in the complete destruction of the particle. Conversely, when corrosion is carefully moderated, the final result is a stable hollow platinum particle which remains intact even during the later stages of the reaction and for this reason the stability of silver nanoplates requires passivation of the surface with PVP [31].

Previous studies have reported experimental results on galvanic replacement processes of platinum on silver nanoplates [37], [38], with the aim of creating extended platinum platforms that are often not achievable without the use of a sacrificial template. In contrast, the objective of this work is to obtain bimetallic nanoparticles limiting the consumption of silver because is the plasmonic active material necessary for SERS application while the platinum role is to cover the silver to reduce the oxidation processes and laser damage.

To limit the anodic dissolution of the silver template, some reports have shown that it is necessary to use a reducing agent capable to reduce the metal ion more rapidly. For example, the same synthesis strategy has been applied to coat silver nanocubes with gold [39] and with platinum [40] by introducing ascorbic acid as the reducing agent into the reaction environment controlling the reduction rate of the metal precursors and limiting the corrosion of the silver template.

Moreover, ascorbic acid contains two acidic protons, and it has been shown that its reducing strength depends on the degree of protonation [41]. In particular, the reducing power increases at higher pH values, thus, the fully deprotonated form is the most reducing, followed by the mono-deprotonated form, and finally the non-deprotonated form.

Kumar-Krishnan et al. investigated the synthesis of bimetallic nanoplates with a silver core and a shell of gold, platinum, or palladium, as a function of the reaction pH by modulating the reducing power of ascorbic acid [42]. They reported results for pH values of 4 and 11 using a platinum(II) precursor and observed that at pH 4, hollow triangular particles are formed due to the corrosion of the metal precursors, whereas at pH 11, the reducing power of ascorbic acid prevents galvanic

replacement, resulting in rough core–shell structures. Considering that the pK_1 and pK_2 values of ascorbic acid are approximately 4.2 and 11.5 [43], respectively, more than 50% of ascorbic acid was non-deprotonated in the acidic experiments, whereas for the syntheses carried out under basic conditions, most of the ascorbic acid was monodeprotonated with a fraction fully deprotonated.

In contrast to the synthesis reported by Kumar-Krishnan et al., in this work a platinum(IV) precursor is employed, which completely changes the outcome of the synthesis, as will be shown. At the same time, the reaction pH is set between 6 and 10 so that all the ascorbic acid is in its monodeprotonated form. With this precaution, the pH does not affect the reducing power of ascorbic acid, allowing the focus to shift to other phenomena that rule on the deposition of platinum onto silver.

Based on the effect of pH, the first synthesis experiments of Ag/Pt NPTs were carried out keeping the concentration of AA constant at a molar ratio three times higher than the platinum precursor. TEM images of the samples Ag/Pt NPTs AAx3 pH10, Ag/Pt NPTs AAx3 pH8, and Ag/Pt NPTs AAx3 pH6 are shown in Figures 5.7a, 5.7b, and 5.7c, respectively. The images reveal completely different morphologies, suggesting that pH plays a key role in the reduction of platinum regardless of the intrinsic reducing power of AA.

The particles synthesized at pH 10 (Fig. 5.7a) are the most similar to the original silver nanoplates, showing a smooth surface with slight corrosion localized at the particle edges. In contrast, the synthesis at pH 8 (Fig. 5.7b) shows a slight roughness attributed to deposited platinum nanoparticles and “perforated” areas, suggesting partial anodic dissolution of silver. Finally, the sample at pH 6 (Fig. 5.7c) exhibits pronounced and uniform roughness over the entire particle, as platinum finds favourable deposition conditions. The high roughness indicates an island-growth process typical of galvanic replacement; however, this cannot be the only mechanism of platinum reduction, since the nanoplates are intact thanks to the combined protective effect of PVP and the reduction of the AA.

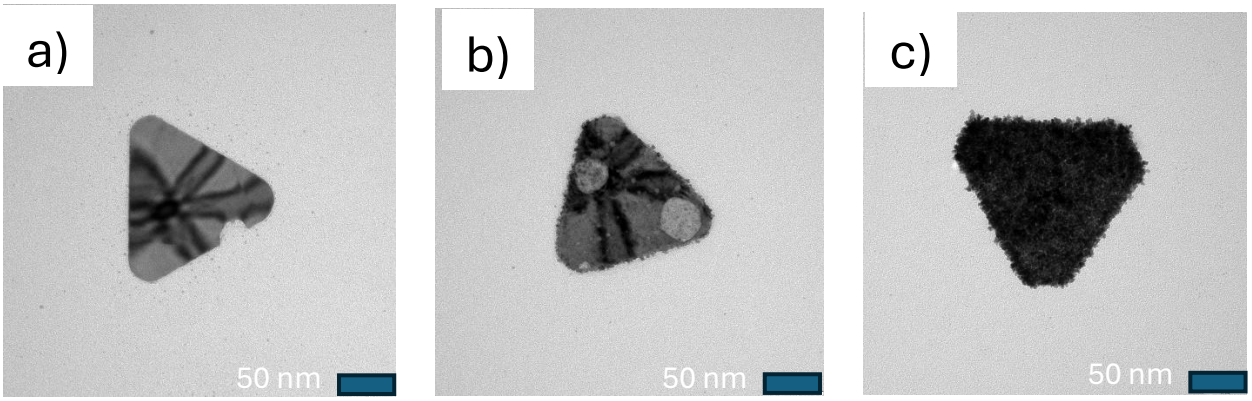

Figure 5.7. TEM images of samples a) Ag/Pt NPTs AAx3 pH10, b) Ag/Pt NPTs AAx3 pH8 and c) Ag/Pt NPTs AAx3 pH6.

Figure 5.8 shows the STEM images of the three samples together with the EDS maps of silver (in green) and platinum (in blue), used to monitor the elemental distribution of the two species in the synthesized particles. It can be observed that platinum is uniformly distributed over the entire surface of the nanoplates for all the pH values used, but the amount deposited increases at lower pH, as indicated by the higher intensity of the colour in the maps. This observation is consistent with the morphological analysis, which showed that at more acidic pH the particles are rougher and therefore contain larger platinum nanoparticles compared to those obtained at higher pH. Furthermore, at pH 8, the amount of silver is lower precisely in the areas where TEM images indicated voids, confirming that these regions were eroded by anodic dissolution.

The reason why platinum tends to deposit more slowly under basic pH conditions is probably related to the concentration of OH^- ions, which act as stronger ligands for Pt^{4+} species compared to chloride ions or water molecules. Indeed, Dabbish et al. reported that the reduction of platinum(IV) complexes by AA is strongly influenced by the type of ligand bound to platinum, and OH^- ions make the complexes more inert [44]. This hypothesis was also proposed in the study by Aslam et al., who synthesized silver core-shell nanocubes coated with a thin layer of platinum

at pH 12 [34], stating ligand exchange modifies the electronic levels of the platinum complex, lowering its reduction potential.

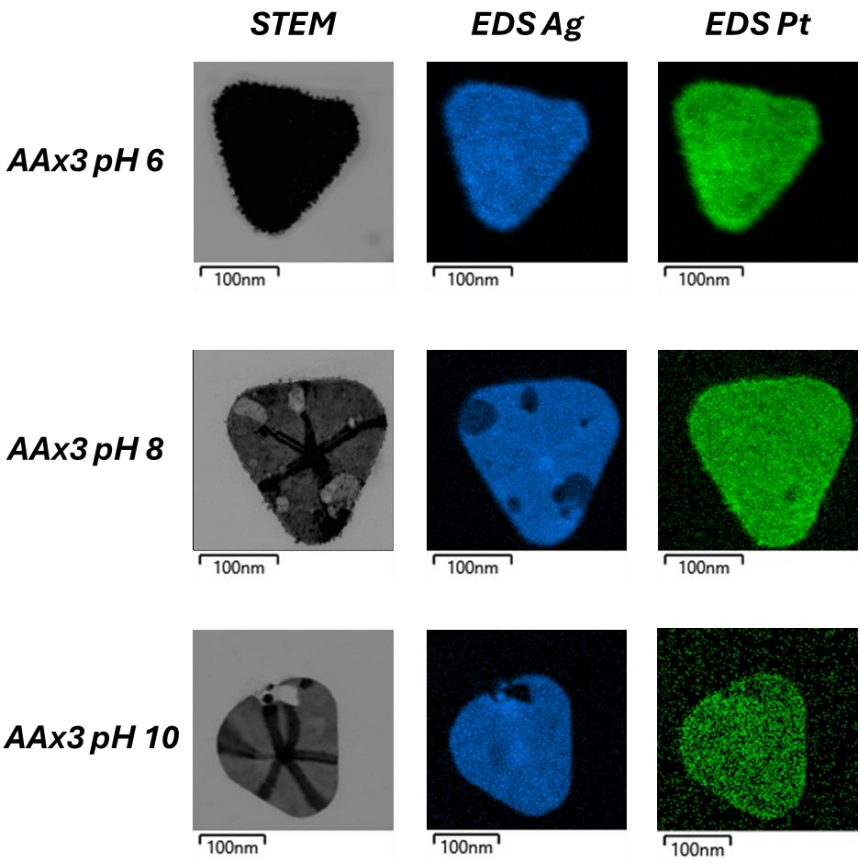

Figure 5.8. STEM images and EDS elemental distribution of Ag (in blue) and of Pt (in green) for the samples Ag/Pt NPTs AAx3 pH6, Ag/Pt NPTs AAx3 pH8 and Ag/Pt NPTs AAx3 pH10.

The chemical speciation of silver and platinum was analysed for the three samples by performing XPS measurements, and the corresponding spectra are reported in Figure 5.9.

For the sample synthesized at pH 10, the Ag3d signals are located at 368.04 eV and 374.04 eV, maintaining the same positions as those of silver nanoplates without platinum, while Pt4f signals at 70.32 eV and 73.65 eV are attributed to Pt^0 species, and two more intense signals at 72.01 eV and 75.34 eV are typical of Pt^{2+} species [45]. This implies that, at pH 10, platinum was deposited

on the silver surface mainly in its oxidized form, and therefore the reduction reaction was not complete.

At pH 8, the Ag 3d signals exhibit a slight shift towards lower binding energies with a broadening of the FWHM, while the signals associated with Pt^0 shift in the opposite direction, towards higher binding energies. Moreover, metallic platinum species are more abundant than oxidized ones.

At pH 6, the Ag3d and Pt4f signals continue to shift in opposite directions, and the Pt^{2+} species is absent.

The shift of the Ag signals towards lower binding energies could indicate a partial oxidation of silver caused by galvanic replacement. However, considering the opposite shift observed for platinum, it can be assumed that either charge transfer or alloy formation occurs at the silver-platinum interface. Typically, the binding energy values, associated with metallic silver, are higher than 368 eV, while those for metallic platinum are around 71 eV. Nevertheless, in a study by Pham et al. on the growth of silver nanoparticles on platinum, it is reported that binding energy values are similar to those observed in the present work. In the study by Pham et al., silver was deposited on platinum, and thus Ag3d binding energies below 368 eV could not be attributed to oxidation by galvanic replacement, but rather to charge transfer driven by the electronegativity difference between platinum and silver [45].

Another hypothesis is the formation of an alloy at the silver-platinum interface, supported by the XPS analyses reported by Shuzong et al. on silver-platinum alloy nanoparticles [46]. They observed that, for any alloy composition, the binding energy values of silver were lower than 368 eV, while those of platinum were below 71 eV. At the same time, the two signals shifted in opposite directions as the platinum content in the alloy increased, as in the present work, where opposite shifts are observed with increasing platinum deposition.

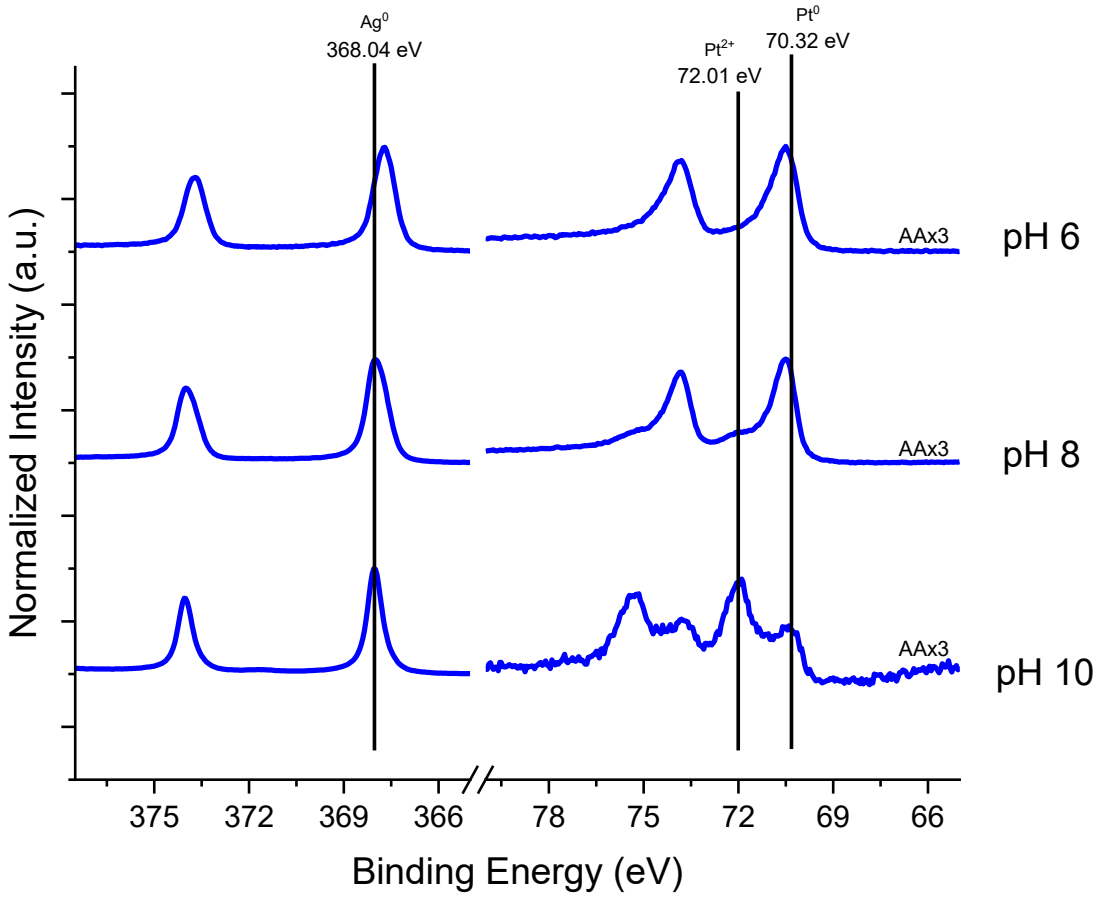

Figure 5.9. XPS spectra of Ag3d and Pt4f for the samples Ag/Pt NPTs AAx3 pH6, Ag/Pt NPTs AAx3 pH8 and Ag/Pt NPTs AAx3 pH10.

To better understand the role of ascorbic acid in the reduction of the platinum precursor, experiments were carried out by varying the amount of AA while keeping the pH constant at 8 value. The three synthesized samples were Ag/Pt NPTs AAx1 pH8, Ag/Pt NPTs AAx3 pH8, and Ag/Pt NPTs AAx5 pH8 and their TEM images are shown in Figures 5.10a, 5.10b, and 5.10c, respectively. It is evident that increasing the concentration of ascorbic acid, a greater amount of platinum is deposited, as indicated by the higher surface roughness observed for the AAx5 sample (Fig. 5.10c). This clearly demonstrates the active role of ascorbic acid in the reduction of platinum on silver.

Furthermore, the XPS spectra of the three samples (Fig. 5.10d) reveal that the silver and platinum signals shift in opposite directions as the concentration of AA, and consequently the amount of

deposited platinum, increases. This confirms the same trend observed for the samples synthesized at different pH values (fig. 5.9).

The XPS spectra in Figure 5.10d also show the presence of Pt^{2+} species, which are more prominent at lower AA concentrations. The partial reduction of Pt^{4+} to metallic platinum can be explained by referring to the study of Luty-Błocho et al., who observed that Pt^{4+} ions are reduced by ascorbic acid in two steps: first to Pt^{2+}, and then to Pt^{0} [47]. Thus, at low concentrations of ascorbic acid, not all of the precursor can be reduced to the metallic state, with part of it in the intermediate oxidation state. Instead, by increasing the concentration of the reducing agent platinum is fully reduced to the metallic state.

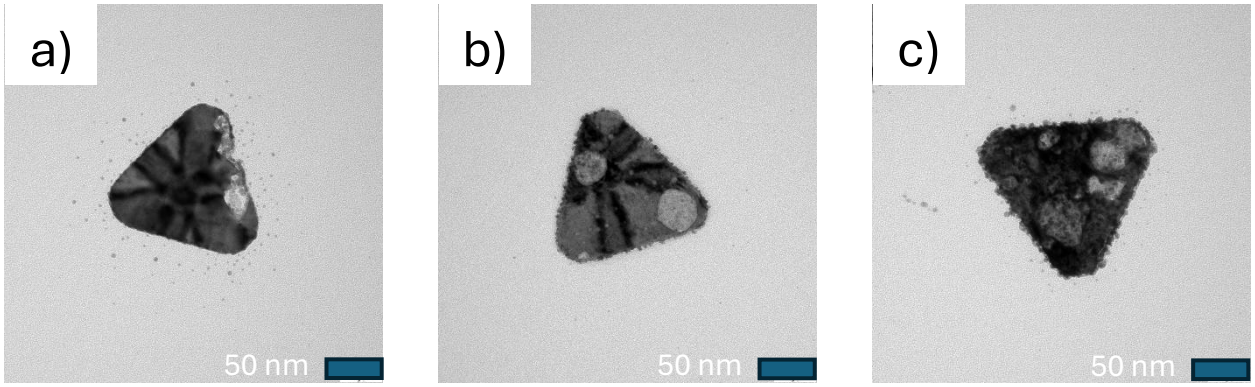

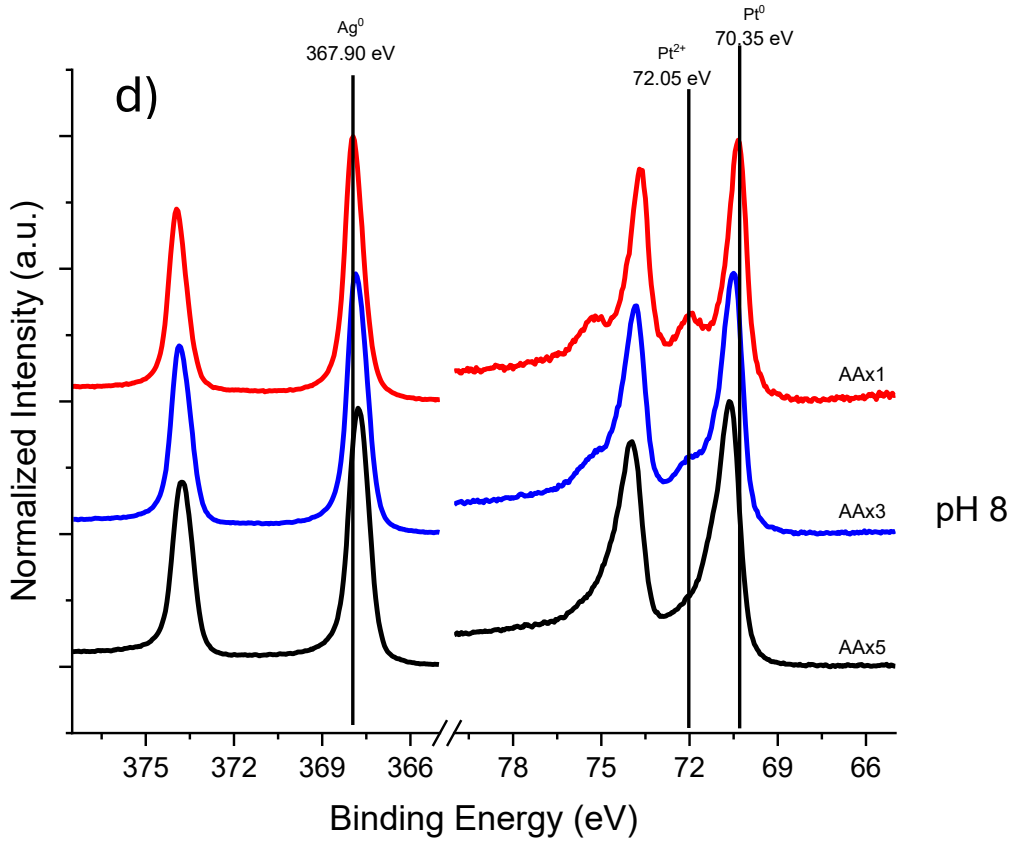

Figure 5.10. TEM images of samples a) Ag/Pt NPTs AAx1 pH8, b) Ag/Pt NPTs AAx3 pH8 and c) Ag/Pt NPTs AAx5 pH8. d) XPS spectra of Ag3d and Pt4f of the three samples.

To understand deeper insight into the reduction mechanism of platinum, it is necessary to determine what is the kinetically slow step between the reduction of Pt^{4+} to Pt^{2+} or to the reduction of Pt^{2+} to Pt^{0}. To address this question, experiments were carried out by replacing the Pt(IV) based precursor with an analogous Pt(II) precursor: K_2PtCl_4. The syntheses were performed at a fixed ascorbic acid concentration (AAx3) and at pH values of 6, 8, and 10.

Figure 5.11 shows the results of the syntheses carried out with the Pt(II) precursor (right column), compared with those obtained using Pt(IV) (left column). While the Pt(IV) based syntheses exhibited a strong dependence on pH, the Pt(II) based ones appeared almost identical across the different pH values, with a strong coverage of the nanoplates.

These findings indicate that the kinetically slow step is the reduction of Pt^{4+} to Pt^{2+}, which can be accelerated under acidic conditions due to the decreased stability of Pt(IV) complexes in solution.

In contrast, Pt(II) complexes are less affected by pH, because they are less stable than Pt(IV) complexes. This greater stability of Pt(IV) complexes explains why they are widely employed in research on anticancer drugs: their chemical inertness allows them to reach tumour sites without reacting prematurely [48].

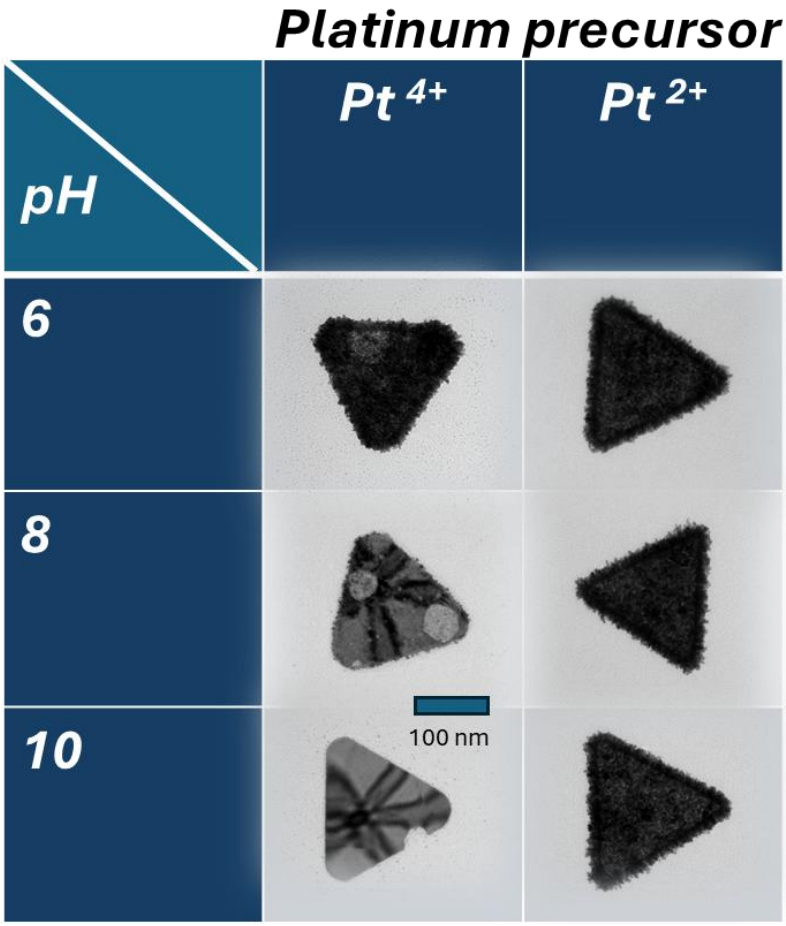

Figure 5.11. TEM images of Ag/Pt NPTs synthesized with different platinum precursor at various pH values.

5.3 Silver/Platinum Nanoplates as reliable SERS substrate

Silver/Platinum Nanoplates were employed as SERS substrates to evaluate both the stability of the signals and the repeatability of the measurements as a function of the platinum coverage. The

substrates selected for the SERS experiments were derived from the particles shown in Figure 5.7, synthesized at a fixed ascorbic acid concentration (AAx3) and at pH values of 6, 8, and 10.

To prepare the SERS samples (Figure 5.12), an aqueous solution 10^{-4} M of the probe molecule 4-MBA was incubated with the three Ag/Pt colloids for 6 hours. After incubation, unbound molecules were removed by centrifugation and the supernatant was discarded. The functionalized particles were then redispersed in water and drop-casted onto silicon wafers, allowing complete solvent evaporation. At the edges of the dried drops, a characteristic coffee ring pattern was formed, in which a high density of nanoparticles was localized. These regions were readily identified under the optical microscope integrated into the Raman system and were selected as measurement spots for SERS analysis.

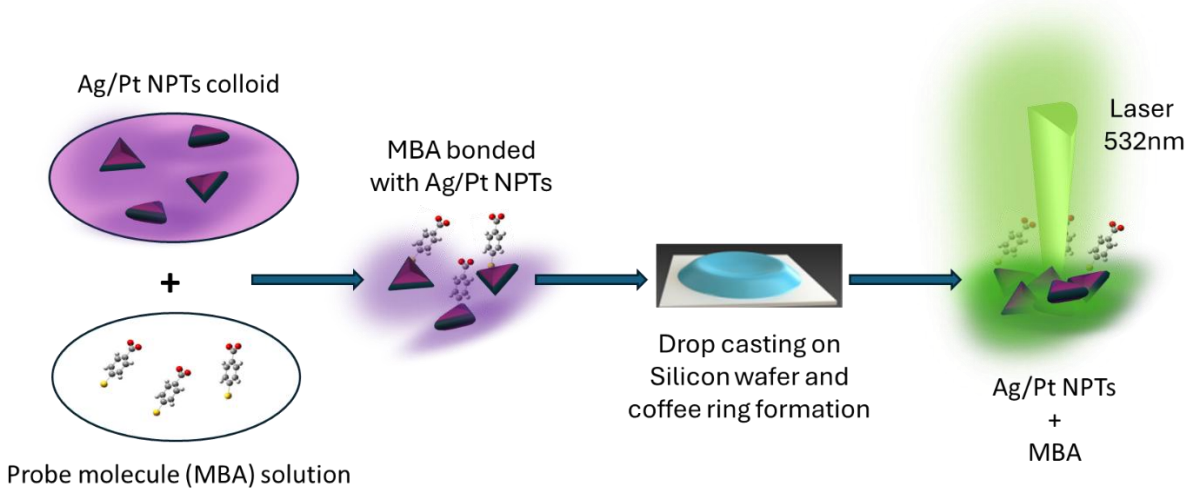

Figure 5.12. SERS samples preparation scheme.

SERS measurements were performed using a 532 nm laser (1 mW power) and a 100x objective, with spectra acquired under the following conditions: 5 s integration time, 5 accumulations. Each experiment followed the same procedure. A measurement spot was first selected using the optical microscope, then the laser was turned on and the initial spectrum was immediately recorded (defined as t = 0 min). After the acquisition, the laser remained focused on the same spot for 5

minutes before recording a second spectrum. The laser was then kept on for an additional 5 minutes (total irradiation time of 10 min), and then a third spectrum was acquired.

Figure 5.13 reports the SERS spectra of 4-MBA molecules adsorbed on different substrates and recorded at increasing laser irradiation times. Spectra in Figure 5.13 refer to the following SERS substrates: Ag NPTs without platinum (control experiment) (fig. 5.13a), Ag/Pt NPTs AAx3 pH 10 (fig 5.13b), and Ag/Pt NPTs AAx3 pH 8 (fig 5.13c). In the case of Ag/Pt NPTs AAx3 pH 6, SERS spectra were instead collected at two different laser powers (fig. 5.13d).

For 4-MBA adsorbed on silver nanoplates (fig. 5.13a), the spectra at 0 minutes exhibit intense characteristic vibrational modes, the most prominent being at 1078 cm^{-1} and 1580 cm^{-1}, corresponding to δ(CH) in-plane bending and ν(CC) stretching of the aromatic ring, respectively [49]. Upon 5 minutes of laser irradiation, the signal intensity decreases by ~30%, and after 10 minutes by nearly 70%. This reduction cannot be attributed to chemical degradation of 4-MBA, since all Raman peaks decrease proportionally and their relative intensities remain unchanged. Instead, a simultaneous decrease in the spectral background suggests a reduction in the enhancement efficiency of the substrate, with a progressive damage of the plasmonic nanostructures. Indeed, laser powers of the order of 1 mW are known to induce photothermal effects in plasmonic nanoparticle aggregates, leading to structural modifications [50]. Moreover, the appearance of a band at ~235 cm^{-1} indicates the formation of Ag–O bonds, suggesting the oxidative degradation of the silver substrate [51].

For 4-MBA molecules adsorbed on Ag/Pt NPTs AAx3 pH 10 (fig. 5.13b), the SERS signals are weaker compared to the bare silver nanoplates. This attenuation is attributed to the platinum layer, which screens the local electric field of the plasmonic core, thus reducing the enhancement effect [52]. In addition, the spectral stability is very poor, indicating a rapid substrate degradation. This behaviour can be explained by the extremely thin platinum coverage, which is insufficient to provide effective silver core protection against photothermal damage.

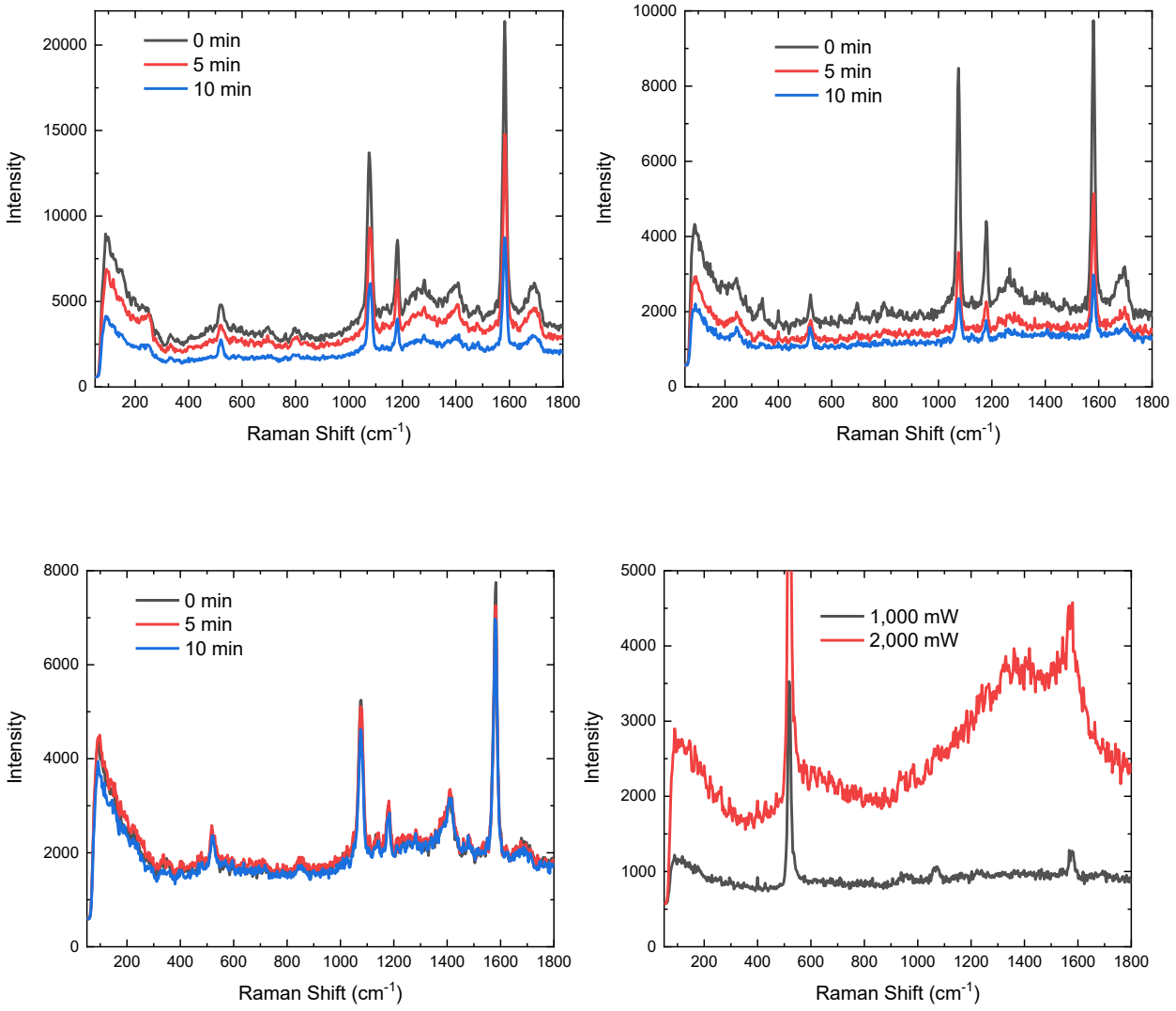

Figure 5.13. SERS spectra of 4-MBA recorded with different laser irradiation time, on the substrates a) AgNPTs, b) Ag/Pt NPTs AAx3 pH10, c) Ag/Pt NPTs AAx3 pH8. d) SERS spectra of 4-MBA on Ag/Pt NPTs AAx3 pH6 recorded at different laser powers.

In contrast, the Ag/Pt NPTs AAx3 pH 8 substrate functionalized with 4-MBA (fig. 5.13c) displays highly stable SERS signals over time. After 10 minutes of continuous laser irradiation, the signal intensity decreases by only ~5%, and no band around 235 cm^{-1} is detected, excluding silver oxidation. This demonstrates that in this case the platinum layer is sufficiently thick to obtain an effective protection of the silver core against photothermal degradation, still maintaining strong

plasmonic activity. The spectra exhibit all the characteristic vibrational modes of 4-MBA with high intensity confirming the preservation of the enhancement effect.

Finally, the SERS spectrum of 4-MBA adsorbed on Ag/Pt NPTs AAx3 pH 6 (fig. 5.13d) was acquired at two different laser powers. At 1 mW, only very weak signals of 4-MBA are observed. Instead, increasing the power to 2 mW, the spectrum shows the characteristic broad bands of amorphous carbon between 1200 and 1600 cm^{-1} [53], indicating photodegradation of the probe molecule. In this case, the platinum shell is excessively thick, quenching the plasmonic properties of the silver core and thus preventing efficient SERS enhancement.

Finally, SERS measurements were performed on ten different spots for each sample in order to evaluate signal repeatability. Figure 5.14 reports the average intensities with the corresponding standard deviations as error bars. It is evident that the AgNPTs and Ag/Pt NPTs AAx3 pH 10 substrates have not satisfied deviations, making them unsuitable as reliable SERS platforms. In contrast, the Ag/Pt NPTs AAx3 pH 8 substrate shows a standard deviation of approximately 10%, which is commonly accepted by criteria for reproducible SERS substrates [4].

These results indicate that, although the platinum covering reduce the enhancement of the silver core, at the same time a significant signal stability and repeatability can be achieved when the coverage is sufficiently thick to protect the silver but not enough to suppress the plasmonic activity. Careful control of the synthesis parameters, understanding the reduction mechanism, is crucial for the fabrication of SERS substrates that are reliable. Moreover, the ability to modulate the platinum coverage could also be used for the rational design of platinum or platinum oxide catalysts.

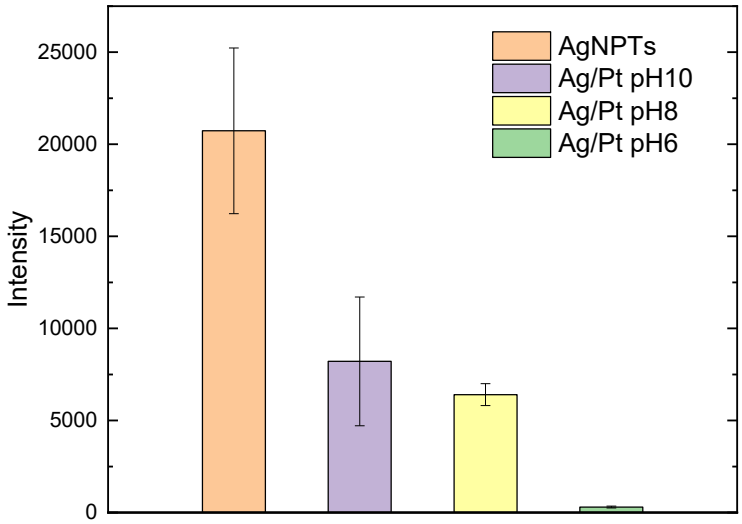

Figure 5.14. SERS average intensity and standard deviation calculated for ten 4-MBA spectra recorded on different spots on the substrates AgNPTs, Ag/Pt NPTs AAx3 pH10, Ag/Pt NPTs AAx3 pH8. Ag/Pt NPTs AAx3 pH6.

References

[1] Y. Xu, W. Aljuhani, Y. Zhang, Z. Ye, C. Li, and S. E. J. Bell, 'A practical approach to quantitative analytical surface-enhanced Raman spectroscopy', *Chem Soc Rev*, vol. 54, no. 1, pp. 62–84, Jan. 2025, doi: 10.1039/D4CS00861H.

[2] R. Goodacre, D. Graham, and K. Faulds, 'Recent developments in quantitative SERS: Moving towards absolute quantification', *TrAC Trends in Analytical Chemistry*, vol. 102, pp. 359–368, May 2018, doi: 10.1016/J.TRAC.2018.03.005.

[3] R. J. C. Brown and M. J. T. Milton, 'Nanostructures and nanostructured substrates for surface-enhanced Raman scattering (SERS)', *Journal of Raman Spectroscopy*, vol. 39, no. 10, pp. 1313–1326, 2008, doi: 10.1002/JRS.2030.

[4] M. J. Natan, 'Concluding Remarks', *Faraday Discuss*, vol. 132, no. 0, pp. 321–328, Apr. 2006, doi: 10.1039/B601494C.

[5] L. González-Cabaleiro *et al.*, 'Pushing the Limits of Lateral Flow Immunoassay by Digital SERS for the Ultralow Detection of SARS-CoV-2 Virus', *Small Science*, vol. 4, no. 11, p. 2400259, Nov. 2024, doi: 10.1002/SMSC.202400259.

[6] S. E. J. Bell and N. M. S. Sirimuthu, 'Rapid, quantitative analysis of ppm/ppb nicotine using surface-enhanced Raman scattering from polymer-encapsulated Ag nanoparticles (gel-colls)', *Analyst*, vol. 129, no. 11, pp. 1032–1036, Oct. 2004, doi: 10.1039/B408775E.

[7] A. Stewart, S. Zheng, M. R. McCourt, and S. E. J. Bell, 'Controlling assembly of mixed thiol monolayers on silver nanoparticles to tune their surface properties', *ACS Nano*, vol. 6, no. 5, pp. 3718–3726, May 2012, doi: 10.1021/NN300629Z.

[8] D. P. Cowcher, Y. Xu, and R. Goodacre, 'Portable, quantitative detection of bacillus bacterial spores using surface-enhanced raman scattering', *Anal Chem*, vol. 85, no. 6, pp. 3297–3302, Mar. 2013, doi: 10.1021/AC303657K.

[9] W. Shen *et al.*, 'Reliable quantitative SERS analysis facilitated by core-shell nanoparticles with embedded internal standards', *Angewandte Chemie - International Edition*, vol. 54, no. 25, pp. 7308–7312, Jun. 2015, doi: 10.1002/ANIE.201502171.

[10] M. P. Konrad, A. P. Doherty, and S. E. J. Bell, 'Stable and uniform SERS signals from self-assembled two-dimensional interfacial arrays of optically coupled Ag nanoparticles', *Anal Chem*, vol. 85, no. 14, pp. 6783–6789, Jul. 2013, doi: 10.1021/AC4008607.

[11] A. S. Preston, R. A. Hughes, N. L. Dominique, J. P. Camden, and S. Neretina, 'Stabilization of Plasmonic Silver Nanostructures with Ultrathin Oxide Coatings Formed Using Atomic Layer Deposition', *Journal of Physical Chemistry C*, vol. 125, no. 31, pp. 17212–17220, Aug. 2021, doi: 10.1021/ACS.JPCC.1C04599.

[12] A. Matikainen *et al.*, 'Atmospheric oxidation and carbon contamination of silver and its effect on surface-enhanced Raman spectroscopy (SERS)', *Sci Rep*, vol. 6, no. 1, pp. 1–6, Nov. 2016, doi: 10.1038/SREP37192.

[13] M. Erol, Y. Han, S. K. Stanley, C. M. Stafford, H. Du, and S. Sukhishvili, 'SERS not to be taken for granted in the presence of oxygen', *J Am Chem Soc*, vol. 131, no. 22, pp. 7480–7481, Jun. 2009, doi: 10.1021/JA807458X.

[14] L. Zhou, Q. Huang, and Y. Xia, 'Plasmon-Induced Hot Electrons in Nanostructured Materials: Generation, Collection, and Application to Photochemistry', *Chem Rev*, vol. 124, no. 14, pp. 8597–8619, Jul. 2024, doi: 10.1021/ACS.CHEMREV.4C00165.

[15] R. A. Álvarez-Puebla, 'Effects of the excitation Wavelength on the SERS spectrum', *Journal of Physical Chemistry Letters*, vol. 3, no. 7, pp. 857–866, Apr. 2012, doi: 10.1021/JZ201625J.

[16] K. Setoura, Y. Okada, and S. Hashimoto, 'CW-laser-induced morphological changes of a single gold nanoparticle on glass: observation of surface evaporation', *Physical Chemistry Chemical Physics*, vol. 16, no. 48, pp. 26938–26945, Nov. 2014, doi: 10.1039/C4CP03733B.

[17] A. Samadi, H. Klingberg, L. Jauffred, A. Kjær, P. M. Bendix, and L. B. Oddershede, 'Platinum nanoparticles: a non-toxic, effective and thermally stable alternative plasmonic material for cancer therapy and bioengineering', *Nanoscale*, vol. 10, no. 19, pp. 9097–9107, May 2018, doi: 10.1039/C8NR02275E.

[18] Z. Q. Tian *et al.*, 'Surface-enhanced Raman scattering from transition metals with special surface morphology and nanoparticle shape', *Faraday Discuss*, vol. 132, no. 0, pp. 159–170, Apr. 2006, doi: 10.1039/B507773G.

[19] K. Loza, M. Heggen, and M. Epple, 'Synthesis, Structure, Properties, and Applications of Bimetallic Nanoparticles of Noble Metals', *Adv Funct Mater*, vol. 30, no. 21, p. 1909260, May 2020, doi: 10.1002/ADFM.201909260.

[20] M. Taner, N. Sayar, I. G. Yulug, and S. Suzer, 'Synthesis, characterization and antibacterial investigation of silver–copper nanoalloys', *J Mater Chem*, vol. 21, no. 35, pp. 13150–13154, Aug. 2011, doi: 10.1039/C1JM11718A.

[21] I. Maack, K. Oldenburg, and K. Al-Shamery, ‘Controlling the architecture of Au/Pt core–shell nanocubes via platinum growth mode’, *CrystEngComm*, vol. 26, no. 47, pp. 6748–6756, Dec. 2024, doi: 10.1039/D4CE00823E.

[22] Z. Gao *et al.*, ‘Template Regeneration in Galvanic Replacement: A Route to Highly Diverse Hollow Nanostructures’, *ACS Nano*, vol. 14, no. 1, pp. 791–801, Jan. 2020, doi: 10.1021/ACSNANO.9B07781.

[23] D. Medina-Cruz *et al.*, ‘Bimetallic nanoparticles for biomedical applications: A review’, *Racing for the Surface: Antimicrobial and Interface Tissue Engineering*, pp. 397–434, Jan. 2020, doi: 10.1007/978-3-030-34471-9.

[24] H. Lin *et al.*, ‘Bimetallic nanoparticles: advances in fundamental investigations and catalytic applications’, *Environmental Science: Advances*, vol. 4, no. 1, pp. 33–56, Jan. 2025, doi: 10.1039/D4VA00241E.

[25] T. Li *et al.*, ‘Comparative toxicity study of Ag, Au, and Ag-Au bimetallic nanoparticles on Daphnia magna’, *Anal Bioanal Chem*, vol. 398, no. 2, pp. 689–700, Sep. 2010, doi: 10.1007/S00216-010-3915-1.

[26] J. Yang, X. Y. Wang, L. Zhou, F. Lu, N. Cai, and J. M. Li, ‘Highly sensitive SERS monitoring of catalytic reaction by bifunctional Ag-Pd triangular nanoplates’, *Journal of Saudi Chemical Society*, vol. 23, no. 7, pp. 887–895, Nov. 2019, doi: 10.1016/J.JSCS.2019.01.007.

[27] Y. Fan, A. Girard, M. Waals, C. Salzemann, and A. Courty, ‘Ag@Pt Core-Shell Nanoparticles for Plasmonic Catalysis’, *ACS Appl Nano Mater*, vol. 6, no. 2, pp. 1193–1202, Jan. 2023, doi: 10.1021/ACSANM.2C04767.

[28] J. Gao, X. Ren, D. Chen, F. Tang, and J. Ren, ‘Bimetallic Ag–Pt hollow nanoparticles: Synthesis and tunable surface plasmon resonance’, *Scr Mater*, vol. 57, no. 8, pp. 687–690, Oct. 2007, doi: 10.1016/J.SCRIPTAMAT.2007.06.049.

[29] J. Chen, B. Wiley, J. McLellan, Y. Xiong, Z. Y. Li, and Y. Xia, ‘Optical properties of Pd-Ag and Pt-Ag nanoboxes synthesized via galvanic replacement reactions’, *Nano Lett*, vol. 5, no. 10, pp. 2058–2062, Oct. 2005, doi: 10.1021/NL051652U.

[30] L. Yang *et al.*, ‘Tuning the Electronic Properties of Platinum in Hybrid-Nanoparticle Assemblies for use in Hydrogen Evolution Reaction’, *Angewandte Chemie - International Edition*, vol. 62, no. 25, p. e202301065, Jun. 2023, doi: 10.1002/ANIE.202301065.

[31] F. Merkoçi *et al.*, ‘Understanding galvanic replacement reactions: the case of Pt and Ag’, *Mater Today Adv*, vol. 5, p. 100037, Mar. 2020, doi: 10.1016/J.MTADV.2019.100037.

[32] W. Zhang, J. Yang, and X. Lu, ‘Tailoring galvanic replacement reaction for the preparation of Pt/Ag bimetallic hollow nanostructures with controlled number of voids’, *ACS Nano*, vol. 6, no. 8, pp. 7397–7405, Aug. 2012, doi: 10.1021/NN302590K.

[33] S. Wojtysiak, J. Solla-Gullón, P. Dłuzewski, and A. Kudelski, ‘Synthesis of core–shell silver–platinum nanoparticles, improving shell integrity’, *Colloids Surf A Physicochem Eng Asp*, vol. 441, pp. 178–183, Jan. 2014, doi: 10.1016/J.COLSURFA.2013.09.008.

[34] U. Aslam and S. Linic, ‘Addressing Challenges and Scalability in the Synthesis of Thin Uniform Metal Shells on Large Metal Nanoparticle Cores: Case Study of Ag-Pt Core-Shell Nanocubes’, *ACS Appl Mater Interfaces*, vol. 9, no. 49, pp. 43127–43132, Dec. 2017, doi: 10.1021/ACSAMI.7B14474.

[35] G. Compagnini *et al.*, ‘Growth Kinetics and Sensing Features of Colloidal Silver Nanoplates’, *J Nanomater*, vol. 2019, no. 1, p. 7084731, Jan. 2019, doi: 10.1155/2019/7084731.

[36] A. M. Ferraria, A. P. Carapeto, and A. M. Botelho Do Rego, ‘X-ray photoelectron spectroscopy: Silver salts revisited’, *Vacuum*, vol. 86, no. 12, pp. 1988–1991, Jul. 2012, doi: 10.1016/J.VACUUM.2012.05.031.

[37] B. A. Larsen *et al.*, ‘Platinum Nanoplates as Fuel Cell Electrocatalysts’, *J Electrochem Soc*, vol. 159, no. 10, pp. F622–F627, Aug. 2012, doi: 10.1149/2.029210JES/XML.

[38] H. Liu *et al.*, ‘Synthesis of ultrathin platinum nanoplates for enhanced oxygen reduction activity’, *Chem Sci*, vol. 9, no. 2, pp. 398–404, Jan. 2018, doi: 10.1039/C7SC02997G.

[39] Y. Yang, J. Liu, Z. W. Fu, and D. Qin, ‘Galvanic replacement-free deposition of au on ag for core-shell nanocubes with enhanced chemical stability and SERS activity’, *J Am Chem Soc*, vol. 136, no. 23, pp. 8153–8156, Jun. 2014, doi: 10.1021/JA502472X.

[40] X. Sun, X. Yang, Y. Zhang, Y. Ding, D. Su, and D. Qin, ‘Pt–Ag cubic nanocages with wall thickness less than 2 nm and their enhanced catalytic activity toward oxygen reduction’, *Nanoscale*, vol. 9, no. 39, pp. 15107–15114, Oct. 2017, doi: 10.1039/C7NR04366J.

[41] K. Lemma, D. A. House, N. Retta, and L. I. Elding, ‘Kinetics and mechanism for reduction of halo- and haloam(m)ine platinum(IV) complexes by l-ascorbate’, *Inorganica Chim Acta*, vol. 331, no. 1, pp. 98–108, Mar. 2002, doi: 10.1016/S0020-1693(01)00762-9.

[42] S. Kumar-Krishnan, M. Estevez-González, R. Pérez, R. Esparza, and M. Meyyappan, ‘A general seed-mediated approach to the synthesis of AgM (M = Au, Pt, and Pd) core–shell nanoplates and their SERS properties’, *RSC Adv*, vol. 7, no. 44, pp. 27170–27176, May 2017, doi: 10.1039/C7RA04301E.

[43] M. Jabbari and S. Khosravinia, ‘Thermodynamic study on the acid-base properties of antioxidant compound ascorbic acid in different NaClO4 aqueous ethanol solutions’, *J Braz Chem Soc*, vol. 27, no. 5, pp. 841–848, May 2016, doi: 10.5935/0103-5053.20150336.

[44] E. Dabbish, F. Ponte, N. Russo, and E. Sicilia, ‘Antitumor Platinium(IV) Prodrugs: A Systematic Computational Exploration of Their Reduction Mechanism by L-Ascorbic Acid’, *Inorg Chem*, vol. 58, no. 6, pp. 3851–3860, Mar. 2019, doi: 10.1021/ACS.INORGCHEM.8B03486.

[45] H. Q. Pham and T. T. Huynh, ‘Facile room-temperature fabrication of a silver–platinum nanocoral catalyst towards hydrogen evolution and methanol electro-oxidation’, *Mater Adv*, vol. 3, no. 3, pp. 1609–1616, Feb. 2022, doi: 10.1039/D1MA01077H.

[46] D. Shuzhong, X. Fanhua, and D. Jingfa, ‘The adsorption of oxygen and the oxidation of methanol on silver-platinum alloys’, *J Catal*, vol. 109, no. 1, pp. 170–179, Jan. 1988, doi: 10.1016/0021-9517(88)90195-9.

[47] M. Luty-Błocho, A. Szot, V. Hessel, and K. Fitzner, ‘The Kinetics of the Redox Reaction of Platinum(IV) Ions with Ascorbic Acid in the Presence of Oxygen’, *Materials*, vol. 16, no. 13, p. 4630, Jul. 2023, doi: 10.3390/MA16134630/S1.

[48] F. Ponte, S. Scoditti, G. Mazzone, and E. Sicilia, ‘The current status in computational exploration of Pt(iv) prodrug activation by reduction’, *Physical Chemistry Chemical Physics*, vol. 25, no. 23, pp. 15586–15599, Jun. 2023, doi: 10.1039/D3CP01150J.

[49] C. H. Ho and S. Lee, ‘SERS and DFT investigation of the adsorption behavior of 4-mercaptobenzoic acid on silver colloids’, *Colloids Surf A Physicochem Eng Asp*, vol. 474, pp. 29–35, Jun. 2015, doi: 10.1016/J.COLSURFA.2015.03.004.

[50] Z. C. Zeng, H. Wang, P. Johns, G. V. Hartland, and Z. D. Schultz, ‘Photothermal Microscopy of Coupled Nanostructures and the Impact of Nanoscale Heating in Surface-Enhanced Raman Spectroscopy’, *Journal of Physical Chemistry C*, vol. 121, no. 21, pp. 11623–11631, Jun. 2017, doi: 10.1021/ACS.JPCC.7B01220.

[51] N. Joshi, N. Jain, A. Pathak, J. Singh, R. Prasad, and C. P. Upadhyaya, ‘Biosynthesis of silver nanoparticles using Carissa carandas berries and its potential antibacterial activities’, *J Solgel Sci Technol*, vol. 86, no. 3, pp. 682–689, Jun. 2018, doi: 10.1007/S10971-018-4666-2.

[52] Z. Q. Tian *et al.*, ‘Surface-enhanced Raman scattering from transition metals with special surface morphology and nanoparticle shape’, *Faraday Discuss*, vol. 132, no. 0, pp. 159–170, Apr. 2006, doi: 10.1039/B507773G.

[53] R. Yuan *et al.*, ‘Raman spectroscopy analysis of disordered and amorphous carbon materials: A review of empirical correlations’, *Carbon N Y*, vol. 238, p. 120214, May 2025, doi: 10.1016/J.CARBON.2025.120214.

Chapter 6

6.1 Metal-free SERS

Traditionally, SERS has been dominated by plasmonic substrates based on noble metals such as gold and silver that exhibit strong plasmon resonances boosting the Raman signals by several orders of magnitude, but their remarkable performances are compromised by chemically unstablility of silver or the expensive costs of gold. Moreover, as reported in the last chapter the stability of plasmonic substrates is a challenge, as even small variations in morphology can drastically affect the SERS response. These limitations have stimulated intense research into alternative materials for SERS.

One class of alternatives is represented by plasmonic but metal-free materials, such as transition metal nitrides (e.g., TiN, ZrN). These compounds can exhibit plasmonic properties similar to noble metals, and significantly lower cost. TiN, in particular, has been investigated as a plasmonic substitute for Au and has demonstrated detectable SERS activity as showed in Figure 6.1 where is possible to appreciate the comparable intensity of SERS signals for probe molecules adsorbed on similar structures of gold and TiN [1].

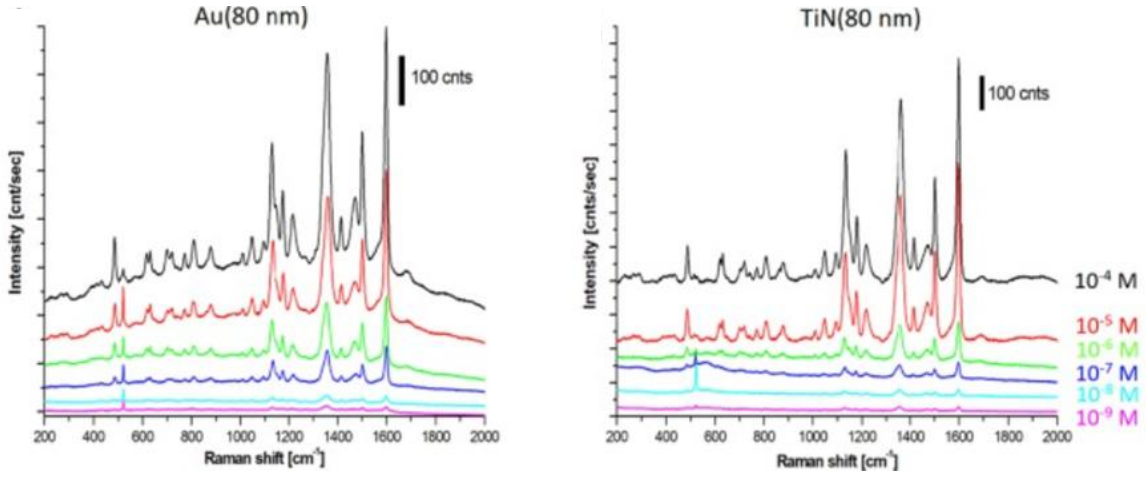

Figure 6.1. SERS spectra of tartazine recorded on similar structures of gold and TiN at different analyte concentrations [1].

Another promising strategy is the development of non-plasmonic semiconductor substrates for SERS. Unlike noble metals or nitrides, semiconductors such as TiO_2, ZnO do not show a strong LSPR. Instead, their SERS activity is predominantly governed by the chemical enhancement mechanism. This involves electronic interactions at the substrate-molecule interface: when the energy levels of the substrate and analyte are appropriately separated, light excitation can trigger charge transfer across the interface. Such CT events modify the polarizability tensor of the adsorbed molecule, resulting in enhanced Raman scattering [2].

For example, as showed in Figure 6.2, the laser of Raman apparatus can excite electrons from the valence band of the semiconductor substrate to the LUMO of the molecule adsorbate. Another way is the excitation of charge carrier from the HOMO of the molecule to the empty conduction band of the semiconductor substrate [3].

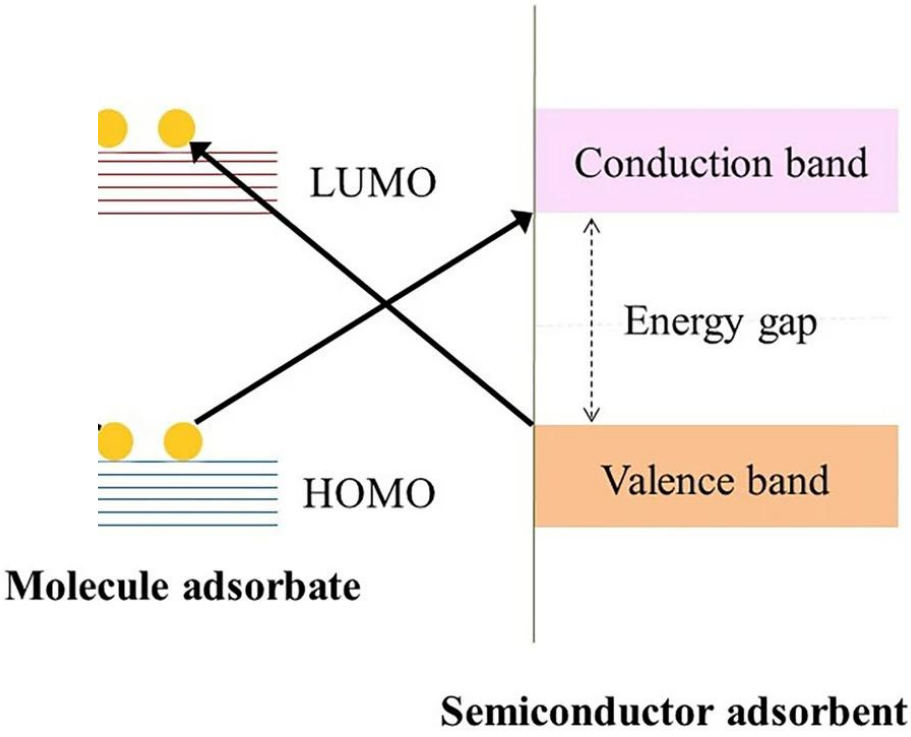

Figure 6.2. Scheme of charge transfer between semiconductor SERS substrate and adsorbed molecule [3].

The efficiency of chemical enhancement is linked to electronic band structure engineering. In particular, the introduction of defects such as oxygen or sulfur vacancies can create states located in the forbidden band of semiconductors facilitating the charge transfer [4].

Several strategies have been pursued to improve the SERS performance of semiconductor substrates. Doping with antimony ions tin oxide nanoparticles, it can tune the band gap and SERS activity was correlated with the density of free carriers and the modulation of the band structure [5]. In Figure 6.3 is showed the SERS intensity of a probe molecule in function of antimony ions doping percentage and is possible to see that a doping of 1.5% is the optimum to promote the SERS enhancement.

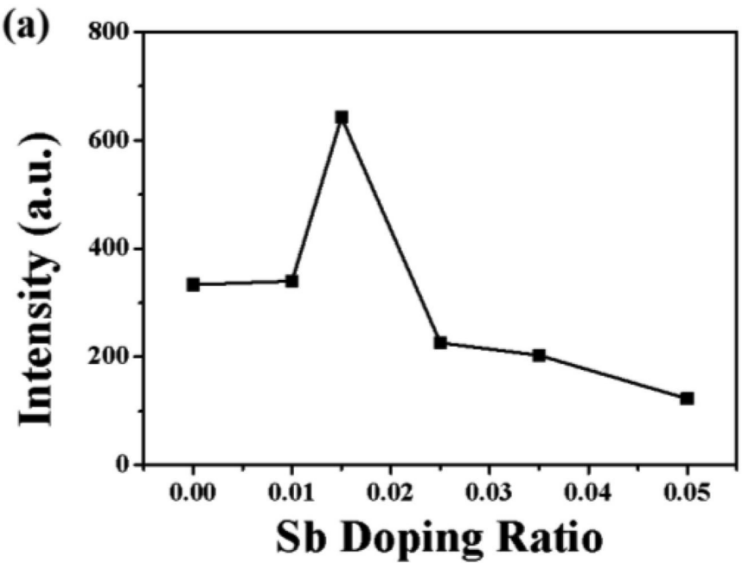

Figure 6.3. SERS intensity of a probe molecule in function of antimony ions doping percentage in tin oxide nanoparticles [5].

Among the different methods for synthesizing and modifying semiconductor substrates, laser irradiation in liquids has emerged as a particularly attractive approach. This technique combines simplicity, speed, and environmental compatibility, as it can be carried out at ambient pressure and temperature without dangerous chemicals. Pulsed laser irradiation induces intense local heating in the liquid medium, leading to fragmentation, melting, and chemical modification of particles [6].

These processes can generate new morphologies, trigger phase transformations, and introduce a high density of structural defects.

A notable example is the laser-induced modification of TiO_2, which produces so-called black titania. Using pulsed laser irradiation in liquid, white TiO_2 nanoparticles undergo partial transformation from anatase to rutile, accompanied by the creation of Ti^{3+} centers and oxygen vacancies. These changes result in defect-rich structures with enhanced visible-light absorption and improved photocatalytic activity [7]. Such results demonstrate the capacity of laser processing to engineer the band structure of semiconductors as showed in Figure 6.4: the semicondutctor energy gap is controlled changing the solvent used during the laser irradiation.

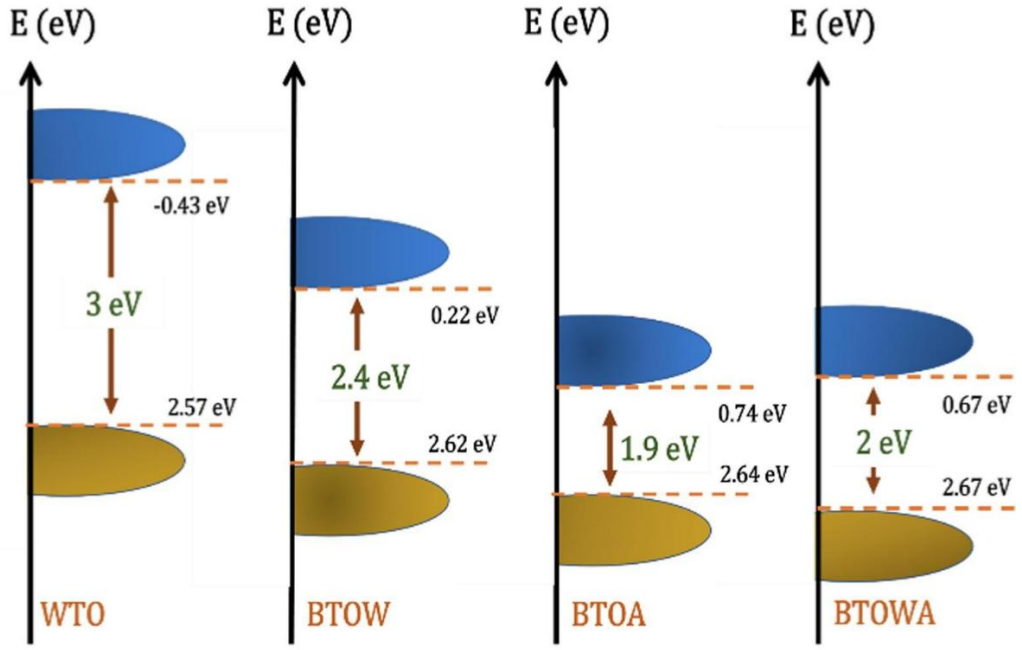

Figure 6.4. TiO_2 band gap control with pulsed laser irradiation and using different solvents [7].

In this context, defect engineering and phase modification by laser irradiation represent promising strategies to transform inactive semiconductors into efficient, metal-free SERS substrates.

In this work, it was investigated the use of molybdenum disulphide (MoS_2) as a semiconductor material for the development of metal-free SERS substrates. Specifically, it was employed pulsed laser irradiation to modify dispersions of MoS_2 nanoflakes and a set of characterization techniques is applied to elucidate the morphological, and elemental changes induced by laser processing. These analyses allow to correlate the generation of defects, sulfur vacancies, and partial MoS_2 phase transition.

Finally, laser-modified MoS_2 sample was tested as SERS substrates using 4-MBA as a probe molecule observing an improvement in SERS performances compared with unmodified MoS_2.

6.2 Laser-modified MoS_2 as a metal-free SERS substrate

Pulsed Laser Irradiation in Liquid (PLIL) of MoS_2 was carried out by irradiating 3 mL of a commercial (Graphene Supermarket) dispersion of MoS_2 nanoflakes (18 mg/L) in a water (45% vol.) / ethanol (55% vol.) mixture. Different timeframes, in a range 0-15 min, are used to induce structural changes and defects in the raw material, by using an unfocused pulsed Nd:YAG laser (Continuum, Surelite II model Nd:YAG laser, pulse duration = 5 ns, repetition rate = 10 Hz). The second harmonic of the laser (532 nm) was employed to irradiate MoS_2 sheets, with an output power of 1.1 W (fluence ~0.39 J/cm^2), a repetition rate of 10 Hz, and a pulse duration of approximately 5 ns. The laser was unfocused on the dispersion with a beam diameter of 6 mm. The dispersion was stirred during laser irradiation to prevent sedimentation of the new structures formed. After laser irradiation, modified 2D structures were collected by centrifugation (8000 r.p.m. for 5 min) and washed several times with the deionized water and dispersed in a water (45%) / ethanol (55%) mixture. The pristine and the laser-modified MoS_2 dispersions were optically characterized by UV-Vis absorption and photoluminescence (PL) spectroscopies. Absorption spectra were recorded in the 200-1000 nm range using an Agilent Cary 60 UV–Vis

spectrophotometer, while PL analyses were performed by a HORIBA Fluoromax spectrofluorometer, acquiring the emission spectra at an excitation wavelength of λ_{exc} =532 nm. Morphological investigations were carried out through TEM, STEM. For TEM characterization, 5µl of the MoS_2 dispersion (pristine and irradiated) were deposited on a copper grid and dried for 12 h before to acquire images. TEM analyses were conducted on a Zeiss 900 N instrument operated at 80 kV. STEM images were obtained with a ZEISS Merlin Gemini 2 microscope operated at 30 kV, in this case a drop of the MoS_2 irradiated dispersion was deposited on a silicon substrate. Phase changes in MoS_2 were examined by Raman spectroscopy, employing an excitation wavelength of 532 nm of a Sapphire Laser (Coherent Inc., Santa Clara, CA, USA) mounted on a WITec alpha 300 (Wissenschaftliche Instrumente und Technologie GmbH, Ulm, Germany) confocal Raman apparatus. The laser power was set at 0.5 mW to avoid potential alteration of the samples. Spectra have been collected by a 10x objective, an integration time of 10 s per spectrum and 10 accumulations on the dispersions deposited on HOPG and silicon substrates.

Elemental speciation was investigated by XPS using a Thermo Fisher ESCALAB 250Xi equipped with monochromatic Al Kα radiation and argon-assisted charge compensation. Spectra were averaged over 10 scans with a pass energy of 10 eV, a step size of 0.05 eV, and a dwell time of 100 ms. In this case 10 µl of the investigated samples were deposited on a Silicon substrate and air-dried for 12h.

Finally, SERS samples were prepared by mixing ethanolic solutions of 4-MBA (in a concentration range of 10^{-3}-10^{-6} M) with MoS_2 dispersions for 24 h allowing the adsorption of the molecules onto the MoS_2 platforms. The mixtures were centrifuged (8000 r.p.m., t=5 min) to remove the supernatant and the unbound molecules and then re-dispersed in water. Then a drop of the dispersions was deposited onto silicon wafers and after the complete water evaporation, single spectra SERS measurements were performed by acquiring signals at a laser power of 0.5 mW with an acquisition time of 10 sec and 10 accumulation per spectrum. Imaging maps were obtained by

scanning a 15 × 15 μm^2 area of the sample with a 532 nm laser using a 100× objective. The scanned area was divided into 10000 pixels, and one SERS spectrum was collected from each pixel with an acquisition time of 0.01 s and 10 accumulations per spectrum. For each scanned pixel, the intensity of the strongest SERS signal of 4-MBA at 1594 cm^{-1} was recorded, producing an intensity map in false colours that visualizes the signal distribution across the scanned area. A scheme of the overall experimental procedure to obtain defective MoS_2 architectures is reported in Figure 6.5.

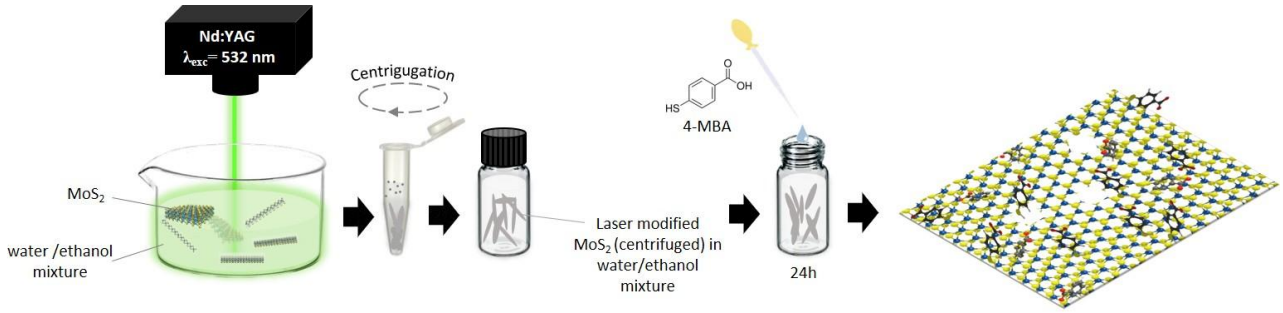

Figure 6.5. Experimental Scheme of preparation of defective MoS_2- based SERS substrates.

Figure 6.6 shows TEM images representing three different irradiation times modifying MoS_2 together with the starting MoS_2: (a) pristine MoS_2 (t=0), (b) t=5 min, (c) t=10 min and (d) t=15 min. All analysed samples were irradiated with a laser wavelength of 532 nm at a power of 1.1 W. The TEM images distinctly reveal the morphological changes; the pristine MoS_2 dispersion consists of nanoflakes with lateral dimensions of a few hundred nanometers (Figure 6.6a), after 5 minutes of irradiation, elongated structures of approximately 300 nm become well visible (Figure 6.6b), which further grow after 10 minutes (Figure 6.6c), reaching micrometric or larger dimensions after 15 minutes (Figure 6.6d).

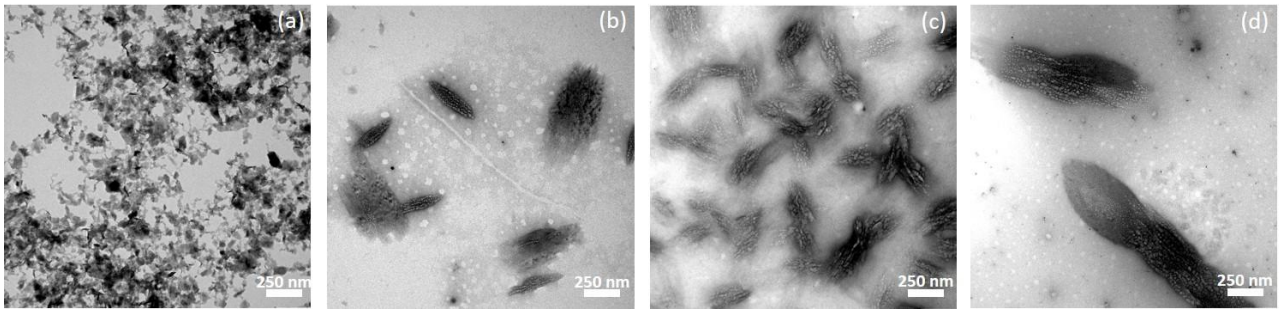

Figure 6.6. TEM images of (a) Pristine MoS_2 (t=0), (b) after 5 min, (c) 10 min and (d) 15 min of laser irradiation.

The TEM observations suggest that laser irradiation can induce either the coalescence of MoS_2 nanoflakes and/or a self-assembly process. A similar outcome was reported by Ibrahim et al., who studied the reorganization of 2D materials under femtosecond pulsed laser irradiation at a wavelength of 800 nm (non-resonant with MoS_2 absorption bands). They employed a polarized, focused beam directly applied to the dispersion and attributed the self-organization to the strong electric field at the laser focus. This field fragmented the MoS_2 nanoflakes into smaller particles, which then aligned according to the light polarization [9]. In contrast, the current study employed an unfocused nanosecond laser, leading to a less vigorous process. However, the irradiation wavelength of 532 nm corresponds to one of MoS_2 absorption bands, suggesting that electronic excitation and non-radiative relaxation mechanisms could induce localized heating, promoting coalescence. Luo et al. reported similar melting and assembly phenomena of MoS_2 nanoflakes under nanosecond green laser irradiation, which resulted in the formation of fullerene-like structures [10] [11]. To further investigate the organization of the elongated microstructures, STEM images (Figure 6.7a and 6.7b) at different magnifications, were obtained for the sample

irradiated for 15 minutes. These analyses revealed significant surface nanoroughness, which may have originated from the assembly of the initial MoS_2 flakes in random orientations.

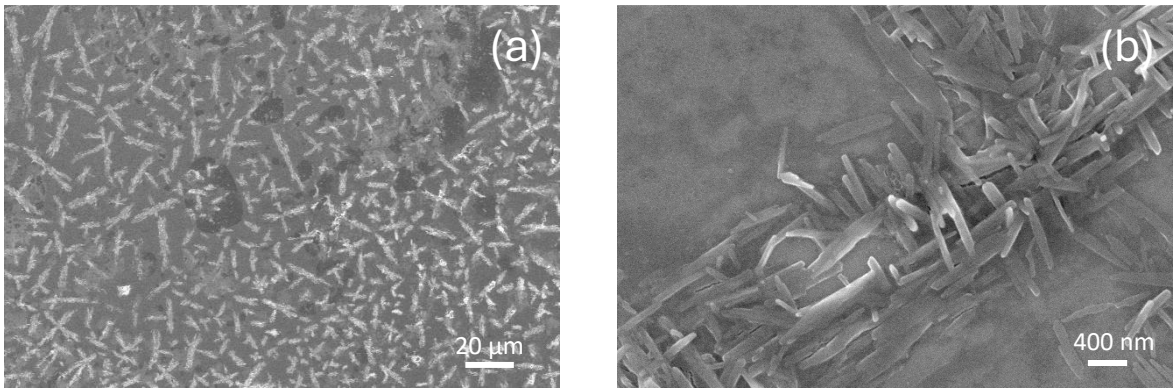

Figure 6.7. STEM images of MoS_2 laser-modified after 15 min of irradiation time.

To further investigate the growth process and study the changes in the optical properties of MoS_2, UV–Vis absorption spectra (Figure 6.8a) were recorded for the dispersion after irradiation times (t_{irr}) of 0, 5, 10, and 15 minutes. Upon analyzing the UV-Vis spectra, it is clear that, before laser exposure, the sample exhibits substantial absorption in the range of 200 nm to 700 nm, characterized by several electronic transitions. Two prominent bands are observed at 603 nm and 662 nm (typically denoted as B and A, respectively), which are associated with excitonic transitions at the K point of the Brillouin zone [12]. In addition, the absorption bands between 200 nm and 500 nm are attributed to direct transitions from the deep valence band to the conduction band, conventionally labeled as transitions C, D, and E [13]. The overall absorption spectrum of starting MoS_2 reflects the characteristic electronic structure of two-dimensional transition metal dichalcogenides, from which valuable information regarding the number of stacking layers can be inferred through the behaviour of the A excitonic transition. For instance, Castellanos-Gomez et al. demonstrated that the A excitonic peak undergoes a redshift proportional to the increasing number of MoS_2 layers [13]. In the spectrum of the non-irradiated sample, the position of the A excitonic band suggests the presence of few-layer MoS_2 (ranging from 2 to approximately 7 layers,

as indicated by the commercial dispersion specifications). During the laser modification process, the appearance of the MoS_2 dispersion gradually transitioned from pale yellow to nearly transparent. Concurrently, the absorption spectra exhibited significant changes with increasing irradiation time, showing a pronounced absorption band between 200 and 300 nm, while the visible excitonic transitions diminished drastically and nearly disappeared, indicating a significant reorganization of the electronic structure. The newly observed ultraviolet absorption band stabilized after approximately 10 minutes of irradiation, suggesting substantial alterations in the chemical structure of MoS_2 due to the pulsed-laser interaction. Absorption features within the same spectral region have previously been associated with both molybdenum oxide species [14] and sulfur vacancy formation, as well as with a phase transition from the semiconducting 2H phase to the metallic 1T phase [15].

In order to deeply understand charge transfer phenomena, it was useful to investigate possible variations in the photoluminescence (PL) response of the sample in the presence of the analyte. Thus, photoluminescence measurements were performed by exciting the samples with a 532 nm laser line, corresponding to the excitation wavelength used in SERS experiments.

In the inset of Figure 6.8b the UV-Vis absorption tail of the sample irradiated for 15 minutes is shown. Although weak, a measurable absorption is observed at 532 nm. Figure 6.8b presents the PL spectra recorded under 532 nm excitation for the pristine sample (t_{irr}=0, dashed black line), the laser-modified sample (t_{irr}=15 min, dark green line), and the same sample interacting with the probe molecule at a concentration of 10^{-4} M (light green line). For comparison the 4-MBA PL spectrum it is also shown (pink line).

The non-irradiated sample shows no detectable photoluminescence, indicating that multiple pristine layers are stacked together, resulting in an indirect bandgap that quenches the emission typically observed in monolayer samples, where the bandgap is direct [16]. This quenching arises from interlayer interactions which become increasingly significant with the addition of layers,

causing a distortion in the band structure and shifting the conduction band minimum and valence band maximum to different points in k-space [16].

In contrast, the sample irradiated for 15 minutes exhibits a weak photoluminescence band in the 600-700 nm range. Although this wavelength region corresponds to the emission of direct-bandgap MoS_2, the origin of this feature is not easy to determine. We suggest that the introduction of oxygen defects and sulfur vacancies generates new electronic states which facilitate, weakly, radiative recombination processes.

The most interesting aspect is the quenching of photoluminescence upon the addition of MBA at concentrations 10^{-4} M suggesting that the interaction between laser-modified MoS_2 and MBA inhibits radiative charge-carrier recombination, indicating the possible charge-transfer processes. We excluded dilution effects since the analyte was added from a 10^{-1} M stock solution, ensuring that the additional volume was negligible. For example, Khan et al. reported that the interaction between MoS_2 and diindenoperylene molecules results in a pronounced photoluminescence quenching, which was attributed to the formation of trap states that suppress electron transfer from the LUMO of diindenoperylene to the conduction band minima of MoS_2 [17].

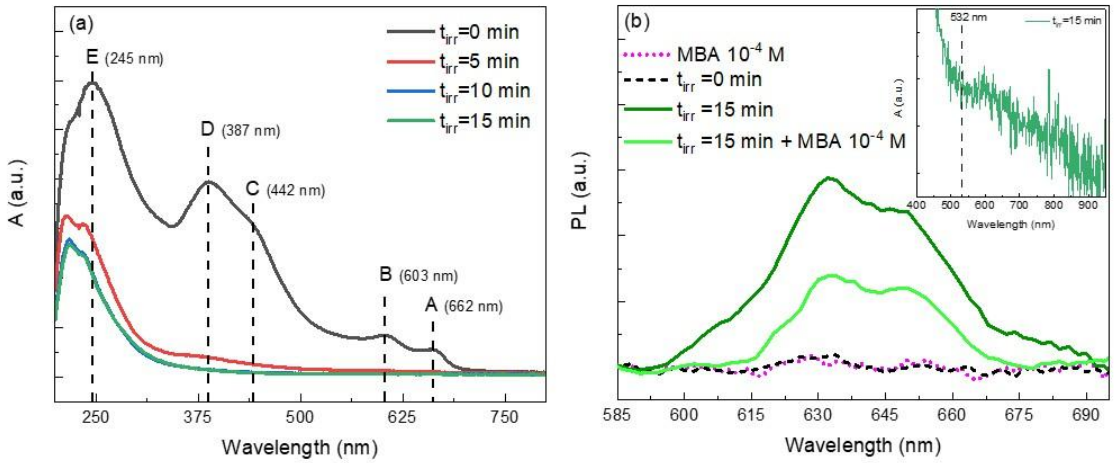

Figure 6.8. UV-Vis spectra evolution of MoS_2 dispersion during 15 min of laser irradiation (a) and (b) photoluminescence spectra under 532 nm excitation of the pristine sample (t_{irr}=0, dashed black line), MoS_2 at t_{irr}=15 min (dark green line) and in presence of 4-MBA 10^{-4}M (light green line) and of 4-MBA 10^{-4}M (pink line).

To investigate phase transitions and oxide formation, Raman spectra were recorded on MoS_2 samples as a function of irradiation time (0, 5, 10, and 15 minutes), as shown in Figure 6.9a. The spectrum of the non-irradiated sample exhibits two dominant peaks at 382.7 cm^{-1} and 406.9 cm^{-1}, corresponding to the in-plane (E_{2g}) and out-of-plane (A_{1g}) S-Mo-S vibrational modes, respectively. These features are characteristic of 2D MoS_2, and the observed ~24 cm^{-1} separation between the two modes indicates that the MoS_2 flakes consist of multilayer stacks [18].

After 5 minutes of pulsed-laser irradiation, the samples still display the E_{2g} and A_{2g} modes as the main features; however, the intensity ratio of A_{1g}/E_{2g} decreases, suggesting that the MoS_2 domains tend to reorganize into a more horizontal arrangement [19]. This observation is consistent with the TEM images, which show the formation of planar structures. Furthermore, after 10 minutes of irradiation, new Raman bands appear at 197, 222, and 352 cm^{-1}, which indicate a partial phase transition from the semiconducting 2H-MoS_2 to the more metallic 1T-MoS_2 phase, as previously reported by Yin et al. [20]. These results support the hypotheses derived from the UV-Vis absorption and XPS spectra. Additionally, several new features emerge in the 700-950 cm^{-1} region, which can be attributed to the formation of mixed molybdenum oxides [21]. These bands become more pronounced after 15 minutes of irradiation, in agreement with the XPS results.

To investigate potential atomic defects involving molybdenum and sulfur and to validate the Raman observations regarding the Mo oxidation state, precise determination of the stoichiometry of the irradiated samples is essential for correlating the composition with the enhanced properties observed in SERS experiments. Therefore, XPS analyses were carried out on the original MoS_2 dispersion and on the 15 min irradiated sample in the Mo3d region. Figure 6.9b presents the XPS spectrum of the pristine MoS_2 sample, which is characterized by two spin-orbit split components centered at binding energies of 229.56 eV and 232.69 eV, typical of molybdenum atoms bonded to sulfur in 2D MoS_2 structures [22]. Additionally, a third signal corresponding to the sulfur 2s core level is observed at 226.72 eV, slightly overlapping with the Mo signals, further confirming

the presence of MoS_2. Weaker Mo 3d components were also extracted through spectral fitting, which can be attributed to the presence of sulfur vacancies at the flake edges or small amounts of oxidized Mo atoms.

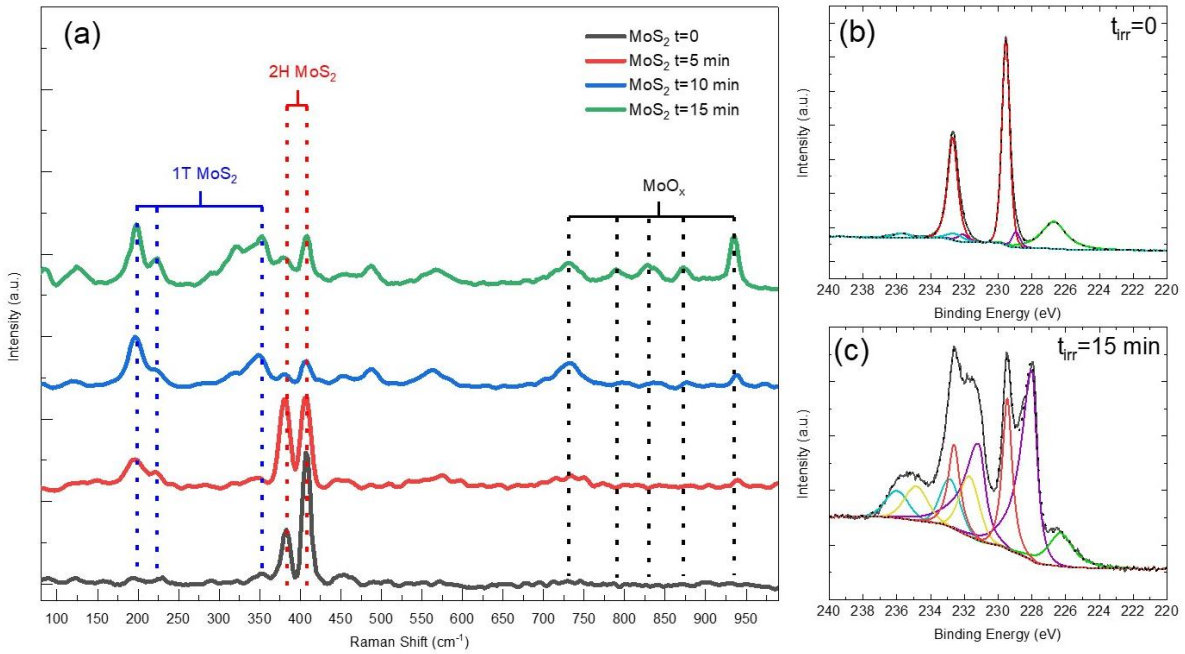

Figure 6.9. Raman spectra vs irradiation time (a) XPS spectra of Mo3d region of (b) pristine and (c) 15 min laser-modified samples.

The XPS spectrum of the laser-modified sample, irradiated for 15 minutes (Figure 6.9c), exhibits significant differences compared to the pristine material, indicating that molybdenum underwent chemical transformations involving changes in oxidation states and bonding configurations. Deconvolution of the Mo 3d region revealed components corresponding to MoS_2 at 229.45 eV and 232.66 eV, similar to the pristine sample. However, additional peaks appeared: signals at 232.90 eV and 236.04 eV, characteristic of MoO_3, as well as components at 231.70 eV and 234.85 eV, attributed to sub-stoichiometric molybdenum oxides (MoO_x) [23]. Furthermore, peaks at 228.04 eV and 231.21 eV indicate the presence of metallic-like Mo species, as evidenced by their lower binding energies and the characteristic tailing of metallic states. This metallic behaviour can be

ascribed to sulfur vacancies leading to MoS_{2-x} species but may also arise from a structural phase transition of MoS_2 [24]. Indeed, several studies have reported that shifts toward lower binding energies are associated with the metallic 1T phase of MoS_2, whereas the pristine material is typically in the semiconducting 2H phase [25].

From the XPS spectrum of the laser-modified sample, the atomic percentages of molybdenum in the various chemical species were also determined. From the XPS spectrum of the laser-modified sample, the atomic percentages of molybdenum in the various chemical species were determined. The area of the peaks at 232.90 eV, 236.04 eV, 231.70 eV, and 234.85 eV account for 28.4 % of the total Mo 3d signals and correspond to mixed oxide phases formed as a result of laser irradiation. The area peaks at 228.04 eV and 231.21 eV represent the largest fraction of the sample, amounting to 48.7 %, and are attributed to the formation of sulfur vacancies. Finally, the peaks at 229.45 eV and 232.66 eV correspond to the remaining 22.9 % of unmodified MoS_2, indicating that the irradiation process induced a significant alteration in the molybdenum speciation.

Considering these data, the presence of different phases enables the modification of the electronic properties of the original MoS_2, enhancing charge transfer phenomena and thus increasing its potential as a substrate for SERS sensing. Specifically, the enhanced properties of this non-plasmonic SERS substrate can be attributed to charge transfer, which results from the increased polarizability of the molecules interacting with the SERS substrate, combined with the electromagnetic effects arising from the conductive 1T-phase. Additionally, UV-Vis and Raman spectra suggest the presence of defective molybdenum oxides (MoO_x), which are also considered SERS-active oxide semiconductors [26]. These oxides contribute to the CM, controlled by defect density, leading to energy levels that align with those of the probe molecule, thereby facilitating charge transfer phenomena. At support of this, Zheng et al. demonstrated that thermal treatment of MoS_2 induces partial oxidation via oxygen substitution at sulfur sites, creating defect states that significantly enhance the chemical contribution to SERS, improving sensitivity by several orders

of magnitude [8]. Yin et al. observed that the 1T phase of MoS_2 dramatically enhances the SERS response of copper phthalocyanine via substrate-analyte charge transfer, while pristine MoS_2 exhibited weak and inefficient charge transfer, leading to low SERS signals [21].

Pristine MoS_2 and laser-modified samples were therefore employed as SERS substrates to investigate the effect of defect introduction into the MoS_2 structure. SERS measurements were performed on MoS_2 substrates subjected to different laser irradiation times to assess how laser-induced modifications enhance their SERS performance for detecting adsorbed 4-MBA.

Figure 6.10a shows the SERS spectra of 4-MBA (10^{-4} M) adsorbed on MoS_2 substrates irradiated for 0, 5, 10, and 15 minutes. The spectra collected on pristine MoS_2 are nearly flat, confirming that the unmodified material is not an efficient SERS substrate. In contrast, laser-modified MoS_2 displays a progressive increase in SERS signal intensity with increasing irradiation time, demonstrating that laser exposure plays a crucial role in activating the SERS response. The spectra of irradiated samples show the characteristic 4-MBA vibrational bands at 1078 cm^{-1} and 1595 cm^{-1}, corresponding to the in-plane δ(CH) and aromatic ν(CC) stretching modes, respectively [27]. The gradual intensification of these peaks as irradiation time increases clearly indicates that laser modification enhances the adsorption of 4-MBA molecules and activates a chemical enhancement mechanism.

As discussed in previous sections, XPS and Raman data revealed that laser irradiation induces a high density of sulfur vacancies and other structural defects in MoS_2, along with a partial conversion from the semiconductor 2H phase to the metallic 1T phase, introducing new states in the electronic band structure. As discussed previously, these states may facilitate alignment between the MoS_2 electronic levels and the HOMO-LUMO levels of 4-MBA, enabling charge transfer under laser excitation. PL measurements further support this hypothesis, as the quenching of the intrinsic MoS_2 emission in the presence of 4-MBA confirms the electronic coupling between the substrate, the analyte, and the excitation wavelength.

Previous works report the role of defects, and 1T phase to improve the SERS performance of MoS_2. Zheng et al. demonstrated that thermal treatment of MoS_2 promotes partial oxidation and oxygen substitution at sulfur sites, leading to the formation of defect states that significantly increase the chemical enhancement contribution, boosting SERS sensitivity by several orders of magnitude [8]. Yin et al. reported that the metallic 1T phase of MoS_2 dramatically enhances the SERS response of copper phthalocyanine, attributing the effect to efficient substrate-analyte charge transfer, whereas pristine 2H-MoS_2 exhibited negligible enhancement [21].

Among the investigated samples, the substrate irradiated for 15 minutes exhibited the strongest enhancement and was therefore selected to study the detection capability over a range of 4-MBA concentrations (10^{-3}-10^{-6} M), as shown in Figure 6.10b. At higher concentrations (10^{-3} and 10^{-4} M), the spectra show intense bands at 1078 and 1595 cm^{-1}, along with weaker secondary features, indicating strong signal amplification. When the concentration decreases to 10^{-5} M, the two main peaks remain clearly visible, while at 10^{-6} M, they are still detectable but close to the noise level, suggesting that this concentration represents the detection limit of the system.

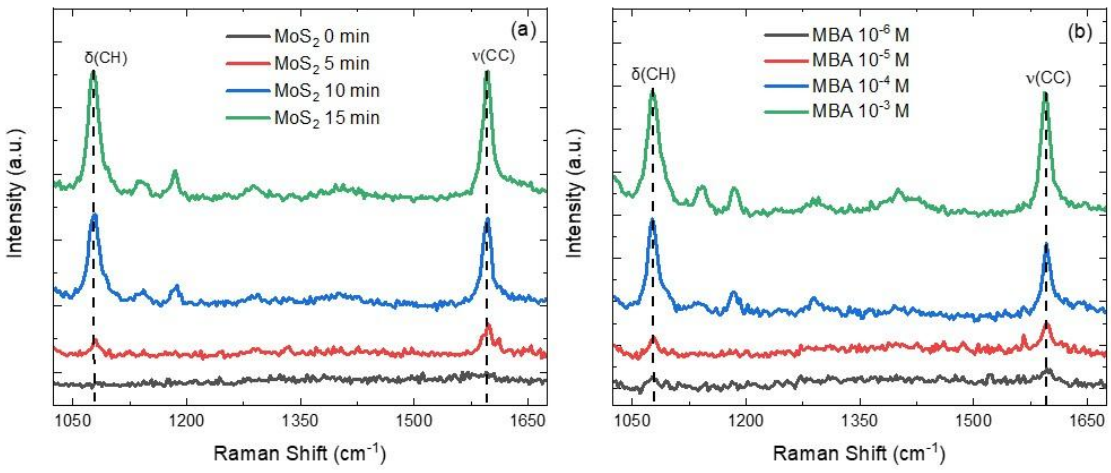

Figure 6.10. SERS spectra vs irradiation time of 4-MBA 10^{-4}M (a) and at different 4-MBA concentration for 15 min laser-modified MoS_2 (b).

To assess the uniformity of the SERS response, Figure 6.11a displays SERS spectra of 4-MBA (10^{-4} M) acquired from different regions of interest (ROI), labeled "1-9" in the SERS map (Figure 6.11b), obtained selecting the 1595 cm^{-1} stretching vibration of the C=C bond (bright regions). Spectra show signals of comparable intensity corresponding to the characteristic fingerprint of 4-MBA. This indicates that 4-MBA molecules are uniformly adsorbed onto the substrate surface and detectable via charge transfer phenomena.

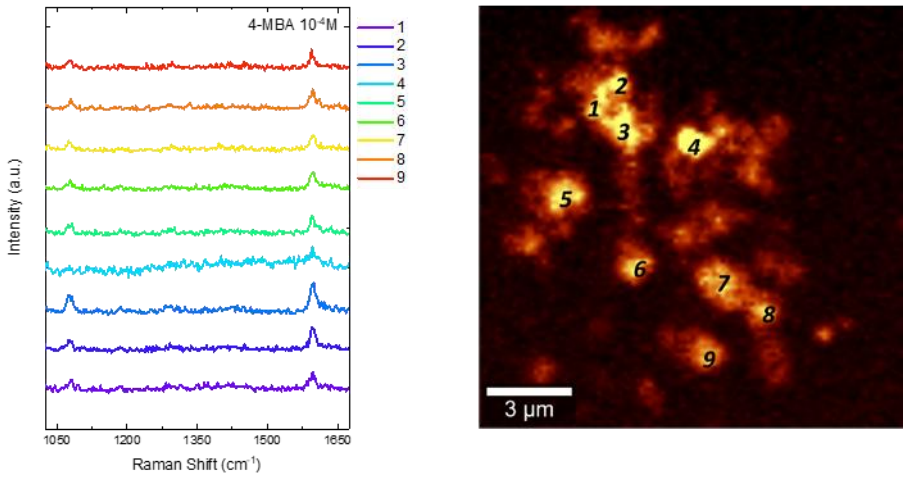

Figure 6.11. SERS spectra of 4-MBA 10^{-4}M onto 15 min laser-modified MoS_2 (a) extracted from SERS map of 1594 cm^{-1} 4-MBA signal ROI labelled as "1-9".

To rationalize the experimental findings, first-principles density functional theory (DFT) simulations were performed using the Vienna Ab-initio Simulation Package (VASP, version 6.5.1). The models included pristine semiconducting 2H-MoS_2, sulfur-defective MoS_2 (MoS_2-VS), and metallic 1T-MoS_2, both in isolation and with adsorbed 4-MBA molecules (The adsorbed systems are called 4-MBA@VS and 4-MBA@1T).

The integrated charge-density differences (Δρ) (Figure 6.12) provide a quantitative picture of the interfacial interaction. For 4-MBA@VS, moderate charge redistribution is observed, whereas 4-MBA@1T exhibits a much higher Δρ amplitude, indicating stronger electronic coupling and more efficient charge donation from MoS_2 to the molecule. The results confirm that the laser-induced

structural transformation (2H → 1T) and defect creation (VS) synergistically promote a charge-transfer resonance mechanism responsible for the enhanced Raman response.

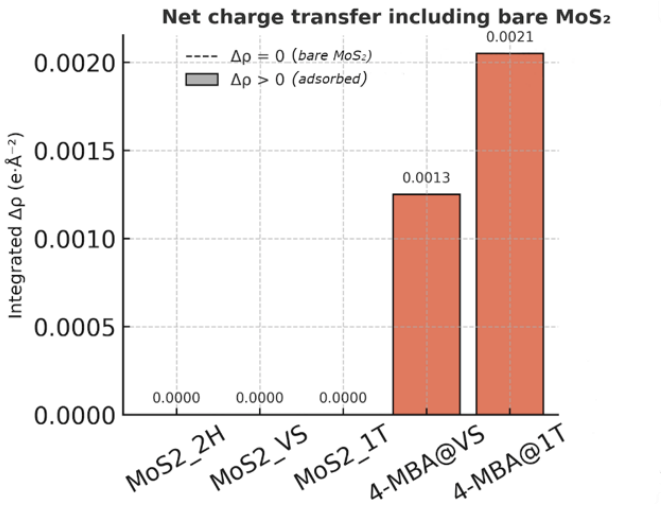

Figure 6.12. Integrated charge-density difference (Δρ) for bare and adsorbed MoS_2 systems.

Therefore, this study highlights the critical role of phase transitions and defects in modulating charge transfer and provides new insights into the chemical mechanisms that govern SERS activity in laser-treated MoS_2. PLIL emerges as an alternative, fast and clean route for tailoring the electronic structure of two-dimensional semiconductor materials, producing MoS_2-based non-plasmonic SERS platforms potentially scalable into advanced chemical and biological detection systems.

References

[1] J. Krajczewski *et al.*, 'The battle for the future of SERS – TiN vs Au thin films with the same morphology', *Appl Surf Sci*, vol. 618, p. 156703, May 2023, doi: 10.1016/J.APSUSC.2023.156703.

[2] L. Lan, Y. Gao, X. Fan, M. Li, Q. Hao, and T. Qiu, 'The origin of ultrasensitive SERS sensing beyond plasmonics', *Frontiers of Physics 2021 16:4*, vol. 16, no. 4, pp. 1–26, Mar. 2021, doi: 10.1007/S11467-021-1047-Z.

[3] M. Magdy, ‘A Conceptual Overview of Surface-Enhanced Raman Scattering (SERS)’, *Plasmonics*, vol. 18, no. 2, pp. 803–809, Apr. 2023, doi: 10.1007/S11468-023-01807-Y.

[4] Z. Zheng *et al.*, ‘Semiconductor SERS enhancement enabled by oxygen incorporation’, *Nat Commun*, vol. 8, no. 1, pp. 1–10, Dec. 2017, doi: 10.1038/S41467-017-02166-Z.

[5] M. Zhang, Y. Wang, Y. Ma, X. Wang, B. Zhao, and W. Ruan, ‘Study of charge transfer effect in Surface-Enhanced Raman scattering (SERS) by using Antimony-doped tin oxide (ATO) nanoparticles as substrates with tunable optical band gaps and free charge carrier densities’, *Spectrochim Acta A Mol Biomol Spectrosc*, vol. 264, p. 120288, Jan. 2022, doi: 10.1016/J.SAA.2021.120288.

[6] H. Zeng *et al.*, ‘Nanomaterials via laser ablation/irradiation in liquid: A review’, *Adv Funct Mater*, vol. 22, no. 7, pp. 1333–1353, Apr. 2012, doi: 10.1002.

[7] P. Raveendran Nair *et al.*, ‘Black titanium dioxide nanocolloids by laser irradiation in liquids for visible light photo-catalytic/electrochemical applications’, *Appl Surf Sci*, vol. 623, p. 157096, Jun. 2023, doi: 10.1016/J.APSUSC.2023.157096.

[8] Z. Zheng *et al.*, “Semiconductor SERS enhancement enabled by oxygen incorporation,” *Nat Commun*, vol. 8, no. 1, pp. 1–10, Dec. 2017, doi: 10.1038/S41467-017-02166-Z.

[9] K. Ibrahim *et al.*, “Laser-Directed Assembly of Nanorods of 2D Materials,” *Small*, vol. 15, no. 46, p. 1904415, Nov. 2019, doi: 10.1002/SMLL.201904415.

[10] T. Luo *et al.*, “Green laser irradiation-stimulated fullerene-like MoS2 nanospheres for tribological applications,” *Tribol Int*, vol. 122, pp. 119–124, Jun. 2018, doi: 10.1016/J.TRIBOINT.2018.02.040.

[11] M. Sinatra, G. Messina, G. R. Compagnini, and S. Scalese, “Formation of inorganic fullerene-like MoS2 nanostructures by laser ablation in water,” 2023, Accessed: Oct. 23, 2025. [Online]. Available: https://www.iris.unict.it/handle/20.500.11769/100108

[12] S. Ghayeb Zamharir, R. Karimzadeh, and S. H. Aboutalebi, “Laser-assisted tunable optical nonlinearity in liquid-phase exfoliated MoS2 dispersion,” *Appl Phys A Mater Sci Process*, vol. 124, no. 10, Oct. 2018, doi: 10.1007/S00339-018-2115-2.

[13] A. Mosleh *et al.*, “Transmission spectra of some transition metal dichalcogenides. II. Group VIA: trigonal prismatic coordination,” *Journal of Physics C: Solid State Physics*, vol. 5, no. 24, p. 3540, Dec. 1972, doi: 10.1088/0022-3719/5/24/016.

[14] G. Kong, X. Du, X. Cai, P. Feng, X. Wang, and F. Akhtar, “Recycling Molybdenum Oxides from Waste Molybdenum Disilicides: Oxidation Experimental Study and Photocatalytic Properties,” *Oxidation of Metals*, vol. 92, no. 1–2, pp. 1–12, Aug. 2019, doi: 10.1007/S11085-019-09909-X.

[15] M. Stavrou, N. Chazapis, E. Nikoli, R. Arenal, N. Tagmatarchis, and S. Couris, “Crystalline Phase Effects on the Nonlinear Optical Response of MoS2 and WS2 Nanosheets,” *ACS Appl Nano Mater*, vol. 5, no. 11, pp. 16674–16686, May 2023, doi: 10.1021/acsanm.2c03709.

[16] B. Han and Y. H. Hu, “MoS2 as a co-catalyst for photocatalytic hydrogen production from water,” *Energy Sci Eng*, vol. 4, no. 5, pp. 285–304, Oct. 2016, doi: 10.1002/ESE3.128.

[17] Y. Khan, S. M. Obaidulla, M. Rezwan Habib, Y. Kong, and M. Xu, “Anomalous photoluminescence quenching in DIP/MoS2 van der Waals heterostructure: Strong charge transfer and a modified interface,” *Appl Surf Sci*, vol. 530, p. 147213, Nov. 2020, doi: 10.1016/J.APSUSC.2020.147213.

[18] H. Li *et al.*, “From Bulk to Monolayer MoS2: Evolution of Raman Scattering,” *Adv Funct Mater*, vol. 22, no. 7, pp. 1385–1390, Apr. 2012, doi: 10.1002/ADFM.201102111.

[19] H. P. Chang, M. Hofmann, Y. P. Hsieh, Y. S. Chen, and J. G. Lin, “Correlation of grain orientations and the thickness of gradient MoS2 films,” *RSC Adv*, vol. 11, no. 54, pp. 34269–34274, Oct. 2021, doi: 10.1039/D1RA05982C.

[20] F. Ye *et al.*, “Synthesis of Two-Dimensional Plasmonic Molybdenum Oxide Nanomaterials by Femtosecond Laser Irradiation,” *Chemistry of Materials*, vol. 33, no. 12, pp. 4510–4521, Jun. 2021, doi: 10.1021/ACS.CHEMMATER.1C00732.

[21] Y. Yin *et al.*, “Significantly Increased Raman Enhancement on MoX2 (X = S, Se) Monolayers upon Phase Transition,” *Adv Funct Mater*, vol. 27, no. 16, p. 1606694, Apr. 2017, doi: 10.1002/ADFM.201606694.

[22] B. Li *et al.*, “Preparation of Monolayer MoS2 Quantum Dots using Temporally Shaped Femtosecond Laser Ablation of Bulk MoS2 Targets in Water,” *Sci Rep*, vol. 7, no. 1, pp. 1–12, Dec. 2017, doi: 10.1038/S41598-017-10632-3.

[23] H. N. Tran *et al.*, “17% Non-Fullerene Organic Solar Cells with Annealing-Free Aqueous MoOx,” *Advanced Science*, vol. 7, no. 21, p. 2002395, Nov. 2020, doi: 10.1002/ADVS.202002395.

[24] Q. Xu *et al.*, “Enlarged Interlayer Spacing of Marigold-Shaped 1T-MoS2 with Sulfur Vacancies via Oxygen-Assisted Phosphorus Embedding for Rechargeable Zinc-Ion Batteries,” *Nanomaterials*, vol. 13, no. 7, p. 1185, Apr. 2023, doi: 10.3390/NANO13071185/S1.

[25] D. Mouloua *et al.*, “Giant Photodegradation Rate Enabled by Vertically Grown 1T/2H MoS2 Catalyst on Top of Silver Nanoparticles,” *Advanced Energy and Sustainability Research*, vol. 5, no. 12, Dec. 2024, doi: 10.1002/AESR.202400213.

[26] C. Gu, D. Li, S. Zeng, T. Jiang, X. Shen, and H. Zhang, “Synthesis and defect engineering of molybdenum oxides and their SERS applications,” *Nanoscale*, vol. 13, no. 11, pp. 5620–5651, Mar. 2021, doi: 10.1039/D0NR07779H.

[27] C. H. Ho and S. Lee, “SERS and DFT investigation of the adsorption behavior of 4-mercaptobenzoic acid on silver colloids,” *Colloids Surf A Physicochem Eng Asp*, vol. 474, pp. 29–35, Jun. 2015, doi: 10.1016/J.COLSURFA.2015.03.004.

Conclusions

This work demonstrates how morphology and composition control in nanostructured materials can be used to develop SERS platforms through systematic synthesis, and characterization showing that silver-based nanostructures and defect-engineered 2D semiconductors can be optimized to achieve strong field enhancement, tunable catalytic activity, and improved stability.

Silver nanoflowers (AgNFs) proved to be the most effective plasmonic substrate among the investigated systems. Their hierarchical nanoroughness, characterized by petal-like protrusions, provided a dense distribution of electromagnetic hot-spots. This enabled not only strong enhancement factors but also the capability to monitor reactions at the single-particle level across multiple excitation wavelengths.

The plasmon-driven dimerization of 4-nitrothiophenol (4-NTP) into 4,4′-dimercaptoazobenzene (DMAB) was successfully monitored using 532 nm excitation promoted efficient dimerization, while irradiation at 785 nm favored alternative reduction pathways, promoting 4-aminothiophenol (4-ATP).

In contrast, silver nanospheres (AgNSs) and nanoplates (AgNPTs) offered lower enhancement, yet their comparative analysis revealed critical insights and that morphology directly governs hot-spot density, and SERS performances. These findings highlight that both structural design and optical parameters can be strategically tuned to select reaction pathways and another purpose involves extending plasmon-driven chemistry beyond dimerization. In particular, the possibility of driving polymerization reactions directly on plasmonic substrates represents an exciting opportunity. Using trifunctional molecules, plasmon-assisted polymer networks could be fabricated in situ, enabling nanoscale materials synthesis under light control.

To address the known instability of silver, nanoplates were coated with platinum shells whose growth was carefully controlled by tuning the experimental conditions. It was observed that the reduction mechanism strongly depends on both the pH of the medium and the oxidation state of platinum precursors. By adjusting these parameters, it was possible to obtain well-defined Pt coatings that preserved the strong plasmonic response of the silver core. This approach led to more stable SERS substrates, demonstrating that compositional engineering, when combined with controlled growth mechanisms, is a powerful strategy to enhance practical applicability. From this study, a first direction concerns the validation of these substrates with analytes of real-world relevance. Environmental pollutants, biomarkers, or industrial intermediates could be tested to demonstrate the feasibility of SERS-based detection in practical scenarios.

Finally, beyond noble metals, laser irradiation in liquid was employed to modify MoS_2, leading to the formation of microstructures containing sulfur vacancies and molybdenum oxides. These defect sites promoted the self-assembly of MoS_2 flakes into hierarchical architectures capable of generating strong chemical enhancement contributions. As a result, these modified 2D semiconductors provided SERS activity through charge-transfer mechanisms, opening a sustainable route toward metal-free substrates that complement traditional plasmonic systems using a low cost, flexible and practical technique as laser irradiation. Beyond MoS_2, other layered systems such as hexagonal boron nitride (h-BN) could be modified by laser-assisted techniques to introduce tailored defects. This could expand the role of metal-free materials for SERS applications.

List of Publications

- M. Condorelli, **A. Brancato***, C. Longo, M. Barcellona, M. Fragalà, E. Fazio, G. Compagnini, L. D'Urso. Tuning plasmonic reactivity: Influence of nanostructure, and wavelength on the dimerization of 4-NTP. Journal of Catalysis, Volume 450, 2025, 116267, ISSN 0021-9517. https://doi.org/10.1016/j.jcat.2025.116267

- V. Cantaro*, A. Sciuto, **A. Brancato**, G. Compagnini, G. D'Arrigo. Plasmonic Ag Nanoparticles on SiC for Use as SERS Substrate and in Integrated Optical Sensors for Bio-Chemical Applications. Key Engineering Materials, vol. 984, Trans Tech Publications, Ltd., 2024, pp. 63–69. https://doi.org/10.4028/p-x4ecaa

- **A. Brancato**, M. Condorelli*, L. Salemi, V. Scardaci, M. Fragalà, M. Barcellona, G. Compagnini, L. D'Urso. Ag nanoflowers as single-particle, multi-wavelength SERS active platforms. Surfaces and Interfaces, Volume 40, 2023, 103157, ISSN 2468-0230. https://doi.org/10.1016/j.surfin.2023.103157

- M. Pulvirenti, V. Scardaci*, L. Catanzaro, M. Scuderi, G. Sfuncia, **A. Brancato**, M. Condorelli, L. D'Urso, G. Compagnini. Study and characterization of the gold nanoparticle's formation mechanism by re-irradiation of linear bromide induced gold nanoparticles chain. (submitted)

- **A. Brancato**, M. Condorelli*, V. Scardaci, E. Fazio, G. Forte, L. D'Urso, G. Compagnini. Defect- engineering in MoS_2 layers for Surface Enhanced Raman Scattering. (submitted)

- **A. Brancato**, L. D'Urso, K. Al-Shamery. Mechanistic study of Silver/Platinum Nanoplates synthesis and their application as reliable SERS substrate. (in preparation)

Schools and Conferences attended

- 7th International Conference on "Nanoscience and Nanotechnology" (ICONN), March 27-29, 2023. Oral communication: *Ag Nanoflowers as multi-wavelength SERS active platform*. **A. Brancato**, M. Condorelli, G. Compagnini, L. D'Urso.

- VISPEC school & conference on Vibrational Spectroscopy, June 12-16, 2023, Perugia (Italy). Poster communication: *AgNFs as single-particle, multi-wavelength SERS platform.* **A. Brancato**, M. Condorelli, G. Compagnini, L. D'Urso.

- School of Physical Chemistry 2023 - Frontiers in Materials Physical Chemistry: Nanostructures and Nanomaterials, June 19-23, 2023, Verbania (Italy). Poster communication: *Ag Nanoflowers as plasmonic platforms for photocatalytic applications.* **A. Brancato**, M. Condorelli, C. Longo, G. Compagnini, L. D'Urso.

- 17th International Conference on Laser Ablation (COLA 2024), September 29 - October 4, 2024, Hersonissos (Greece). Poster communication: *MoS_2 structures modified by laser irradiation for semiconductor-SERS sensing*. **A. Brancato**, L. D'Urso, M. Condorelli, V. Scardaci, E. Fazio, C. Corsaro, G. Compagnini. Poster communication: *Study of magnetic nanoparticles obtained by Laser ablation of Mount Etna volcanic rocks*. **A. Brancato**, M. Condorelli, L. Catanzaro, G. Compagnini, L. D'Urso. Poster communication: *Tuning the Aggregation of Metal Nanoparticles prepared by Laser Ablation with Halide Salt solutions*. **A. Brancato**, L. Catanzaro, M. Condorelli, L. D'Urso, M. Scuderi, V. Scardaci, G. Compagnini.

- 2025 Spring Meeting of the European Materials Research Society (E-MRS), May 26-30, 2025, Strasbourg (France). Oral communication: *The Effect of Nanostructure and Wavelength on 4-NTP Dimerization*. **A. Brancato**, M. Condorelli, C. Longo, M. Barcellona, M. Fragalà, E. Fazio, G. Compagnini, L. D'Urso. Poster communication: *Mechanistic study of Silver/Platinum Nanoplates synthesis and their application as reliable SERS substrate*. **A. Brancato**, L. D'Urso, K. Al-Shamery.

- 50th Congress of the Physical Chemistry Division of the Società Chimica Italiana and 5th European Conference on Physical Chemistry (CDCF50&5thECPC), June 29 - July 03, 2025, Pisa, (Italy). Oral communication: *Laser-modified MoS2 structures for improved semiconductor SERS sensing*. **A. Brancato**, M. Condorelli, E. Fazio, C. Corsaro, G. Compagnini, L. D'Urso.

- PCAM Summer School 2025 - Materials for Nanotechnology, and 2025 Fall Meeting of the European Materials Research Society (E-MRS), September 15-18, 2025, Warsaw (Poland). Oral communication accepted: *Platinum-coated Silver Nanoplates: synthesis and application as a reliable SERS substrate*. **A. Brancato**, L. D'Urso, K. Al-Shamery. Poster communication accepted: *Silver Nanoplates transformation under solvent exchange*. **A. Brancato**, L. D'Urso, K. Al-Shamery.